



HAL
open science

Research and implementation of artificial neural networks models for high velocity oxygen fuel thermal spraying

Meimei Liu

► **To cite this version:**

Meimei Liu. Research and implementation of artificial neural networks models for high velocity oxygen fuel thermal spraying. Artificial Intelligence [cs.AI]. Université Bourgogne Franche-Comté, 2020. English. NNT : 2020UBFCA003 . tel-03092001

HAL Id: tel-03092001

<https://theses.hal.science/tel-03092001>

Submitted on 1 Jan 2021

HAL is a multi-disciplinary open access archive for the deposit and dissemination of scientific research documents, whether they are published or not. The documents may come from teaching and research institutions in France or abroad, or from public or private research centers.

L'archive ouverte pluridisciplinaire **HAL**, est destinée au dépôt et à la diffusion de documents scientifiques de niveau recherche, publiés ou non, émanant des établissements d'enseignement et de recherche français ou étrangers, des laboratoires publics ou privés.



**THESE DE DOCTORAT DE L'ETABLISSEMENT UNIVERSITE BOURGOGNE
FRANCHE-COMTE**

PREPAREE A L'UNIVERSITE DE TECHNOLOGIE DE BELFORT-MONTBELIARD (UTBM)

Ecole doctorale n°37

SPIM (Sciences Pour l'Ingénieur et Microtechniques)

Doctorat de Automatique

Par

Mme. LIU Meimei

Research and implementation of artificial neural networks models for high velocity oxygen fuel thermal spraying

Thèse présentée et soutenue à Belfort, le 31 Mars 2020

Composition du Jury :

Mr. Didier KLEIN Professeur des Universités, Université Bourgogne - Franche-Comté Président
Mme. Armelle VARDELLE Professeur des Universités, Université de Limoges Rapporteur
Mr. Abdoul-fatah KANTA Chargé de Recherche, Centre Sahélien d'Excellence en Ingénierie Rapporteur
Mr. Kondo Hloindo ADJALLAH Professeur des Universités, Université de Lorraine Examineur
Mr. Hanlin LIAO Professeur des Universités, Université Bourgogne - Franche-Comté Examineur
Mr. Sihao DENG Maître de Conférences-HDR, Université Bourgogne - Franche-Comté Directeur de thèse

Université de Technologie de Belfort-Montbéliard

**Ecole doctorale Sciences Pour l'Ingénieur et
Microtechniques**

THESE

Présentée pour obtenir le grade de

**Docteur de l'Université de Technologie de Belfort-Montbéliard en
Automatique**

**Research and implementation of artificial neural
networks models for high velocity oxygen fuel thermal
spraying**

Meimei LIU

Defended on 31st March 2020

With the jury composed of

President:

Mr. Didier KLEIN, Professeur des Universités, Université Bourgogne - Franche-Comté

Rapporteurs

Mme. Armelle VARDELLE, Professeur des Universités, Université de Limoges

Mr. Abdoul-fatah KANTA, Chargé de Recherche, Centre Sahélien d'Excellence en Ingénierie

Examiners

Mr. Kondo Hloindo ADJALLAH, Professeur des Universités, Université de Lorraine

Mr. Hanlin LIAO, Professeur des Universités, Université Bourgogne - Franche-Comté

Supervisor

Mr. Sihao DENG, Maître de Conférences-HDR, Université Bourgogne - Franche-Comté

Acknowledgements

My Ph.D. work was done in the laboratory ICB-LERMPS, UMR 6303, CNRS, Université de Bourgogne Franche-Comté (UBFC) under the support of China Scholarship Council (CSC) and the UT-INSA cooperation project (2016). The dissertation was under the guidance of Dr. Sihao DENG. The past three years have been an enjoyable research experience for me. I would like to extend my sincere thanks to all my colleagues, friends and family.

Firstly, I am extremely grateful to my supervisor, Dr. Sihao DENG, for his help, guidance, and encouragement throughout my work. His professional guidance and scientific skills made it possible to conduct this study successfully. He also helps me to shape rigorous researching attitude, which would be benefiting for my future research work.

Many appreciate go to Prof. Hanlin LIAO. His knowledge in thermal spray technology helped me a lot. He is also very generous with his help and time for discussing my work. I am very fortunate to have worked with him.

I would like to appreciate the jury members of my thesis defense session: Prof. Armelle VARDELLE, Dr. Abdoul-fatah KANTA, Prof. Didier KLEIN and Prof. Mr. Kondo Hloindo ADJALLAH, for their help and advices.

So many thanks go to the members of our ICB-LERMPS laboratory past and present: Prof. LANGLADE, Prof. COSTIL, Marie-Pierre PLANCHE, Christian ADAM, Emmanuelle ARCENS, Charles BERNAGE, Zexin YU, Franck DECROOS, Chaoyue CHEN, Yingchun XIE, Yan WANG, Chen SONG, Chunjie HUANG, Xiujuan FAN, Xingchen YAN, Xieliang XIE, Tao JIANG, Hongjian WU, Shiming XIE, Shaowu LIU, Shuohong GAO, Libin LALU KOITHARA, Farida BAADACHE, Sophie LAPRADE, Christophe VERDY, Joel CHAUVELOT and so on. I want to thank everyone for their help and assistance both in and out of the lab.

Last but not least, I want to thank especially my husband Zexin YU, for his help in my work and my life during these years. To my parents, without their encouragement, support and love, I would not have made it successfully.

Introduction

The high velocity oxygen fuel (HVOF) spray technique is performed by confining combustion gases and particles within a high-pressure chamber to produce a high-velocity jet. This technique has been extensively developed and is now widely used in all major engineering sectors. The HVOF spray process is capable of depositing a high-quality, high-performance HVOF coating that satisfies various industrial applications. In the HVOF spray process, coating properties are sensitive to the characteristics of in-flight particles, which are mainly determined by process parameters. Obtaining a comprehensive multi-physical model or analysis of the HVOF process remains challenging because of the complex chemical and thermodynamic reactions that occur during the deposition procedure. However, although industrial automation has transformed thermal spraying into a highly automated process, modern thermal spraying applications must also be intelligent. Thus, the development of a central automated system to research and analyze the correlation between operating parameters, behaviors of in-flight particles, and coating properties would yield particularly interesting results, as this could then predict coating properties that correlate with predefined parameters.

This background has driven researchers to develop a robust methodology that uses artificial neural networks (ANN) to solve issues related to HVOF-sprayed NiCr-Cr₃C₂ coatings under different operating parameters. Moreover, ANN models can be programmed and integrated into the HVOF spray control system, which subsequently creates an intelligent control system.

This dissertation is organized into six chapters, as follows:

- Chapter 1 presents a bibliographic study of thermal spray technologies, the measurement of in-flight particles' behaviors during thermal spray processes, and HVOF spray optimization methods. This chapter focuses specifically on the application of ANN models in thermal spray technologies. Additionally, a mean impact value (MIV)-based analysis is employed to quantitatively explore the relative importance of each input variable in an ANN model. This demonstrates the necessity of applying ANN models to HVOF spray processes while also highlighting the objectives and strategies of this work.
- Chapter 2 explores the details and setup of HVOF processes, including the feedstock, substrates,

characterization method of in-flight particles, coatings' characterization methods and performance evaluation methods of coatings as well as the environment to implement ANN models.

- Chapter 3 outlines the 40 sets of HVOF spray experiments and coating property tests that were conducted for analysis and to compile the data set for ANN models. The relationship between process parameters, behaviors of the in-flight particles, and coating properties were investigated from an intuitive point of view, which provided a preliminary understanding of the HVOF process and sprayed coatings. This revealed a tendency for the temperature to increase as the O₂ flow rate increases, as well as a trend for the temperature to initially increase and then decrease as the stand-off distance (SOD) increases. The increased O₂ flow rate increases the velocity of the in-flight particles. However, with the increase of SOD, the effect of the O₂ flow rate on the velocity of the in-flight particles gradually disappears. The velocity decreases progressively as SOD increases. Furthermore, both the velocity and temperature of in-flight particles have an impact on coating properties. Although the effect of process parameters on the behaviors of in-flight particles, and thus on the coating properties, can be generally summarized, it is impossible to establish direct connections between them. Thus, as a more precise prediction is necessary, the following chapters introduce machine learning methods, particularly ANN models, to address this challenge.
- Chapter 4 describes the different machine learning methods that were employed and compared to demonstrate the ANN model's superiority and necessity. Then, two ANN models were developed and implemented to predict coatings' performance (in terms of microhardness, porosity, and wear rate) and to analyze the influence of operating parameters (SOD, oxygen flow rate, and fuel flow rate), while considering intermediate variables (the temperature and velocity of in-flight particles). A set of additional experiments were also conducted to validate the reliability and accuracy of the ANN models. The chapter concludes that the implicit models that have been developed can satisfy the prediction requirements. Clarifying the interrelationships between the spraying conditions, behaviors of in-flight particles, and the final coating performances will provide better control of HVOF-sprayed coatings. The MIV-based analysis was also conducted to evaluate the factors' importance. The results indicate a number of important sequences of the

factors, including for the velocity of the in-flight particles ($SOD > O_2 \text{ flow rate} > CH_4 \text{ flow rate}$), temperature ($SOD > CH_4 \text{ flow rate} > O_2 \text{ flow rate}$), the coating's microhardness ($V > T$), and the coating's porosity and wear rate ($T > V$). These well-trained ANN models were programmed and integrated into the HVOF spray's control system, in order to create the intelligent control system that is the focus of the next chapter.

- Chapter 5 focuses on the development of the HVOF spray's control system and the integration of the packaged ANN models, which are utilized to realize an intelligent control system. First, the chapter presents a detailed introduction to the hardware and software architectures, the principle, and the programming language. This provides the foundation for developing the control system. The operation is clearly explained, ensuring the corrected operation of the system. In addition, a data-recording system was programmed, which runs in the background to monitor the spray process and observe potential fluctuations. For the integration of the ANN models, the information that is stored in the two packaged ANN models was first extracted in MATLAB. This information, together with the specific functions used, helped to encode the ANN models using MATLAB code. Finally, the ANN models were programmed and integrated into the HVOF spray's control system. With this system, the temperature and velocity of in-flight particles can be calculated by entering process parameters and subsequently obtaining specific coating properties. This integration provides a preliminary idea for the construction of an intelligent control system for the HVOF spray process, which can be applied to other thermal spray technologies.
- Chapter 6 presents this work's conclusions and perspectives.

Overall, this work not only analyzes the relationship between process parameters, behaviors of in-flight particles, and coating properties, but also provides a prediction method for the HVOF spray process and HVOF-sprayed coatings that utilizes optimized and well-trained ANN models. In addition, the work also suggests a prototype for an intelligent control system for the HVOF spray process. Therefore, further integrating an ANN model into the HVOF spray process is warranted and should be more thoroughly investigated.

Content

Acknowledgements.....	I
Introduction.....	III
Content.....	VII
List of abbreviation.....	XI
List of pictures.....	XIII
List of tables.....	XVII
Chapter 1. Backgrounds and objectives.....	1
1.1. Introduction to thermal spray technology.....	3
1.1.1. The principle of thermal spray technologies.....	3
1.1.2. Development of thermal spray technologies.....	4
1.1.3. Classification of thermal spray technologies.....	6
1.1.4. HVOF thermal spray technology.....	10
1.2. Control system and the behavior of in-flight particles.....	16
1.2.1. Diagnostic tools for measuring the behaviors of in-flight particles.....	16
1.2.2. Introduction to the Accuraspray-g3 diagnostic tools.....	19
1.3. Optimization methods for HVOF spray.....	20
1.3.1. Statistic optimization methods.....	21
1.3.2. Numerical simulation optimization methods.....	22
1.3.3. ML optimization methods.....	23
1.4. Artificial intelligence.....	27
1.4.1. History of the artificial neural network.....	28
1.4.2. Principle of the artificial neural network.....	29

1.4.3.	Feedforward neural network.....	32
1.4.4.	Procedure for designing an ANN model.....	33
1.5.	MIV analysis approach	38
1.6.	Research objectives.....	40
	Reference of chapter 1	42
Chapter 2.	Spray equipment, coating characterization, and performance test.....	51
	Introduction.....	53
2.1.	Coatings elaborating via HVOF spray	53
2.1.1.	Setup of the HVOF spray process	53
2.1.2.	Selection and treatment of powder	55
2.1.3.	Selection and treatment of substrate	56
2.2.	Characterization of in-flight particles	56
2.3.	Characterization of coatings.....	57
2.3.1.	Preparation of samples	57
2.3.2.	Observation of the morphologies of coatings.....	57
2.3.3.	Determination of the phase compositions	57
2.3.4.	Measurement of the microhardness	58
2.3.5.	Abrasive test of coatings	58
2.4.	Environment for implementing ANN models.....	59
2.5.	Conclusions.....	59
	Reference of chapter 2	60
Chapter 3.	Experimental procedure and analysis of the results.....	61
	Introduction.....	63
3.1.	Selection of HVOF process parameters and experimental procedure.....	63

3.1.1.	HVOF spray process parameters	63
3.1.2.	Experimental procedure.....	64
3.2.	Analysis of the behaviors of in-flight particles	66
3.2.1.	Temperature of the in-flight particles	67
3.2.2.	Velocity of the in-flight particles	71
3.3.	Phase composition and coating structure	73
3.3.1.	The phase composition of coatings	74
3.3.2.	The microstructure of the coatings	77
3.4.	Analysis of the coating properties.....	78
3.4.1.	The porosity of the coatings	80
3.4.2.	The microhardness of the coatings	81
3.4.3.	The wear performance of the coatings	82
3.5.	Conclusions.....	86
	Reference of chapter 3	87
Chapter 4.	Setup, training, and test of the artificial intelligence.....	89
	Introduction.....	91
4.1.	Collection and pre-processing of the dataset	92
4.2.	Comparison of different machine learning methods	93
4.3.	Implementation of ANN1 model for forecasting the behaviors of in-flight particles	97
4.3.1.	Optimization process for the ANN1 model	98
4.3.2.	Training and testing of the ANN1 model	103
4.4.	Implementation of the ANN2 model for predicting coatings' properties.....	105
4.4.1.	Optimization process for the ANN2 model	105
4.4.2.	Training and testing of the ANN2 model	108

4.5.	MIV analysis in the ANN models	111
4.6.	Conclusions	113
	Reference of chapter 4	114
Chapter 5.	The development of the HVOF control system and the integration of ANN models	117
	Introduction.....	119
5.1.	Development of the control system	119
5.1.1.	The principle of the HVOF spray control system.....	119
5.1.2.	The hardware of the HVOF spray control system	121
5.1.3.	The programming language of the HVOF spray control system.....	122
5.1.4.	The interfaces of the HVOF spray control system	125
5.1.5.	Data recording system	128
5.2.	Integration of the ANN models into the HVOF spray control system.....	129
5.2.1.	Extracting and programming with MATLAB code for ANN models	130
5.2.2.	The combination of ANN models with the HVOF control system.....	132
5.3.	Development and integration of the reversed ANN model	133
5.4.	Conclusions	135
	Reference of chapter 5	136
Chapter 6.	Conclusions and perspectives	137
6.1.	Conclusions.....	139
6.2.	Perspectives.....	141
	Abstract.....	143
	Résumé.....	145

List of abbreviation

ADALINE	Adaptive linear neuron	HVAF	High velocity air fuel
AHP	Analytic hierarchy process	HVFS	High velocity flame spraying
AI	Artificial intelligence	HVOF	High velocity oxygen fuel
ANN	Artificial neural network	I/O	Input/output
ANOVA	Analysis of variance	IEC	International Electrotechnical Commission
APS	Atmospheric plasma spraying	IL	Instruction list
CCD	Charged coupled device	LD	Ladder diagram
CDS	Continuous detonation system	LDV	Laser Doppler velocimetry
CGS	Cold gas spray	LSTM	Long short-term memory
CNNs	Convolutional neural network	MIV	Mean impact value
COF	Coefficient of friction	ML	Machine learning
CPU	Central processing unit	MLP	Multilayer perceptron
CS	Cold spray	O/F	Oxygen/Fuel
D-gun	Detonation gun	PIV	Particle image velocimetry
DBNs	Deep belief networks	PLC	Programmable Logic Controller
DC	Direct current	RBM s	Restricted Boltzmann machines
DOE	Design of experiments	RF	Radio frequency
EDS	Energy Dispersive Spectroscopy	RMSE	Root mean square error
EHC	Electrolytic hard chrome	RNN s	Recurrent neural networks
FBD	Function block diagram	SEM	Scanning electron microscope
FL	Fuzzy logic	SFC	Sequential function chart
FSM	Finite-state machine	SOD	Stand-off distance
GANs	Generative adversarial networks	ST	Structured text
GPR	Gaussian process regression	SVM	Support vector machine
GPUs	Graphics processing units	VPS	Vacuum plasma spraying
HP-HVOF	High-pressure high velocity oxygen fuel	XOR	Exclusive or
		XRD	X-ray diffraction

List of pictures

Figure 1.1 Schematic of the thermal spraying process [4].....	3
Figure 1.2 Principle for the formation of coatings by thermal spray processes [5]	4
Figure 1.3 Milestones in the development of the thermal spray industry [1]	5
Figure 1.4 Classification of thermal spray processes [15]	6
Figure 1.5 Schematic diagram of (A) wire flame and (B) powder flame processes [16]	7
Figure 1.6 Schematic presentation of an HVOF spray torch [16].....	8
Figure 1.7 Schematic diagram of DC-plasma spraying process [16].....	9
Figure 1.8 Schematic diagram of electric arc wire spray process [16]	9
Figure 1.9 Schematic of commercial high-pressure HVOF (JP5000) [18]	10
Figure 1.10 Schematic of Jet Kote II HVOF thermal spray gun and three main modeling steps [21]	11
Figure 1.11 Schematic of Top-Gun-G [22]	12
Figure 1.12 Particle temperatures and velocities obtained in different thermal spray processes, as measured for high-density materials. The arrow indicates the observed trend of recent developments (AS: powder flame spraying, FS: wire flame spraying, PS: air plasma spraying, VPS, CS: cold spray) [1, 23]	13
Figure 1.13 Schematic of the Diamond Jet 2700 [24].....	13
Figure 1.14 The principle of the Accuraspray-g3.....	20
Figure 1.15 Machine learning algorithms [67]	23
Figure 1.16 Neuron and myelinated axon, with signal flow from inputs at dendrites to outputs at axon terminals [111]	30
Figure 1.17 The structure of an elementary artificial neuron with R inputs [112].....	31
Figure 1.18 Multilayer feedforward neural network [110]	32
Figure 1.19 The pre-processing and post-processing block of the network workflow [112]	34
Figure 2.1 Interface of the HVOF spray control system.....	54
Figure 2.2 Schematic diagram of the experimental setup	55

Figure 2.3 The feedstock's morphology (a) and diameter distribution (b)	56
Figure 2.4 Installation of Accuraspray-g3 sensor.....	57
Figure 2.5 Equipment setup of ball-on-disc CSEM Tribometer (a), schematic diagram (b), and physical sample (c)	58
Figure 3.1 Some of the variables involved in the HVOF spray process	63
Figure 3.2 The experimental results of the temperature of in-flight particles for SOD from 200 to 320 mm, Q(O ₂) from 200 to 240 slpm, and Q(CH ₄) from 120 to 200 slpm.....	68
Figure 3.3 Comparison of the temperature of the in-flight particles, for different O ₂ flow rates	69
Figure 3.4 Comparison of the temperature of the in-flight particles for different CH ₄ flow rates	70
Figure 3.5 Comparison of the temperature of the in-flight particles for different SOD	71
Figure 3.6 The experimental results of velocity of the in-flight particles for SOD from 200 to 320 mm, O ₂ flow rate from 200 to 240 slpm, and CH ₄ flow rate from 120 to 200 slpm.....	72
Figure 3.7 Comparison of the velocity of the in-flight particles for different O ₂ flow rates.....	72
Figure 3.8 Comparison of the velocity of the in-flight particles for different CH ₄ flow rates.....	73
Figure 3.9 Comparison of the velocity of the in-flight particles for different SOD.....	73
Figure 3.10 XRD patterns of feedstock powders and as-sprayed coatings	76
Figure 3.11 EDS spectra analysis of the as-sprayed coatings section	77
Figure 3.12 Microstructure of the as-sprayed coatings in Set 8 (a), 35 (b), 27 (c), and 5 (d), which correspond to the spraying conditions that lead to the highest velocity, lowest velocity, highest temperature, and lowest temperature	78
Figure 3.13 The 3D (a) and 2D (b) distribution of the coating's porosity, with respect to the temperature and velocity of in-flight particles	81
Figure 3.14 Histogram of the coating's porosity	81
Figure 3.15 The 3D (a) and 2D (b) distribution of coating's microhardness, with respect to temperature and velocity of in-flight particles	82
Figure 3.16 Histogram of coating's microhardness	82
Figure 3.17 Variation of COF with sliding distance at process parameters of SOD of 200 mm (a and b), 240 mm (c and d), 280 mm (e and f), and 320 mm (g and h), as well as an O ₂ flow rate of 200 slpm (a, c, e, and g) and 240 slpm (b, d, f, and h)	84

Figure 3.18 The 3D (a) and 2D (b) distribution of coatings' wear rate with respect to the temperature and velocity of in-flight particles	85
Figure 3.19 Histogram of coating's wear rate	85
Figure 4.1 Data flow diagram of ANN models.....	91
Figure 4.2 RMSEs of some regression models for predicting the temperature and velocity of in-flight particles	94
Figure 4.3 RMSEs of some regression models for predicting the microhardness, porosity, and wear rate of coatings.....	95
Figure 4.4 The true response vs. predicted response of selected machine learning models (a–e) and ANN models (f–j) for predicting velocity (a, f), temperature (b, g), microhardness (c, h), porosity (d, i), and wear rate (e, j)	97
Figure 4.5 A typical architecture of the ANN1 model (a) and its transfer function (b)	98
Figure 4.6 Comparing the performance of the ANN1 model with different combinations of transfer functions	99
Figure 4.7 Comparing the performance of the ANN1 model with different training functions	100
Figure 4.8 Comparing the performance of the ANN1 model with different performance functions	101
Figure 4.9 Comparing the performance of the ANN1 model with different structures.....	102
Figure 4.10 Relative error of velocity (a) and temperature (b) between experimental and predicted results, with respect to the experimental results	104
Figure 4.11 Comparison of the experimental and predicted values of velocity (a) and temperature (b), for the test set in the ANN1 model	104
Figure 4.12 A typical architecture of the ANN2 model	105
Figure 4.13 Comparing the performance of the ANN2 model with different combinations of transfer functions	106
Figure 4.14 Comparing the performance of the ANN2 model with different training functions	106
Figure 4.15 Comparing the performance of the ANN2 model with different performance functions.....	107
Figure 4.16 Comparing the performance of the ANN2 model with different structure	108
Figure 4.17 Relative error of microhardness (a, d), porosity (b, e), and wear rate (c, f), between	

the experimental and predicted results, with respect to the experimental results	110
Figure 4.18 Comparison of the experimental and predicted values of microhardness (a), porosity (b), and wear rate (c), for the test set in the ANN2 model	111
Figure 4.19 The contribution rate of input variables on the velocity (a) and temperature (b) of in-flight particles, as well as coating microhardness (c), porosity (d), and wear rate (e)	112
Figure 5.1 System architecture diagram of the HVOF spray control system	120
Figure 5.2 Workflow of the HVOF spray control system	121
Figure 5.3 Hardware of the HVOF spray control system.....	122
Figure 5.4 A simplified example of code for the control system.....	124
Figure 5.5 Operation panel of the HVOF spray control system	125
Figure 5.6 Interface of the CDS system.....	126
Figure 5.7 Interface of the Diamond-Jet system	126
Figure 5.8 Interface of the maintenance system.....	127
Figure 5.9 Interface of the configuration system.....	128
Figure 5.10 Data recording files for the CDS and Diamond-Jet systems.....	129
Figure 5.11 The workflow of integrating the ANN model	130
Figure 5.12 Neural network constant of the ANN1 model.....	131
Figure 5.13 Code for constructing the ANN1 model in MATLAB.....	132
Figure 5.14 Interface of the ANN models in an HVOF control system	133
Figure 5.15 Integration of the ANN3 model into the HVOF control system.....	134

List of tables

Table 1.1 The differences between the three generations of HVOF systems [19].....	13
Table 1.2 Part of the HVOF-sprayed coatings, as well as their applications and relevant properties.....	15
Table 1.3 Some of the main parameters of commercial diagnostic tools.....	18
Table 1.4 Examples of ANN models used in APS	25
Table 1.5 Three different types of transfer function: step, sigmoid, and linear, in unipolar and bipolar formats [110]	31
Table 1.6 The most common pre-processing and post-processing functions and their algorithms in MATLAB [112].....	35
Table 1.7 Four functions for dividing data, which are provided in MATLAB [112].....	35
Table 1.8 Part of the training function in MATLAB [112, 116]	36
Table 1.9 Part of the network performance function in MATLAB [112].....	37
Table 2.1 Chemical composition of the feedstock powder	55
Table 3.1 HVOF spray process parameters	65
Table 3.2 Experimental design of the HVOF spray process	65
Table 3.3 The temperature and velocity of in-flight particles	67
Table 3.4 The porosity, microhardness, and wear rate of coatings.....	79
Table 4.1 Physical limits of the input and output variables	93
Table 4.2 Default setting for functions and parameters for the ANN models.....	99
Table 4.3 Optimized functions and parameters for the ANN1 model	102
Table 4.4. Optimized functions and parameters for the ANN2 model	108
Table 4.5 MIV values for input variables.....	112

Chapter 1. Backgrounds and objectives

1.1. Introduction to thermal spray technology

1.1.1. The principle of thermal spray technologies

Thermal spraying processes are a group of coating technologies, through which a stream of finely divided metallic and nonmetallic particles are deposited, in a molten or semi-molten condition, onto a prepared substrate to form a coating [1].

The core device of the thermal spraying process is the thermal spray torch, which is used to heat the feedstock to a molten or semi-molten state and to accelerate it towards the substrates. This ultimately forms featured morphologies known as “splats” or “lamellar structures” [1-3]. The heat source can be a combustion flame, a plasma jet, or an arc struck between two consumable wires. The general schematic of the thermal spraying process is shown in [Figure 1.1](#). The final coatings can be built-up by depositing the feedstock across a certain number of passes. The heated and accelerated droplets or particles are then able to perform three actions: they can plastically deform or rapidly cool into thin lamellae on impact, they can adhere to the surface, and they can overlap and interlock into a consolidated coating during the rapid solidification process [2]. A more detailed outline of the interaction between particles and substrates is presented in [Figure 1.2](#). In order to improve mechanical bonding between splats and substrates, the substrates are normally pre-treated by sandblasting, as this increases their surface roughness. The substrate can be kept at a relatively low temperature, using specific cooling devices. The number of deposition passes depends on the required coating thickness.

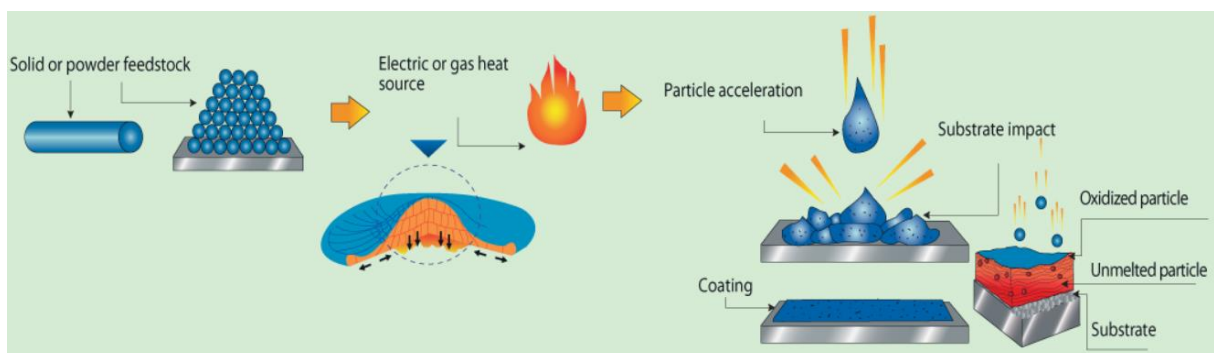


Figure 1.1 Schematic of the thermal spraying process [4]

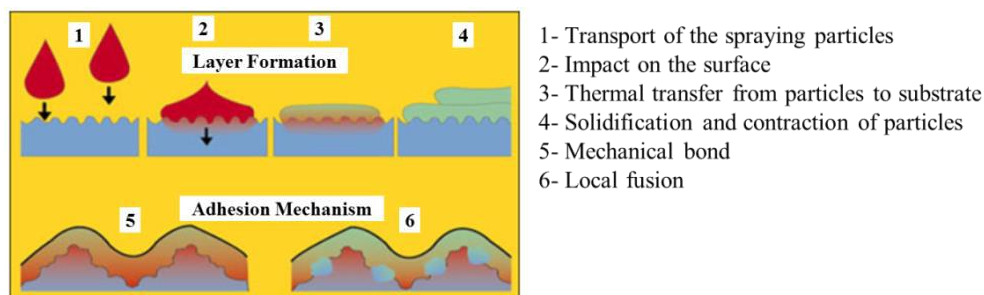


Figure 1.2 Principle for the formation of coatings by thermal spray processes [5]

1.1.2. Development of thermal spray technologies

The Swiss inventor Max Ulrich Schoop is believed to be the “father” of thermal spraying technology, when he established thermal spraying in early 1900s [6]. During his early experiments, low melting point metals were atomized by pouring a stream of molten metal into a jet of high-pressure gas [7]. In its infancy, thermal spraying technology was limited to low melting point materials, such as lead, tin, and zinc, but this subsequently extended to steels. Wire flame spraying was developed to avoid un-melted particles in the spray jet, as the wire feedstock was drawn by drive rolls into the rear of the gun. The melting temperature for materials was initially limited to 1,500–1,600 °C [8]. Until the 1950s, thermal spray technology essentially consisted of flame spraying. Wire and powder flame sprays were the principle thermal sprays in the process, between the 1910s and 1950s. Materials’ reclamation was the key driver in these early years, particularly that of large industrial machinery and the cathode corrosion protection of very large steel structures.

In the mid-1950s, the first plasma spray torch was developed by the Thermal Dynamics Corporation (Lebanon, NH), which was followed by developments by Metco and Plasmadyne [1]. These torches form the basis of many of the torches that remain in use today. Thereafter, plasma spraying became an attractive option for the aeronautics industry and later for the aircraft industry. The thermal plasma heat source (the direct current [DC] arc or the radio frequency [RF] discharge), which have temperatures of over 8,000 K at atmospheric pressure, dramatically extended the technology’s possibilities to include any material that could melt (i.e., the difference between a material’s melting and decomposition or evaporation temperatures was preferably greater than 300 K) [9]. Roughly a decade later, soft vacuum plasma spraying was introduced in to the industry, which made it possible to suppress some important drawbacks of atmospheric plasma spraying (APS) [10].

The emergence of these developments led to the thermal spray becoming a process of choice in the 1970s and 1980s, particularly for component protection and performance enhancement in the aero-engine industry.

In the early 1980s the high velocity oxy-fuel flame (HVOF) (Jet Kote, Doloro-Stellite, Goshen, IN) was introduced by Browning and Witfield [8, 11], who used rocket engine technologies to develop a new way of spraying metal powders. Different kinds of HVOF torches then became available, whose combustion pressure increased from 0.4 to 1.35 MPa. Furthermore, values of up to 4 MPa are expected [12]. High velocity air fuel (HVOF) torches were also designed, through which pressures of 0.8 MPa were achieved, with high-inlet air pressure (1 MPa) providing most of the burner cooling (i.e., only 10% of the energy was lost in the cooling system) [13]. The HVOF process can increase chamber pressure, theoretically achieve higher particle velocity, and therefore obtain desired coatings, particularly metallic and cermet coatings. These coatings have long been the goal of all other coating processes, as they are higher density, have improved corrosion barrier, higher hardness, better wear resistance, higher bonding and cohesive strength, almost no oxidation, thicker coatings, and smoother as-sprayed surfaces [8].

Figure 1.3 illustrates the history of the thermal spray and improvements in its performance through new developments. Additionally, after decades of development, thermal spray technologies have developed in various categories.

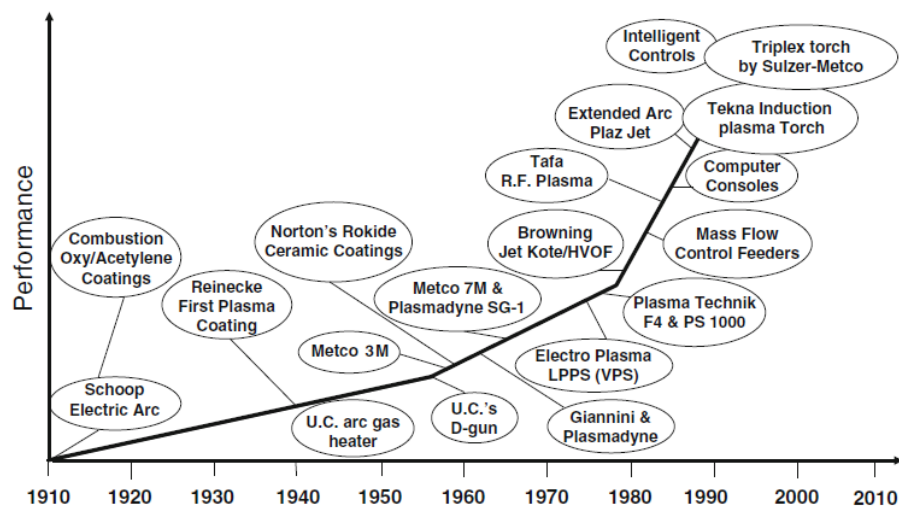


Figure 1.3 Milestones in the development of the thermal spray industry [1]

1.1.3. Classification of thermal spray technologies

Thermal spray coatings can be formed in two ways: through the deposition of molten or semi-molten particles that have passed through heat sources, such as in a flame spray, plasma spray, HVOF, HVAF, or wire arc spray; and through the deposition of ductile metallic or plastic particles in a solid state (cold gas spray [CGS] gun), or metallic or ceramic particles in a plastic state (detonation gun [D-gun]) [14]. Thermal spraying processes can be classified as either combustion, electric arc, or kinetic, according to the source of energy, as shown in Figure 1.4 [2, 15]. For the kinetic thermal spray (also known as a “cold spray”), coatings are formed through the plastic deformation of ductile metallic or alloyed powders, which is different from combustion spraying or electrical-discharge plasma spraying [1]. The following section will concentrate on the combustion spray and electrical-discharge thermal spray routes.

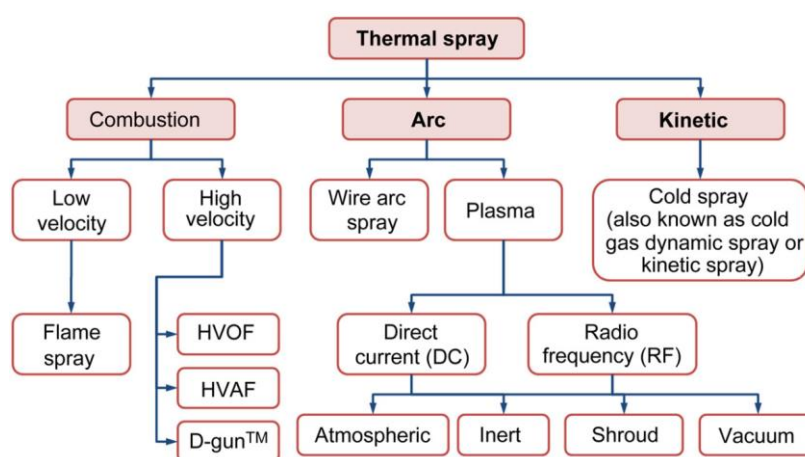


Figure 1.4 Classification of thermal spray processes [15]

Combustion spraying

Conventional flame spraying is the oldest thermal spraying technology, which is characterized by low cost, high deposition rates and efficiencies, and relative ease of both operation and cost of equipment maintenance [16]. It is conducted at atmospheric pressure through the combustion of oxyacetylene mixtures to achieve a temperature of up to approximately 3,000 K. Flame temperatures and characteristics depend on the oxygen-to-fuel gas ratio and pressure. The corresponding flame velocities are below 100 m/s, and a wide variety of feedstock (such as metals and polymers) can be deposited in rods, wires, or powder to form the coatings [1, 16]. The flame spraying process, using wires and powders as feedstock, is illustrated in Figure 1.5 [16].

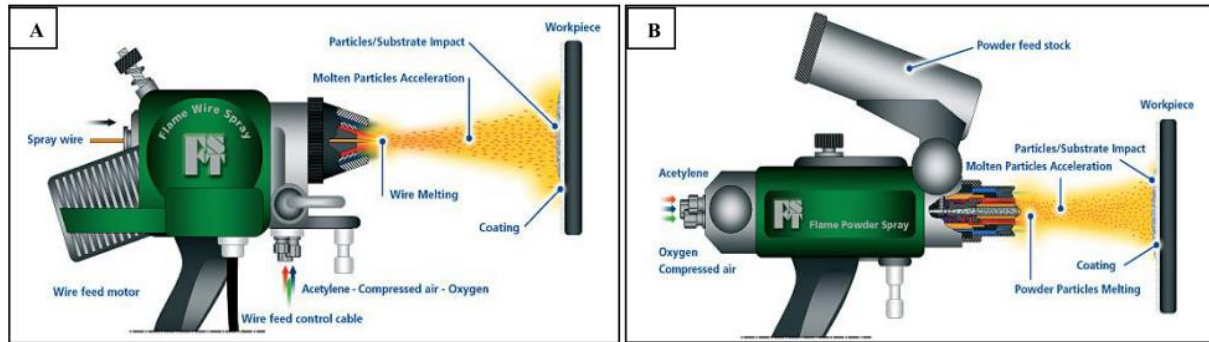


Figure 1.5 Schematic diagram of (A) wire flame and (B) powder flame processes [16]

High velocity flame spraying (HVFS) involves several different combustion flame spray processes, during which a gaseous or liquid fuel is combusted in the combustion chamber of the spray gun, with oxygen or air as the oxidizer. This involves techniques such as HVOF spraying, high-pressure high velocity oxygen fuel (HP-HVOF) spraying, HVOF spraying, high velocity impact-fusion spraying, and other novel techniques (e.g., the warm spraying process) [17]. All these techniques are similar, but they differ from each other in terms of gun design, type of fuel (gas or liquid), type of oxidizer (oxygen or air), particle temperature and velocities, and in other less important characteristics. Both HVOF and HVOF spraying processes employ combustion energy from gas or liquid fuel to heat the injected powders, in which a Laval-type nozzle is used to achieve high gas velocity. The usage of air instead of oxygen means that HVOF generates a lower gas temperature and higher gas velocities, compared to HVOF [1, 16]. In addition, the D-gun can be considered an intermittent HVOF process, with the difference that the explosion of fuel and oxygen creates a detonation-pressure wave, instead of the continuous steady state characteristic of the HVOF process [15]. All of the HVOF, HVOF, and D-gun routes focus on the high speed of particles and a stronger impact on the substrate, in order to form reasonably dense coatings. Figure 1.6 schematically presents an HVOF spray gun [16], which consists of a fuel gas/oxygen mixer, a combustion chamber, and an expansion nozzle. In modern HVOF guns, the expansion nozzle is usually a converging/diverging de-Laval type nozzle. Such nozzles lead to high gas velocities, which in turn accelerate the powder particles to very high velocities in the order of 600–800 m/s [17].

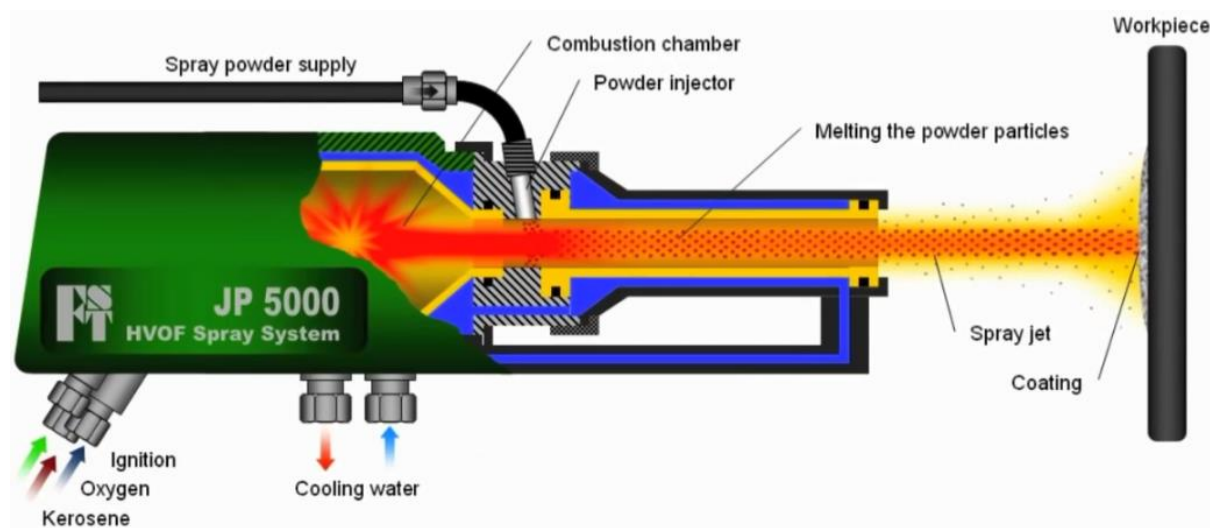


Figure 1.6 Schematic presentation of an HVOF spray torch [16]

Electrical-discharge thermal spray

The electrical-discharge thermal spray process also employs electrical energy to heat the feedstock, either in the form of an arc or plasma, as illustrated in Figure 1.4. Based on the different plasma types, the plasma spray involves both DC and RF inductively coupled plasma.

In DC-plasma spraying, an electric arc generates plasma within a plasma torch. The torch is mainly comprised of a tungsten cathode and a cylindrical copper anode as the nozzle, which are cooled by water during deposition. The plasma gas is injected at the base of the cathode, heated by the arc, and exits the nozzle in the form of a high-temperature, high-velocity jet. The normal working gases for DC-plasma spray are Ar–H₂, Ar–He–H₂, and N₂–H₂ mixtures, which result in a core temperature as high as 15,000 K inside the plasma plume at the nozzle exit [1]. Figure 1.7 is a schematic diagram of the DC-plasma spraying route. When the deposition procedure is operated under atmospheric pressure, the process is commonly called APS. When under soft vacuum conditions, this is commonly referred to as vacuum plasma spraying (VPS), which is able to efficiently avoid the formation of secondary phases in the coatings. Since the vacuum system is expensive, the gas shroud system has been also introduced in to the APS process, where an inter gas from a shroud system restricts the amount of entrained air and oxygen [15]. Generally, APS is used for depositing ceramic-based coatings, due to the high temperature of the plasma plume, and the feedstock are normally in powder-form and in tens of micrometers. More recently, solution or suspension precursors have also been used to deposit finely structured films.

Another type of plasma source, which is generated through the electromagnetic coupling of energy into the discharge cavity, is RF inductively coupled plasma [1]. Similar to the DC-plasma spray process, the deposition atmosphere can be adjusted according to the requirements of the coatings. Compared to DC-plasma spraying, the greatest advantage of RF inductively coupled plasma is that it is adept at melting larger particles in materials of low thermal conductivity [1].

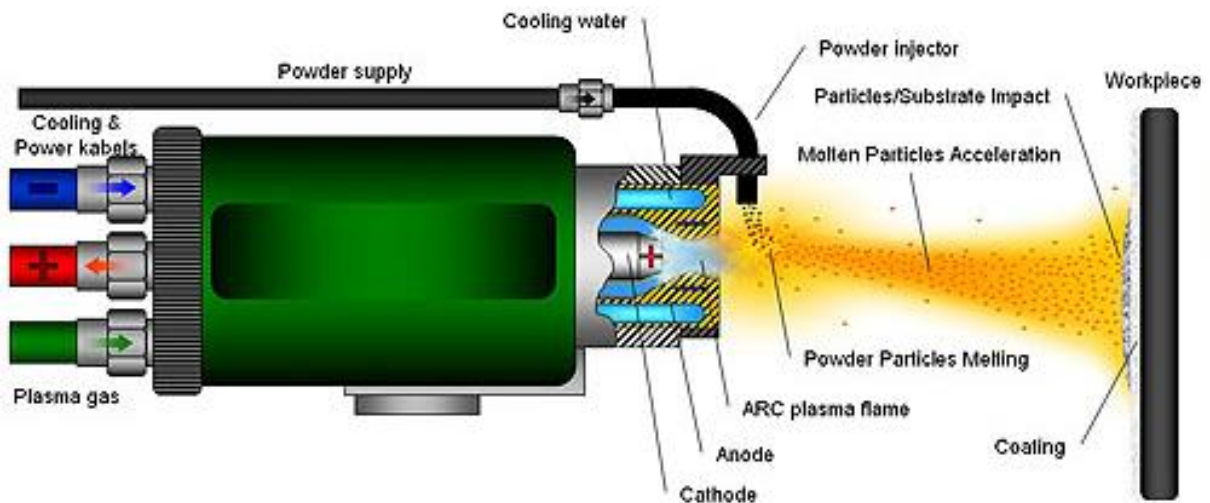


Figure 1.7 Schematic diagram of DC-plasma spraying process [16]

The wire arc spray process is also known as the twin-wire arc process, since the arc is struck between two continuously advancing wires, one of which is the cathode and the other the anode. Feedstock in wire form is continuously fed into the arc zone for melting and the subsequent droplets are further atomized and accelerated by the carrier gas. Arc spraying is used to apply only electrically conductive materials, including different metals, metal alloys, and metal-metal oxide or metal-carbide mixtures (cord wires). This type of process is extensively employed for the protection of steel bridges [1, 16]. Figure 1.8 schematically presents an electric arc two-wire spray gun.

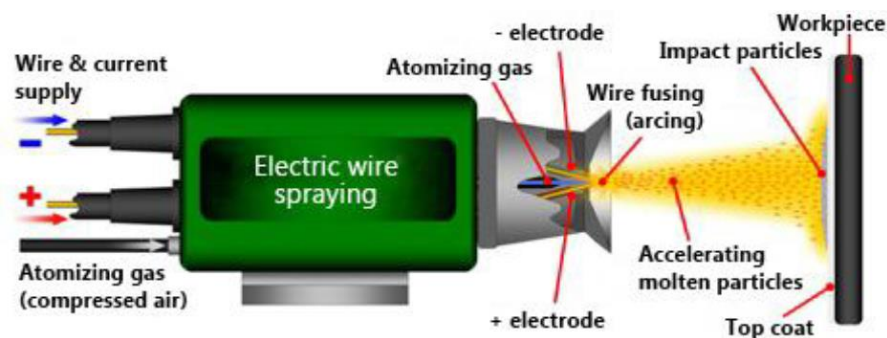


Figure 1.8 Schematic diagram of electric arc wire spray process [16]

1.1.4. HVOF thermal spray technology

Introduction to the HVOF spray process

Since first being introduced in the early 1980s, the HVOF spray technique has been extensively developed, compared to other thermal spray technologies, and it is now widely applied throughout all major engineering industry sectors. Indeed, different kinds of HVOF spray systems with different gun designs and capacities have been examined. Yet these are all based on the same fundamental principles. The HVOF spray process works by confining combustion gases and particles in a high-pressure chamber, in order to produce a high-velocity jet. As shown in Figure 1.9, oxygen and fuel gas or liquid, such as hydrogen, kerosene, propane, propylene, natural gas, ethylene, acetylene, or alcohol, are introduced into the combustion chamber and ignited. The combustion of the gases produces a high temperature and high pressure in the chamber, which causes the supersonic flow of the gases through the nozzle. After the powder particles are fed into the combustion chamber, they melt or partially melt there and during their flight through the nozzle. The feedstock powder can be fed into the system axially or radially, entrained into the high-velocity jet, and accelerated through the barrel to deposit onto a substrate [15].

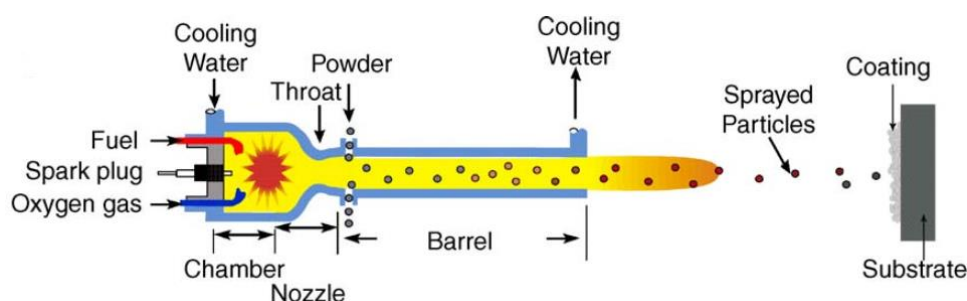


Figure 1.9 Schematic of commercial high-pressure HVOF (JP5000) [18]

Although this process benefits from a reasonable process temperature, the particle velocity on impact is very high. In the HVOF spray process, the flame temperature varies in the range of 2,700–3,500 K, depending on the fuel, the fuel gas/oxygen ratio, and the gas pressure. Particles melt completely or only partially, depending on the flame temperature, particle dwell time, material melting point, and thermal conductivity [19]. As this uses a supersonic jet, which differentiates it from the conventional flame spray, the speed of particle impact on the substrate is much higher, resulting in improved coating characteristics. The mechanism differs from flame spraying because of an

expansion of the jet at the exit of the gun [16]. Different kinds of HVOF spray systems with different gun designs and capacities will be introduced in subsequent sections.

Introduction to the HVOF spray system

Various HVOF spray systems have been developed with different gun designs and capacities, all of which satisfy different industries requirements. Full HVOF spray systems consist of different units [20], including: gas supplies (fuel gas/liquid fuel, oxygen); air supply (compressed air); gas hoses; gas regulators for oxygen, fuel, and air (if used); rotameters or mass flow controllers for gas flow controls; flashback arrestors at the gun and regulators; HVOF spray torch composed of a torch body, gas mixer, combustion chamber, de-Laval nozzle, and gun cooling; powder feeding system; and a spray gun manipulator/robot (unless manually operated).

These systems can be roughly divided into the first, second, and third generation. Jet Kote is the typical representative in first-generation guns [21], in which oxygen and gas are combusted in the combustion chamber (located in the vertical handle) and high-temperature gas (roughly $2,800^{\circ}\text{C}$) reaches the barrel through a ring of annular holes at a certain angle. The powder is fed into the center of the bore of the barrel axially, where the hot gas heats the powder and accelerates it out of the barrel. Both the combustion chamber and the barrel are water-cooled, as displayed in Figure 1.10. First-generation HVOF systems typically feature a relatively large combustion chamber and a straight nozzle. With this design maximum of 1 Mach (where gas velocity is related to the sonic speed), velocities can be produced. The temperature of the powder particles can be above $2,000^{\circ}\text{C}$.

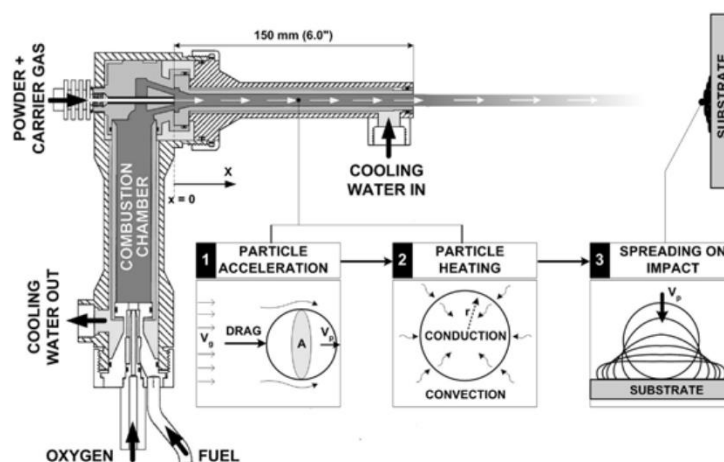


Figure 1.10 Schematic of Jet Kote II HVOF thermal spray gun and three main modeling steps [21]

In both first- and second-generation guns, the pressurized burning of gaseous fuel with oxygen is used to produce an exhaust jet that travels at a speed of around 2,000 m/s. The main fundamental difference between the first and second generation is the design of the nozzle. Second-generation guns, such as the Diamond Jet Standard, the Top Gun (Figure 1.11), and the continuous detonation system (CDS), are characterized by a de-Laval nozzle. The de-Laval nozzle enables over 1 Mach velocities at the diverging part of the nozzle. Under standard spray conditions, the systems are operated at a power level of about 100 kW and are capable of spraying about 2–3 kg/h of WC-Co powders [19].

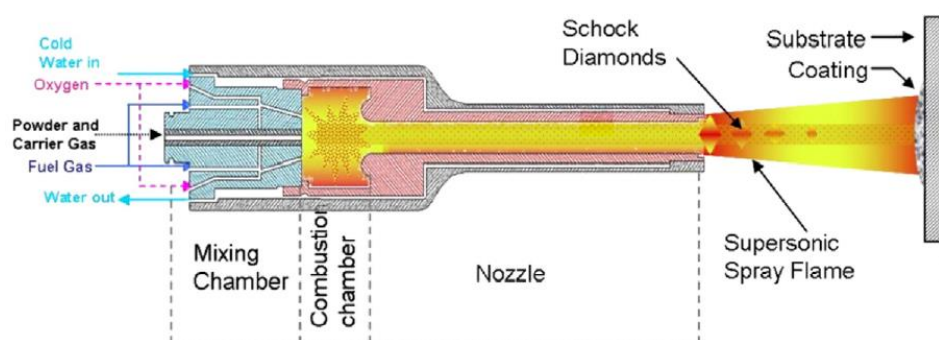


Figure 1.11 Schematic of Top-Gun-G [22]

The development of HVOF systems has aimed to reduce the temperature of particles and increase their velocity, which is shown in Figure 1.12 [1, 23]. Higher particle velocities were obtained using converging-diverging de-Laval type nozzle designs and higher gas pressures. Third-generation systems are used for power levels that range from 100–300 kW and for higher chamber pressures that range from 8 bars up to as much as 25 bars. This is because they are capable of spray rates of up to roughly 10 kg/h [19]. With these features, third-generation systems, such as the DJ2700 (Figure 1.13), DJ2800, and JP5000, accelerate spray particles to velocities of about 650 m/s.

Table 1.1 summarizes the key differences between generations [19]. HVOF process development has seen a trend towards higher gas pressures, faster particle velocities, and lower particle temperatures. This has a clear influence over the coating microstructure, where the amount of oxidation in the lamella boundary is decreased and the flattening rate is increased, and the coating density is subsequently improved from generation to generation [19]. A further reduction in particle temperatures, below the melting temperatures of metals, requires a substantial increase in velocity, which can only be realized by optimizing the expansion ratio in the diverging nozzle section and by

using higher chamber pressures through the injection of noncombustible gases [1].

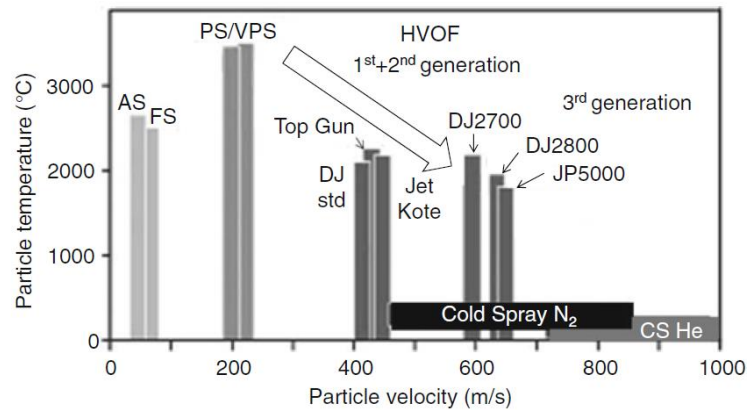


Figure 1.12 Particle temperatures and velocities obtained in different thermal spray processes, as measured for high-density materials. The arrow indicates the observed trend of recent developments (AS: powder flame spraying, FS: wire flame spraying, PS: air plasma spraying, VPS, CS: cold spray) [1, 23]

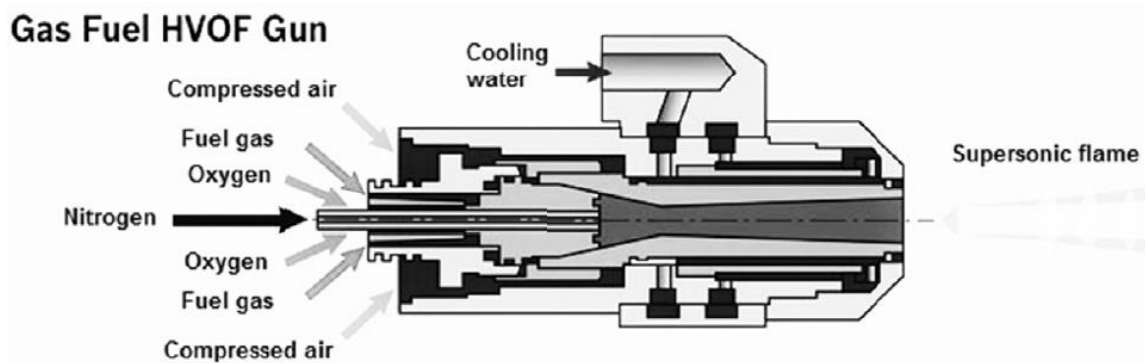


Figure 1.13 Schematic of the Diamond Jet 2700 [24]

Table 1.1 The differences between the three generations of HVOF systems [19]

	Nozzle type	Power level (kW)*	Chamber pressure (bar)	Kg/h (WC-Co)
1st generation	straight	80	3 to 5	2 to 6
2nd generation	De laval	80 to 120	5 to 10	2 to 10
3rd generation	De laval	100 to 300	8 to 12 (up to 25)	10 to 12

*Total Heat Output

After years of evolution, HVOF spray processes are more capable of depositing HVOF coatings with high qualities and desired performances, which satisfies various industrial applications.

Performance of HVOF-sprayed coatings

HVOF-sprayed coatings, such as WC-Co-based, NiCr-based, and Fe-based coatings, have been widely utilized to improve the surface quality and performance of metal parts for varied industrial applications, due to their excellent chemical and mechanical performance, which include high oxidation resistance, corrosion resistance, and wear resistance. With its high flexibility and cost effectiveness, the HVOF spray process is regarded as one of the most efficient techniques for depositing high-performance coatings. The main features of the HVOF process are its ability to produce dense coatings with low amounts of degradation, the oxidation of metallic materials, and phase transformations. As such, this is widely used to produce cermet and metal coatings, in order to improve the properties of substrates. Moreover, it has also been demonstrated that the HVOF process is able to deposit dense ceramic coatings. [Table 1.2](#) lists part of the HVOF-sprayed coatings, along with their applications and relevant properties. Currently, HVOF-sprayed WC- and Cr_3C_2 -based coatings are extensively considered to be an alternative to electrolytic hard chrome (EHC) coatings, as they have a reduced environmental impact and lower overall costs than those associated with the EHC process. In addition, HVOF-sprayed coatings exhibit higher corrosion resistance, higher powder deposition efficiency, lower density, and lower post-processing costs, compared to EHC coatings [25]. Different kinds of HVOF-sprayed coatings can be employed for various applications that have anti-wear, anti-erosion, anti-corrosion, or anti-oxidation requirements, either at room temperature or a high temperature. The HVOF spray process can also be used to deposit hydroxyapatite (HA) coatings, which satisfies biomedical applications [26, 27].

The NiCr- Cr_3C_2 powder has been selected as the feedstock for HVOF spray in this work because this is a typical feedstock for the HVOF spray. The coatings' porosity, microhardness, and wear behaviors have been subsequently evaluated and studied. Furthermore, as previously discussed in [Section 1.1.4.1](#), the behaviors exerted by in-flight particles greatly impact the coating's performances, which makes it beneficial to monitor and control the behaviors of in-flight particles, in order to better control the coatings' properties.

Table 1.2 Part of the HVOF-sprayed coatings, as well as their applications and relevant properties

Material	Properties	Applications	Reference
WC/Co(Cr)	Wear resistance, erosion wear resistance, high temperature wear resistance, cavitation erosion resistance, slurry erosion and corrosion resistance, etc.	Airplane landing gear, turbine blades, diesel engines, machining cutters, mining tools, wear machine parts, fluid medium (such as pumps, valves and turbines), and carrier rollers, etc.	[28-31]
Cr ₃ C ₂ /NiCr	Wear resistance, erosion–corrosion resistance, high temperature oxidation resistance, hot corrosion resistance, nonslip behavior, Impact wear resistance, etc.	worm gears, tiller blades, hydraulic cylinders, flight decks, finned walls in fossil fuel power plants, etc.	[32-36]
WC/Ni(Cr ₃ C ₂)	Wear resistance, high temperature wear resistance, high temperature oxidation resistance, hot corrosion resistance, etc.	gears for automotive and aerospace, power plant boilers, etc.	[35, 37, 38]
NiCrBSi	Wear resistance, corrosion resistance, hot corrosion resistance, etc.	Rollers for printing machines, boiler tubes, worm gears for extrusion (rare), etc.	[39, 40]
CoMoCrSi	Wear resistance, high temperature wear resistance, corrosion and oxidation resistance, etc.	Hardfacing of notches in jet engine turbine blades, tip shroud of turbine blade, etc.	[41-43]
Fe-based	Wear resistance, cavitation erosion resistance, corrosion resistance, etc.	pumps, valves, turbines, ship propellers, pipes, etc.	[44-46]

1.2. Control system and the behavior of in-flight particles

Thermal spray technologies aim to produce coatings with the suitable properties and required performance for specific applications. In order to achieve this objective, a deeper understanding of the spray process as a whole is necessary. The starting material, spray process, and particle-substrate interactions all affect the formation of coatings with different microstructures, which subsequently affect the coating properties and, ultimately, the coating's performance [19]. During the spray process, the characteristics of the in-flight particles are determined by thermal and kinetic exchanges between the thermal jet and the particles. The diagnosis will therefore be mainly based on the measurement of temperatures and the speeds of in-flight particles.

1.2.1. Diagnostic tools for measuring the behaviors of in-flight particles

The properties of coatings strongly depend on the molten state and velocity of the particles upon impact. As previously discussed in Section 1.1.4.2, the development of HVOF systems has aimed to reduce the temperature of particles and to increase their velocity. Modern HVOF spray guns usually use a converging/diverging de-Laval-type nozzle, which leads to high gas velocities and, in turn, the acceleration of the powder particles to very high velocities, in the order of 600–800 m/s [17]. For the temperature of in-flight particles, the flame temperature varies in the range of 2,700–3500 K, depending on the fuel, the fuel gas/oxygen ratio, and the gas pressure. This leads to a temperature of in-flight particles as high as 2,000°C [1, 19, 23].

Two types of methods can be used to measure this speed: the probe method and the optical method. The first method, which includes a Pitot tube, is limited by the problems of holding these probes in a high-temperature environment and problems related to the introduction of disturbing elements in the flow, all of which make these techniques inappropriate for the HVOF spray process. Several measurement systems have been developed for the second optical method, which are based on different physical principles, such as laser Doppler velocimetry (LDV) and particle image velocimetry (PIV) [47].

Temperature diagnoses can be conducted by means of either expansion thermometers, or electric thermometers, or optical pyrometers. The diagnoses of the temperature of hot in-flight particles are

performed by optical pyrometer devices. The optical pyrometer is a method of measuring temperature based on the relationship between the temperature of an object and the optical radiation (infrared or visible) emitted by the object. Optical, photoelectric, or thermal sensors are used, as the optical pyrometer has the advantage of allowing the determination of a temperature without contact with the object. It is therefore an appropriate method for situations in which the experimental conditions do not allow the use of conventional thermometric sensors [48].

In order to better control the thermal spraying process and evaluate the on-line state of the key physical process variables, different sensing devices have been developed during the last decade. They are based on measuring techniques and monitor these characteristics. These devices have been designed to resist the harsh environment that exists in spray booths, and to return reliable information over time [8]. Currently, products are available that are based on the use of the charged coupled device (CCD) camera and based on the pyrometer:

- 1) The DPV 2000 (Tecnar) is a robust, easy-to-use optical sensor that allows detection of the velocity of the in-flight particles by a time-of-flight technique, their temperature by a fast (100 ns) two-color pyrometer, and their diameter (starting from the thermal emission of the particles). An optical-fiber linear array, located in the same sensor head, is used to monitor the hot jet particles and to characterize the trajectories of the sprayed particles. The use of a CCD camera also enables the DPV to detect the position of particles [8, 48].
- 2) The Accuraspray (Tecnar) can continuously record average particle velocity and average particle temperature, as well as the position, width, maximum luminosity, and overall intensity of the spray plume. It is equipped with three sensor heads: “L” for a relatively low-temperature process (e.g., HVOF), “H” for high temperatures (e.g., plasma, combustion, and electric arc wire), and “Ti” for high-temperature processes that spray materials containing titanium oxide. The newest product (Accuraspray 4.0) can even be used to detect suspension spraying (plasma and HVOF) [49].
- 3) The SprayWatch (Oseir) can measure everything except particle size [50]. Their newest product (SprayWatch 4S) uses a novel, patented pyrometric filter design for repeatable temperature and particle measurement without frequent re-calibrations. Optics are adjusted

on the camera, which facilitates the diagnostics of a wide variety of processes, with the same system matching the measurement area to the plume width for best results [50].

- 4) The In-Flight Particle Pyrometer has a sensor head that forms a measurement volume of 5 mm in diameter and approximately 50 mm long. This allows two-color pyrometry to determine the mean temperature of particles that cross the measurement volume [8, 51]. This has been used on NiAl in-flight particles in a plasma jet [52] and on alumina droplets resulting from an arc spray [53].
- 5) The Spray Deposit Control enables the calculation of velocity from the traces left by in-flight particles, using a CCD camera. It also enables measurement of the temperature of the coating and substrate during spraying, using a pyrometer. This system provides distribution of the heat flux that is associated with hot in-flight particles, and can deduce the thermal and quenching stresses (preheating, cooling, and during projection) [48, 54].
- 6) STRATONICS can measure the temperature of p in-flight articles, using a CCD camera and a two-color pyrometer.

Table 1.3 lists some of the main parameters of commercial diagnostic tools that detect the characterization of in-flight particles. Selection of different diagnostic tools requires comprehensive consideration of their abilities and cost. This study has selected the Accuraspray-g3 to detect the characteristic of in-flight particles during the HVOF spray process, due to its cost and existing equipment available in the study’s laboratory. More details about this decision are given in the next section.

Table 1.3 Some of the main parameters of commercial diagnostic tools

Parameters	DPV Evolution	Accuraspray 4.0	SprayWatch 4s	STRATONICS
Temperature (°C)	1000 to 4000	>1000	1000 to 4000	1200 to 2700
Precision (%)	2.5	3	-	1
Velocity (m/s)	5 to 1200	5 to 1200	1 to 2000	10 to 900
Precision (%)	0.5	2	-	-

Particle Size(μ m)	10 to 300	-	-	-
Precision (%)	5 to 7	-	-	-
Plume intensity	✓	✓	✓	-
Plume position	✓	✓	✓	-

1.2.2. Introduction to the Accuraspray-g3 diagnostic tools

The Accuraspray-g3 has been selected to detect the characteristics of in-flight particles during the HVOF spray process that is conducted in this study. [Figure 1.14](#) displays the principle of the Accuraspray-g3.

The Accuraspray-g3's dual fiber optical device (1) "sees" the flow of particles at two different points along the spray stream (2). The signal from the detector (3) is delayed in time because it comes from the same particles that are detected by the detector (4), a few millimeters apart. Cross-correlation yields a very precise measurement of the time delay (5), from which the velocity can be calculated, since the gap between the measuring points is known and constant.

The signals (7, 8) are filtered at two different wavelengths, allowing the mean particle temperature to be measured using the twin wavelength pyrometer principle. This assumes that the emissivity of the particles is the same for the two wavelengths. A value of the cross-correlation between 0 and 1 verifies the validity of the temperature measurement. A correlation threshold is typically set at 0.6, which ensures that both detectors (3, 4) see the same population of particles, and therefore that the twin wavelength pyrometer is working properly.

The spray plume's properties (i.e., width, position, and maximum luminosity) are measured from the digitized live video plume image that is recorded by the CCD camera (6). The spray plume's optical intensity is measured at each point at a given stand-off along the "sampling line," which obtains an intensity profile with a maximum value that is close to center plume. Integrating the total area under that curve results in a value, called intensity, which is proportional to the total optical energy that is radiated by the spray plume at that specific stand-off distance. Units are normalized intensity values that correspond to 100% of light intensity, which is just sufficient to nearly saturate

the CCD camera, when it is set to its minimum sensitivity (shutter speed 1/10,000s). Each CCD camera is calibrated in such a way that it returns the same intensity value when it is aimed at the exact light source.

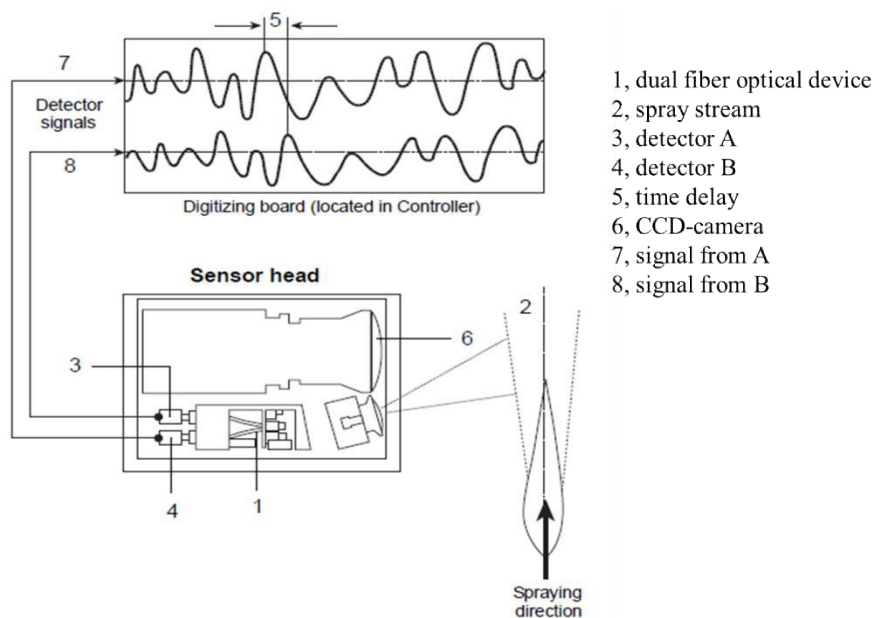


Figure 1.14 The principle of the Accuraspray-g3

1.3. Optimization methods for HVOF spray

HVOF spray is a very complex process, as a large variety of variables affect the deposit formation and, hence, the coating properties. These variables include the process parameters of the spray system (e.g., the flow rates of oxygen, fuel, and air, and the feed rate of powders), robot operating parameters (e.g., stand-off distance, spraying angle, and scanning step), feedstock powders properties (e.g., particle size and particle size distribution), and hardware characteristics (e.g., nozzle geometry). In the HVOF spray process, the powder particles experience very high speed and fast heating (up to its melting point or above). This high temperature and rapid reaction process may cause complex chemical and thermodynamic reactions, such as evaporation of the powder or some components of it, as well as dissolution and phase transformations [19]. Due to this complex nature of the HVOF technique, controlling and optimizing the process, in order to achieve the desired coating, is a highly challenging task. To cope with this challenge, different approaches (e.g., design of experiments [DOE], numerical simulation, and machine learning [ML]) have all been proposed.

1.3.1. Statistic optimization methods

Statistical optimization methods have been widely employed to obtain a polynomial regression equation, which expresses the influence of process parameters on the response and to distinguish the major and minor factors. In terms of these kinds of statistic methods, DOE methods are widely employed, which include the Taguchi design method, analysis of variance (ANOVA), two-level factorial DOE, response surface modeling (RSM), and the analytic hierarchy process (AHP) method.

The Taguchi method is the most frequently used, and this is often used together with statistical ANOVA. This method identifies the influence of process parameters on output response, using the minimum number of the experiment. Numerous applications of the Taguchi method have been employed in the preparation of HVOF-sprayed coatings, which have been reported in recent years. For example, L. Qiao *et al.* adjusted the three process parameters (stand-off distance, kerosene [fuel], and oxygen flow rate) to optimize coatings' porosity, using the Taguchi design method [55]. Their results reveal that the important sequence of the spray parameters is kerosene flow > stand-off distance > oxygen flow rate. A similar method and analysis was conducted by Y. Qin *et al.*, but with different feedstock. Their results show that the significance of spray parameters in terms of determining the porosity of the coatings is in the order of spray distance > oxygen flow > kerosene flow [56]. Considering the different spraying system, feedstock, and application, a study conducted by A. S. Praveen *et al.* demonstrates that the important sequence of the spray parameters, in order to obtain better erosion resistance of coatings, is stand-off distance > powder feed rate > fuel flow rate > oxygen flow rate [57]. S. Nourouzi *et al.* have also employed the Taguchi method to investigate the effect of the main process parameters on particle characteristics and residual stresses, concluding that the stand-off distance and Oxygen/Fuel (O/F) ratio are the most effective factors [58].

Although the Taguchi method is the most widely used, two-level factorial DOE and RSM are also frequently used [59-61]. For example, two-level factorial DOE, together with ANOVA, has been employed to determine preferred optimized settings to achieve high crystallinity and purity of HA coatings [59]. K. Murugan has studied the influence of process parameters on coatings' hardness via RSM, summarizing that the oxygen flow rate has a predominating effect, followed by the fuel flow rate, powder feed rate, and then stand-off distance [62].

Though DOE optimization methods have been widely used to identify the sequence of

importance for variables in the HVOF spray process, they may not be able to achieve precise optimal parameters. This is because coating quality is usually influenced by a combined effect of several HVOF process parameters.

1.3.2. Numerical simulation optimization methods

The HVOF thermal spray process is extremely complex, with regards to its description in a theoretical model, since the process involves combustion, turbulence, compressible flow, multi-components, multiphase interactions, subsonic/supersonic transition, droplet deformation, and solidification. Mathematical/numerical modeling and simulation are also widely employed to simulate and control the spray process, as the fluid physics during the spraying procedure are difficult to research experimentally. The HVOF thermal spray process involves four main physical-chemical processes, which occur in the thermal and flow field [22]:

- I. The transformation of the gas's chemical energy into thermal energy by fuel oxidation in the combustion chamber.
- II. The conversion of the gas flows' thermal energy into kinetic energy by expansion through the nozzle, as well as the transfer of energy from the gas to the particles during this expansion process.
- III. The free jet flow field, whose flow patterns strongly depend on the difference between the pressure at the nozzle outlet and the atmospheric pressure.
- IV. When the coating is deposited, the particles' kinetic and thermal energy are converted into the work of viscous deformation and surface energy.

Various mathematical/numerical models have been constructed to study the complex flow physics, combustion chemistry, flame formation, and propagation involved in thermal spraying processes [63, 64]. The integral HVOF procedure, including the combustion processes, the heat-, mass, and momentum interactions between the flame, the suspension droplets (including vaporization), and the solid spray particles, has been modeled and analyzed by E. Dongmo, *et. al* [65]. E. Dongmo, *et. al* has also developed a 3D modeling and simulation approach to solve the two-phase supersonic, turbulent, and reacting flow, with under-expanded fluid conditions at the exit of the nozzle [22].

Nevertheless, numerical modeling has difficulties modeling real behaviors, due to the complex multi-physical phenomenon that occurs during the thermal spray process. Furthermore, modeling is significantly dependent on the hardware characteristics, such as the nozzle geometry, which limits its promotion.

1.3.3. ML optimization methods

ML is the scientific study of algorithms and statistical models that computer systems use to perform specific tasks. This relies on patterns and inference, instead of explicit instructions [66]. ML algorithms can be classified into three main categories: supervised learning, unsupervised learning, and reinforced learning (all of which are outlined in Figure 1.15) [67]. This has been widely employed for various applications, parts of which are indicated in Figure 1.15.

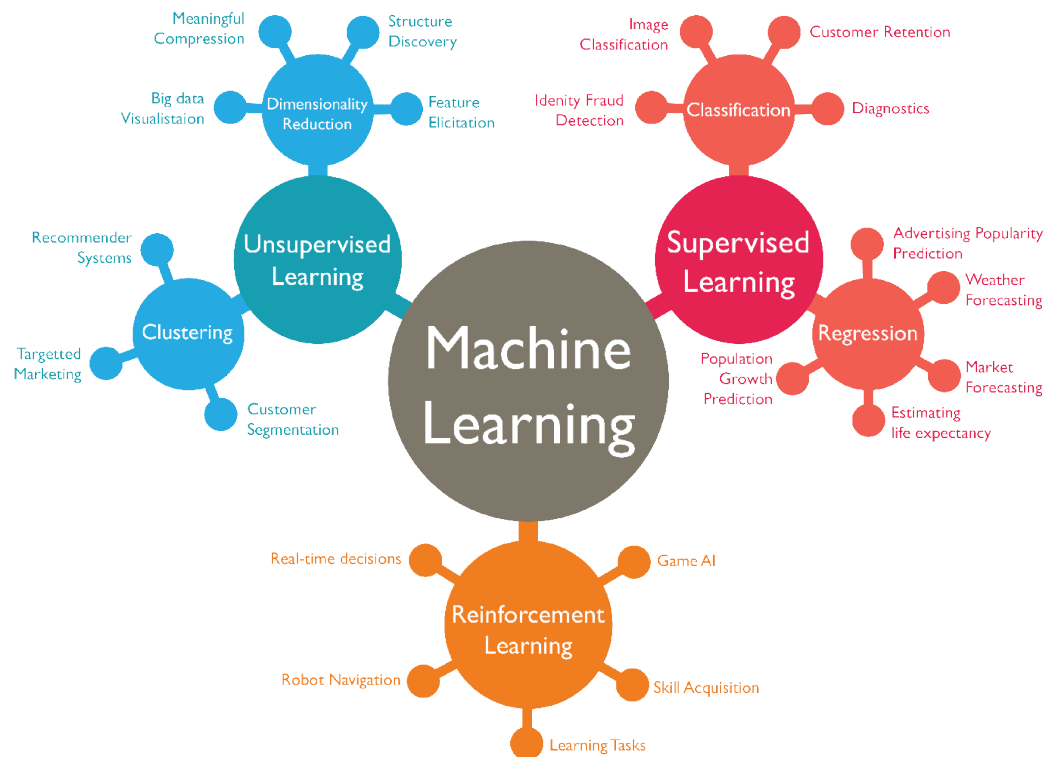


Figure 1.15 Machine learning algorithms [67]

Recently, ML has also drawn considerable attention from the field of thermal spray technology, particularly the artificial neural network (ANN) model. An ANN model is a computing model that can self-regulate and fit various nonlinearities in a data series through training and learning, which results in obtaining high-quality and efficient optimal conditions for manufacturing processes [68]. Therefore,

the ANN model is now increasingly employed to investigate the thermal spray process.

Thermal spraying technology processes contain complex chemical and thermodynamic reactions, which need to be researched using a powerful computational model, such as the ANN model. However, it is difficult and expensive to capture sufficient datasets for thermal spraying processes and coatings, particularly in terms of collecting sufficient data about coating properties. Therefore, the application of the shallow ANN model, which normally contains less than three hidden layers to facilitate relatively less data applications, has also attracted increased attention in the field of the thermal spraying technique.

The ANN model has been increasingly employed to investigate the thermal spray process, especially in the APS process. The initial idea for the neural network implementation of APS was presented by Einerson *et al.* [69]. Subsequently, many researchers have explored the applications of ANN models in the APS process. Significant works in this literature field are described in [Table 1.4](#).

S. Guessasma *et al.* have comprehensively investigated the relationships among APS process parameters, particle characterization, and coatings' performance in the Al_2O_3 –13wt% TiO_2 feedstock. They examined the influence of APS processing parameters on in-flight particle characteristics in [70, 71]. A detailed introduction to the construction and implementation of the ANN model was also presented in [72]. The optimization steps of an ANN model were discussed, considering different types of ANN architecture, learning paradigms, transfer function, performance function, and ANN structure [73]. Analysis and prediction of coatings' properties and the deposit process was conducted, considering the impact of APS process parameters, such as coatings' microstructure and hardness [74], young modulus, and interfacial toughness [75], as well as coatings' porosity [76], deposit profile (footprints) [77], and heat flux during the process [78].

A. F. Kanta *et al.* implemented both the ANN model and fuzzy logic (FL) to predict coatings' porosity [79] and in-flight particle characteristics [80], as a function of APS process parameters. They report that the ANN model is superior than that of FL, with regard to the prediction and simulation concept. Conversely, FL represents a better asset in the field of system control. Later, these authors established a coating's structural control system that considers an optimized ANN model, in which process parameters were considered as output variables [81]. Finally, they developed an expert system

that allows full APS process control, on the basis of pre-defined rules, which combines the ANN model for prediction and FL operators for control [82].

In order to evaluate the network's performance for the APS process, T.A. Choudhury *et al.* provide a detailed illustration of the ANN model's design and network optimization procedures, as well as database handling, expansion steps, and analysis of the predicted values with respect to the experimental ones [83, 84]. These authors also used and optimized the ANN model to predict the output of in-flight particle characteristics for the APS process, from the power and injection parameters [85].

Other researchers have also undertaken attempts that apply ANN models to the APS process, as listed in Table 1.4. All of the literature indicates that the multilayer neural network structure, which features a back-propagation algorithm, is capable of modeling the APS process and of concurrently predicting in-flight particle characteristics. A shallow network, which contains hidden layers that are less than or equal to three, have also been widely applied.

Table 1.4 Examples of ANN models used in APS

Author	Particle material	Inputs	Targets
S. Guessasma <i>et al.</i> [71]	Al ₂ O ₃ -13wt% TiO ₂	Arc current intensity, stand-off distance, injector diameter, carried gas flow rate, H ₂ flow rate, and Ar flow rate	Particle temperature, particle velocity, and particle diameter
L. Wang <i>et al.</i> [86]	WC-12%Co	Arc current intensity, H ₂ flow rate, and Ar flow rate for model 1; Arc current intensity, H ₂ flow rate, Ar flow rate, particle temperature, and particle velocity for model 2	Particle temperature and particle velocity for model 1; coating porosity and hardness for model 2
A. F. Kanta <i>et al.</i> [79]	Al ₂ O ₃ -13wt% TiO ₂	Arc current intensity, total gas(H ₂ + Ar), and H ₂ content(H ₂ /Ar)	Coating porosity

M. D. Jean <i>et al.</i> [87]	Zirconia	Spraying layers, voltage, Arc current, travel speed, stand-off distance, powder feed rate, carried gas flow rate, and primary gas flow rate	Wear volume
T.A. Choudhury <i>et al.</i> [83]	Data from Ref [71]	Arc current intensity, Ar gas flow rate, H ₂ flow rate, carrier gas flow rate, stand-off distance, and injector diameter	Particle velocity, particle temperature, and particle diameter
S. Datta <i>et al.</i> [88]	Ni-5wt% Al	Primary gas flow rate, stand-off distance, powder flow rate, and arc current	Thickness, porosity, and microhardness of the coatings
Taikai LIU <i>et al.</i> [89]	Al ₂ O ₃ -13wt% TiO ₂	Particle temperature and particle velocity	Coating porosity
Chun-Ming Lin <i>et al.</i> [90]	CoMoCrSi	Spray distance, chamber pressure, current, Ar gas flow rate, and H ₂ gas flow rate	Coating porosity
A. H. Pakseresht <i>et al.</i> [91]	Yttria-Stabilized Zirconia	Input power, primary gas flow rate, stand-off distance, powder feed rate, and the carrier gas flow rate	deposition efficiency, tensile bond strength, hardness, and surface roughness

Most existing studies concentrate on the APS process, but increasing attention has also been given to other thermal spray technologies, albeit to a lesser extent. The APS technique has received the most attention, followed by HVOF spray. M. Cherigui *et al.* created two ANN models to research the magnetic properties of a HVOF-sprayed FeNb alloy: Model A was employed to relate process parameters to microstructure features, while Model B was used to relate process parameters to magnetic properties [92]. This study also explored the effect of HVOF process parameters on coating porosity and on the magnetic properties of FeNb coatings, using the ANN model, in [93]. R. Hamzaoui *et al.* have also studied the magnetic properties of Fe-Ni and Fe-Si alloys, using ANN models to research the correlation between process parameters in both milling and spraying

techniques, with respect to magnetic parameters [94]. G. Zhang *et al.* implemented an ANN model to predict the HVOF-sprayed NiCrAlY coating's structural attributes (porosity, hardness) in terms of the function of the process parameters (oxygen/fuel gas stoichiometric ratio and stand-off distance) [95]. Spyros Kamnis *et al.* conducted an interesting study from the perspective of airborne acoustic emission during the HVOF spray process, using an ANN model, in order to emphasize the considerable influence of the spray distance and powder feed rate on coatings' microhardness [96]. An ANN model has also been utilized to predict the rate of erosive wear for WC-CoCr coatings that are deposited by flame spray (FS) and HVOF, in research conducted by M. A. R. Mojena *et al.* This study conclude that microhardness and fracture toughness work together to apply the greatest influence over the erosive rate, followed by porosity [97].

Limited research investigates the HVOF spray process by applying the ANN model. Thus, a comprehensive understanding of the relationships among HVOF process parameters, the behavior of in-flight particles, and coatings' performance is needed, to thoroughly examine the HVOF process through an ANN methodology. Additionally, the relative importance of each input variable in the ANN model has seldom been studied for the thermal spray process. In this thesis, mean impact value (MIV)-based analysis is conducted to quantitatively explore the relative importance of each input variable for the improvement of the mechanical performance of coatings, as described in [Section 1.5](#).

1.4. Artificial intelligence

Artificial intelligence (AI), an ever-evolving area of computer science, is devoted to production software that is capable of sophisticated and intelligent computations, similar to those that the human brain routinely performs. AI includes methods, tools, and systems that are dedicated to simulating human methods of logical and inductive knowledge acquisition, as well as reasoning of brain activity to solve problems [98]. Although AI is undoubtedly multifaceted, there are two main categories of AI developments. The first includes methods and systems that simulate human experience and draw conclusions from a set of rules, such as expert systems. The second includes systems that model the way the brain works; for example, ANNs [98].

1.4.1. History of the artificial neural network

ANNs have a long history, with two periods of inactivity. ANNs were first created by Warren McCulloch and Walter Pitts in 1943, who developed a computational model for neural networks that was based on algorithms called threshold logic [99]. This model paved the way for research's split into two approaches: one focusing on biological processes and the other focusing on the application of neural networks to AI.

Since their initial development, an increasing number of sophisticated concepts and related architectures have been created. For instance, D. O. Hebb created a learning hypothesis in the late 1940s that is known as Hebbian learning, which is unsupervised learning based on the mechanism of neural plasticity [100]. This evolved into models for long-term potentiation, when researchers began applying these ideas to computational models. Various neural network computational machines were created for simulation [101, 102]. In a subsequent study, Rosenblatt created the first perceptron, an algorithm for pattern recognition. In his study, Rosenblatt described circuitry that is not in the basic perceptron, with the help of mathematical notation [103]. Later, in 1962, Wiesel developed the adaptive linear neuron (ADALINE)[104]. The first generation of neural networks was fundamentally limited, in terms of what these networks could learn to do. Research stagnated during the 1970s (the first period of inactivity), as critical focus turned to the “exclusive or” (XOR) problem [105]. Neural network research slowed until computers achieved far greater processing power.

The following period focused on the emergence of more advanced neural networks, such as multilayer back-propagation neural networks, convolutional neural networks (CNNs), and long short-term memory (LSTMs) for recurrent neural networks (RNNs). A key trigger of this renewed interest in neural networks and learning was the back-propagation algorithm, which used back-propagation of the error signal to obtain derivatives for learning [106]. This distributed the error term back up through the layers by modifying the weights at each node. This, in turn, enabled the practical training of multilayer networks. During this second period of inactivity, the support vector machine (SVM), which is an extremely clever type of perceptron, was developed by Cortes and Vapnik [107]. It went on to gradually overtake neural networks. Therefore, many researchers turned their critical attention to researching the SVM, instead of neural networks with multiple adaptive hidden layers, since an SVM performs better with less computational time and training [106].

The progress of graphics processing units (GPUs) and the storage of big data prompted renewed attention in neural networks. In 2006, Hinton *et al.* proposed a new training method (called layer-wise-greedy-learning), which marked the birth of deep learning techniques [108]. Generally speaking, the deep learning algorithm consists of a hierarchical architecture with many layers, each of which constitutes a nonlinear information processing unit. The reasons for deep learning's popularity is twofold. From one perspective, the development of big data analysis techniques suggests that the overfitting problem in training data can be partially solved, while, conversely, the pre-training procedure that occurs before unsupervised learning assigns non-random initial values to the network. Therefore, a better local minimum can be reached after the training process and a faster converge rate can be achieved [109]. Until now, various deep neural networks have been developed, which can be classified into the following categories: restricted Boltzmann machines (RBMs), deep belief networks (DBNs), autoencoders (AEs) networks, and deep CNNs. In addition, deep probabilistic neural networks, deep fuzzy neural networks, and generative adversarial networks (GANs) can also be considered as other categories [105].

1.4.2. Principle of the artificial neural network

ANNs are computational models that are inspired by, but not identical to, networks of biological neurons that constitute animal brains. As displayed in [Figure 1.16](#), the dendrites act as the input vector, which permits the cell body (or soma) to take in signals from a large number of neighboring neurons. Axons carry signals from the neuron to other cells. The cell body, which acts as the summation function, processes the signals from the dendrites. The interaction of the cell body and the environment cause the neuron to pump either sodium or potassium in and out, increasing or decreasing the neuron's electrical potential. Once the neuron's electrical potential reaches a certain potential (a threshold), the neuron "fires," creating an action potential that travels down the axons to the synapses and other neurons [110]. The action potential is created when the voltage across the cell membrane of the neuron becomes large enough to fire the cell, thus creating a spike through the axon to other neurons and cells. If the stimulus causing the buildup of voltage is low, then it will take a long time to fire the neuron. If it is high, the neuron fires much faster.

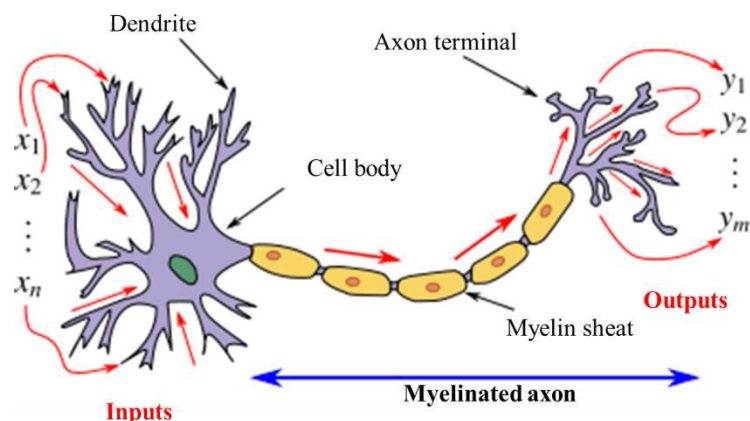


Figure 1.16 Neuron and myelinated axon, with signal flow from inputs at dendrites to outputs at axon terminals [111]

Similarly, an ANN can be described as mapping an input space to an output space, based on a collection of operating elements called neurons (analogous to biological neurons) and connections called weights (analogous to synapses in a biological brain). During the action, the neurons send signals to other neurons by sending an action potential down the axon, which is modeled by a transfer function that mimics the firing rate of the neuron's action potential. Different inputs to the neuron may have different levels of relevance, including whether the neuron should fire, which results in them having smaller or greater impact. This is realized by adjusting the weight. Therefore, the neuron can be regarded as a small computing engine that takes in inputs, processes them, and transmits an output. Figure 1.17 depicts an elementary neuron with R inputs $p_1 p_2 \dots p_R$, a corresponding transfer function f , and an output a . Each input is weighted with an appropriate w . The sum of the weighted inputs and the bias forms the input to the transfer function. The main function of bias is to provide every neuron with a trainable constant value (in addition to the normal inputs that the neuron receives). Neurons can use any differentiable transfer function to generate their output. The output of the neuron in Figure 1.17 can be given by:

$$a = f(\sum_{i=1}^R w_{1,i} p_i + b) \quad \text{Eq. (1.1)}$$

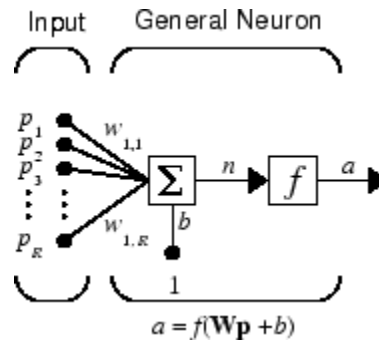
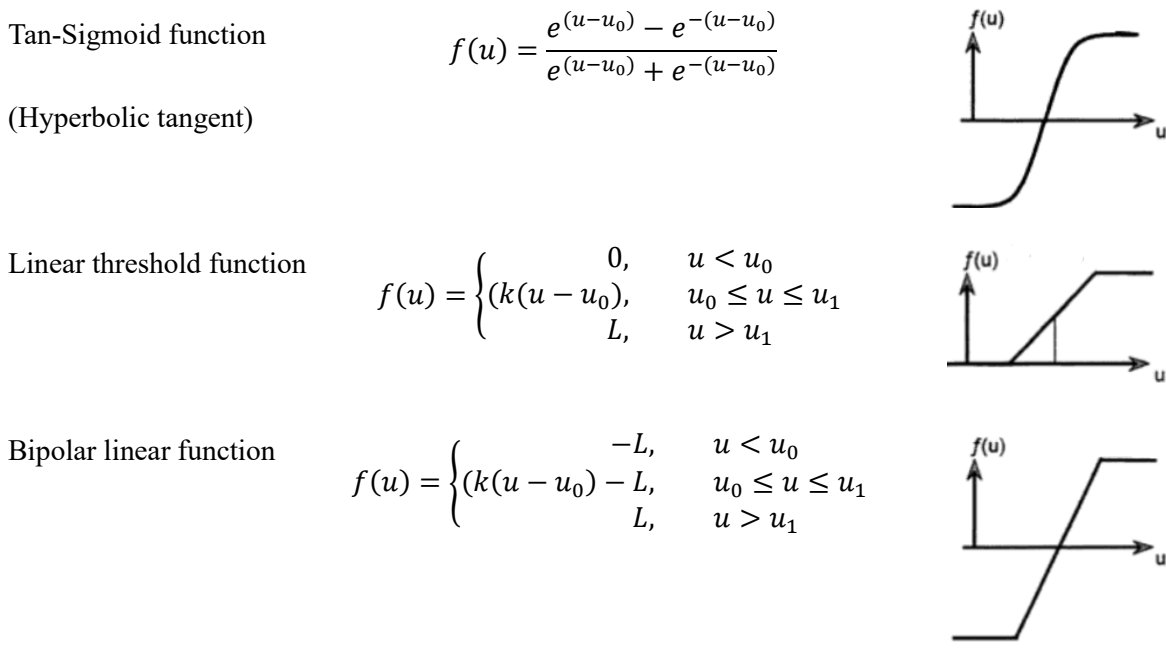


Figure 1.17 The structure of an elementary artificial neuron with R inputs [112]

The purpose of the transfer function is to introduce non-linearity into the output of a neuron. This is important because most real-world data is nonlinear, which means neurons need to learn these nonlinear representations. The different available transfer functions are depicted in Table 1.5; the Log-Sigmoid transfer function, the Tan-Sigmoid transfer function, and the linear transfer function are the most commonly used for multilayer networks. Sigmoid output neurons are often used for pattern-recognition problems, while linear output neurons are used for function-fitting problems.

Table 1.5 Three different types of transfer function: step, sigmoid, and linear, in unipolar and bipolar formats [110]

Name	Value	Representation
Step function	$f(u) = \begin{cases} 0, & u < u_0 \\ L, & u \geq u_0 \end{cases}$	
Bipolar step function	$f(u) = \begin{cases} -L, & u < u_0 \\ L, & u \geq u_0 \end{cases}$	
Log-Sigmoid function (Logistic)	$f(u) = \frac{L}{1 + e^{-k(u-u_0)}}$	



1.4.3. Feedforward neural network

The feedforward neural network was the first and simplest type of artificial neural network ever to be devised [113]. This is an ANN in which connections between nodes do not form a cycle, which means that there are no cycles or loops in the network. Information only moves in a forward direction, flowing from the input nodes, through the hidden nodes (if any), to the output nodes, as displayed in Figure 1.18. The feedforward neural network can have a single-layer or multilayer structure, and the multilayer perceptron (MLP) is one of the most utilized feedforward ANN types for nonlinear function approximation tasks. This uses a variety of learning techniques, the most popular of which is back-propagation.

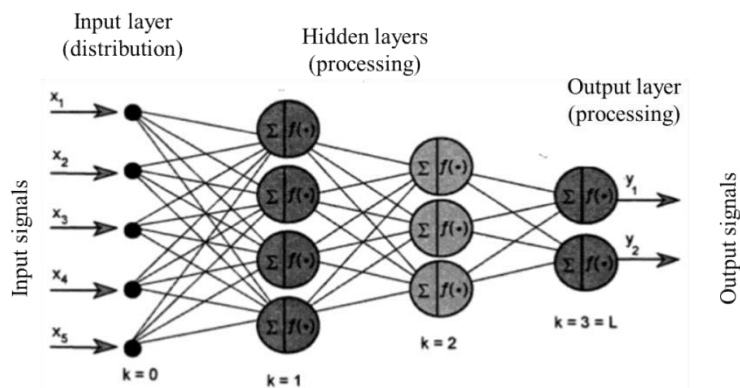


Figure 1.18 Multilayer feedforward neural network [110]

The back-propagation algorithm, as a form of supervised training, is a particular application of the classical gradient-descendant optimization technique [114]. By applying a supervised learning method, the network must be provided with both sample inputs and experimental outputs. The predicted outputs are compared with the experimental outputs for given inputs. The back-propagation training algorithm takes a calculated error and adjusts the weights of the various layers backward from the output layer to the input layer, in order to reduce the value of error. Information is delivered to the output if it achieves the target; otherwise, it is backpropagated. The target value will only be achieved if the weighted sum meets the minimum threshold and hence feeds forward or back-propagates for further processing [115].

The multilayer feedforward neural network can be used for both function-fitting and pattern-recognition problems. With the addition of a tapped delay line, it can also be used for prediction problems. In this work, the MLP neural network, characterized by the back-propagation algorithm, has been chosen to analyze, predict, and optimize the HVOF spray process and HVOF-sprayed coatings. Details of this procedure to design an ANN model are presented in the following section.

1.4.4. Procedure for designing an ANN model

In this thesis, the MATLAB software has been selected to implement the design of the ANN model. The detailed workflow for designing a general neural network consists of seven primary steps, which can be summarized as:

1. Collecting and preparing data;
2. Creating the network;
3. Configuring the network;
4. Initializing the weights and biases;
5. Training the network;
6. Validating the network (post-training analysis);
7. Applying the network.

Data collection and preparation

The first step is to collect data, which is critical to successfully designing an ANN model, but which might occur outside the framework of designing an ANN model. Multilayer networks can be trained to perform well, within the range of inputs for which they have been trained. However, they are not able to accurately predict beyond this range. Therefore, it is essential that the collected data covers the range of inputs for which the network will be used.

After the data has been collected, the normalization of the data should be carried out, as this will help improve the training efficiency of the neural network. Generally, both the input vectors and the target vectors need to be normalized, in order to avoid the calculation error related to different parameter magnitudes. Subsequently, the network output will also fall into a normalized range, which can then be reverse transformed back into the units of the original target data, when the network is applied in the field. Both the pre-processing block (which appears between the input and the first layer of the network) and the post-processing block (which appears between the last layer of the network and the output) should be considered, as displayed in [Figure 1.19](#). The most common pre-processing and post-processing functions and their algorithms in the MATLAB software are listed in [Table 1.6](#).

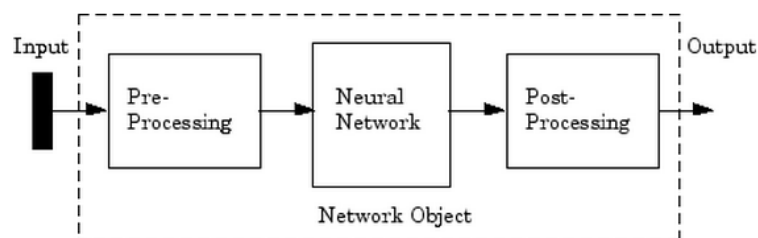


Figure 1.19 The pre-processing and post-processing block of the network workflow [112]

Subsequently, the dataset needs to be divided into three subsets: a training set, validation set, and test set. The training set is used to compute the gradient and to update the network weights and biases. During the initial stage of training, the error in the training and validation set normally decreases. However, the validation error typically begins to rise as the overfitting of the network occurs. Therefore, the error in the validation set is monitored during the training process, and the network weights and biases are saved at the minimum of the validation set error. The test set error is not used during the training. However, if the test set error reaches a minimum iteration number that is

significantly different from that of the validation set error, this might indicate a poor division of the dataset. Four functions for dividing the data, which are provided by MATLAB, are listed in [Table 1.7](#).

Table 1.6 The most common pre-processing and post-processing functions and their algorithms in MATLAB [112]

Function	Description
mapminmax	Normalize inputs/targets to fall in the range $[-1, 1]$
mapstd	Normalize inputs/targets to have zero mean and unity variance
processpca	Extract principal components from the input vector
fixunknowns	Process unknown inputs
removeconstantrows	Remove inputs/targets that are constant

Table 1.7 Four functions for dividing data, which are provided in MATLAB [112]

Function	Description
dividerand	Divide the data randomly (default)
divideblock	Divide the data into contiguous blocks
divideint	Divide the data using an interleaved selection
divideind	Divide the data by index

Creating and configuring the network

In the second step, the network needs to be created and configured with appropriate parameters, which includes selecting the number of hidden layers and the number of neurons in each hidden layer, as well as choosing the training function and transfer function.

For a multilayer feedforward network, more layers might learn complex relationships more quickly, whereas one hidden layer can produce excellent results for simple or linear problems. However, two hidden layers may also be considered, if the results of one are not adequate. The general suggestion is to start with two layers for most problems, which can then be increased to three

layers if the performance with two layers is not satisfactory. Increasing the number of neurons in the hidden layer increases the power of the network, but requires more computation and is more likely to produce overfitting.

The selection of a suitable training function for a given problem depends on many factors, including the complexity of the problem, the number of data points in the training set, the number of weights and biases in the network, the error goal, and whether the network is being used for pattern recognition (discriminant analysis) or function approximation (regression) [112]. Varied training functions are provided for different problems in MATLAB. [Table 1.8](#) outlines a part of the training function. The “trainlm” function, which performs better on function fitting (nonlinear regression) problems, is generally the fastest training function, but “trainbfg” is also distinctly fast. However, both of these functions tend to be less efficient for large networks (with thousands of weights), since they require more memory and more computation time. The “trainscg” and “trainrp” functions are usually chosen to train large networks and for pattern-recognition networks.

Table 1.8 Part of the training function in MATLAB [112, 116]

Function	Description
trainlm	Levenberg-Marquardt back-propagation
trainbfg	BFGS quasi-Newton back-propagation
trainbr	Bayesian regularization back-propagation
trainrp	Resilient back-propagation
traingdx	Gradient descent with momentum and adaptive learning rate back-propagation
trainscg	Scaled conjugate gradient back-propagation

Training the network and evaluating its performance

The network is ready for training once the network is configured and the weights and biases are initialized. The training process involves tuning the values of the weights and biases of the network to optimize network performance. There are two different ways to perform this training process: the incremental mode and the batch mode. In the incremental mode, the gradient is computed and the

weights are updated after each input is applied to the network. In the batch mode, all inputs in the training set are applied to the network before the weights are updated. For most problems, batch training is significantly faster and produces smaller errors than incremental training, in a MATLAB environment.

The network performance function is used to measure the network's performance, parts of which are listed in Table 1.9. In MATLAB, the correct evaluation value R is an indication of the relationship between the outputs and targets. If $R = 1$, this indicates that there is an exact linear relationship between outputs and targets. If R is close to zero, there is no linear relationship between outputs and targets. Therefore, an ANN model with a higher value R is more capable of performing high-quality predictions.

Table 1.9 Part of the network performance function in MATLAB [112]

Name	Description	Function
mse	Mean squared normalized error performance function	$mse = \frac{1}{N} \sum_{i=1}^N (t_i - a_i)^2$
mae	Mean absolute error performance function	$mae = \frac{1}{N} \sum_{i=1}^N t_i - a_i $
sse	Sum squared error performance function	$sse = \sum_{i=1}^N (t_i - a_i)^2$
sae	Sum absolute error performance function	$sae = \sum_{i=1}^N t_i - a_i $

, where t_i is the target, a_i is the network predicted result, and N is the number of datasets.

Validation and application of the network

The network's performance can be checked and evaluated, in order to determine any necessary changes to the training process, the network architecture, or the datasets, all of which will improve the network's accuracy. There are several approaches to improving the results in the MATLAB environment:

1. Re-initializing the network and training;
2. Increasing the number of hidden neurons to provide the network with more flexibility;
3. Trying different training functions;
4. Enlarging the dataset.

Once the network is trained and validated, the network can be used to calculate the network response to any input. However, it is important to note that each time a neural network is trained. This can result in a different solution, due to different initial weight and bias values and different divisions of data. Consequently, different neural networks that have been trained on the same problem can produce different outputs for the same input. Thus, retraining the network several times is suggested, in order to ensure strong neural network accuracy.

1.5. MIV analysis approach

It is important to introduce an appropriate method to analyze the significance of each input variable, which must take the error of the input variables into account. MIV-based analysis provides such a method, as it allows an ANN model to explore the relative importance of each input variable, which ultimately improves its prediction performance.

The MIV method was first proposed by Dombi in the biomedical field. It is used to choose parameters or analyze independent variables that significantly impact dependent variables in an ANN [117]. This is currently widely employed to quantitatively feature analysis in ML applications [118, 119]. The process of MIV-based analysis is as follows [120]:

The first step is to obtain the trained ANN model with the input (X) in the dataset, as shown in Eq. (1.2).

$$X = \begin{bmatrix} x_{11} & x_{12} & \cdots & x_{1m} \\ x_{21} & x_{22} & \cdots & x_{2m} \\ \vdots & \vdots & \ddots & \vdots \\ x_{n1} & x_{n2} & \cdots & x_{nm} \end{bmatrix} \quad \text{Eq. (1.2)}$$

, where n is the number of the input variables and m is the number of values of each variable.

Then, the i th variable in X is added and reduced by 10%, to form two new inputs, $X_i(1)$ and $X_i(2)$, as displayed in Eq. (1.3–1.4).

$$X_i(1) = \begin{bmatrix} x_{11} & x_{12} & \dots & x_{1m} \\ \vdots & \vdots & & \vdots \\ x_{i1}(1 + 10\%) & x_{i2}(1 + 10\%) & \dots & x_{im}(1 + 10\%) \\ \vdots & \vdots & & \vdots \\ x_{n1} & x_{n2} & \dots & x_{nm} \end{bmatrix} \quad \text{Eq. (1.3)}$$

$$X_i(2) = \begin{bmatrix} x_{11} & x_{12} & \dots & x_{1m} \\ \vdots & \vdots & & \vdots \\ x_{i1}(1 - 10\%) & x_{i2}(1 - 10\%) & \dots & x_{im}(1 - 10\%) \\ \vdots & \vdots & & \vdots \\ x_{n1} & x_{n2} & \dots & x_{nm} \end{bmatrix} \quad \text{Eq. (1.4)}$$

Third, these two new inputs are used for simulation within the trained model. The simulated outputs, $Y_i(1)$ and $Y_i(2)$, which are based on $X_i(1)$ and $X_i(2)$, are obtained. The difference between $Y_i(1)$ and $Y_i(2)$ is calculated and defined as impact value I_i , as depicted in Eq. (1.5–1.7).

$$Y_i(1) = \begin{bmatrix} y_{11}(1) & y_{12}(1) & \dots & y_{1m}(1) \\ \vdots & \vdots & & \vdots \\ y_{k1}(1) & y_{k2}(1) & \dots & y_{km}(1) \\ \vdots & \vdots & \ddots & \vdots \\ y_{l1}(1) & y_{l2}(1) & \dots & y_{lm}(1) \end{bmatrix} \quad \text{Eq. (1.5)}$$

$$Y_i(2) = \begin{bmatrix} y_{11}(2) & y_{12}(2) & \dots & y_{1m}(2) \\ \vdots & \vdots & & \vdots \\ y_{k1}(2) & y_{k2}(2) & \dots & y_{km}(2) \\ \vdots & \vdots & \ddots & \vdots \\ y_{l1}(2) & y_{l2}(2) & \dots & y_{lm}(2) \end{bmatrix} \quad \text{Eq. (1.6)}$$

$$I_i = Y_i(2) - Y_i(1) \quad \text{Eq. (1.7)}$$

, where l is the number of the output variable.

Therefore, the MIV of the i th input variable on the k th output variable could be calculated according to Eq. (1.8). The sequence of the input variables is sorted according to their absolute MIVs.

$$MIV_i(k) = \frac{1}{m} \sum_{j=1}^m (I_i)_{kj} \quad \text{Eq. (1.8)}$$

The contribution rate to the k th output variable from the i th input variable can be further calculated as following [121]:

$$C_i(k) = \frac{|MIV_i(k)|}{\sum_{i=1}^n |MIV_i(k)|} * 100\% \quad \text{Eq. (1.9)}$$

Both the MIV and contribution rate (C) indicators can be applied to quantitatively characterize

the importance of the input variables. The higher the absolute MIV is, the more important the input variable will be. The C is derived from the MIV, in order to identify the contribution percentages of the input variables on the output variables. With these indicators, the ANN model can not only predict the outputs, but can also calculate the influence level of the input variables, which compensates for the deficiencies of the application of the ANN model in thermal spray technologies.

1.6. Research objectives

The above discussion highlights the need for a comprehensive understanding of the relationship among HVOF process parameters, the behavior of in-flight particles, and coatings' performance. As a result, the present work focuses on thoroughly investigating the HVOF spray process, by applying ANN models. In addition, MIV-based analysis will be conducted to quantitatively explore the relative importance of each input variable, in order to improve the mechanical performance of the coatings. This dissertation is structured into four parts.

In the first part, a recompiled control system for the HVOF spray will be developed to control and record the spraying process. In this system, control systems for the CDS torch and Diamond Jet 2700 torch will both be developed, taking different spraying requirements into consideration. This will also provide an interface to integrate ANN models into the HVOF control system, which will subsequently realize the "real-time" control of the spraying process. Experiments with varied process parameters will then be conducted, using this recompiled control system. The behaviors of in-flight particles will be monitored during the spraying process. Together with the coatings' performance, all of this data will be recorded and collected for further analysis and research.

In the second step, the behaviors of in-flight particles and the coatings' properties will be analyzed from the perspective of the HVOF spray technology. As the coatings' properties are sensitive to the behaviors of in-flight particles, which are mainly influenced by the processing parameters, it is useful to preliminarily analyze the relationship between them.

Third, the detailed construction and optimization of ANN models will be presented. Two ANN models will be created, trained, and tested, in order to thoroughly examine the HVOF spray process and HVOF-sprayed coatings. The ANN1 model will be used to relate the behaviors of in-flight

particles to the process parameters. The ANN2 model will then be applied, in order to research the influence of process parameters on the coatings' properties. Furthermore, MIV analysis will be conducted for both of the ANN models, in order to quantitatively analyze the significance of each input variable, taking the error of the input variables into account.

Finally, an intelligent HVOF spray system, which integrates ANN models to process and control the coatings, which will be constructed and optimized to realize the "on-line" regulating and optimizing of the coatings' quality. This system will be created based on the recompiled control HVOF system in the first step. In addition, this section will provide useful ideas about future constructions of an intelligent thermal spray system for other thermal spray technologies.

Reference of chapter 1

- [1] P.L. Fauchais, J.V. Heberlein, M.I. Boulos, *Thermal Spray Fundamentals: From Powder to Part*, Springer, New York, 2014.
- [2] A.S.M. Ang, N. Sanpo, M.L. Sesso, S.Y. Kim, C.C. Berndt, Thermal spray maps: material genomics of processing technologies, *Journal of thermal spray technology*, 22 (2013) 1170-1183.
- [3] C.-J. Li, A. Ohmori, Relationships between the microstructure and properties of thermally sprayed deposits, *Journal of thermal spray technology*, 11 (2002) 365-374.
- [4] Schematic of the thermal spray process, in, TCPP, <http://www.tcpp.fr/activities.html>.
- [5] Principle of thermal spray, in, *Advanced Coating*, <http://www.advanced-coating.com/english/spraying.htm>.
- [6] S. Siegmann, C. Abert, 100 years of thermal spray: About the inventor Max Ulrich Schoop, *Surface and Coatings Technology*, 220 (2013) 3-13 %@ 0257-8972.
- [7] H. Herman, *Treatise on Materials Science and Technology: Ultrarapid Quenching of Liquid Alloys*, Elsevier, 2012.
- [8] P. Fauchais, A. Vardelle, B. Dussoubs, Quo vadis thermal spraying?, *Journal of Thermal Spray Technology*, 10 (2001) 44-66 %@ 1059-9630.
- [9] P. Fauchais, Understanding plasma spraying, *Journal of Physics D: Applied Physics*, 37 (2004) R86 %@ 0022-3727.
- [10] T.F. Bernecki, *Thermal Spray Coatings: Properties, Processes and Applications*, Pittsburgh, (1991) 1992.
- [11] J.A. Browning, Highly concentrated supersonic liquified material flame spray method and apparatus, in, *Google Patents*, 1983.
- [12] M.L. Thorpe, H.J. Richter, A pragmatic analysis and comparison of HVOF processes, *Journal of Thermal Spray Technology*, 1 (1992) 161-170.
- [13] J.A. Browning, Hypervelocity impact fusion—a technical note, *Journal of Thermal Spray Technology*, 1 (1992) 289-292.
- [14] P. Fauchais, G. Montavon, Thermal and cold spray: Recent developments, in, *Trans Tech Publ*, 2008, pp. 1-59 %@ 0878493727.
- [15] J.A. Gan, C.C. Berndt, Thermal spray forming of titanium and its alloys, in: *Titanium Powder Metallurgy*, Elsevier, 2015, pp. 425-446.
- [16] S. Amin, H. Panchal, A review on thermal spray coating processes, *transfer*, 2 (2016).
- [17] P. Vuoristo, *Thermal spray coating processes*, (2014).
- [18] J. Kawakita, S. Kuroda, T. Fukushima, H. Katanoda, K. Matsuo, H. Fukanuma, Dense titanium coatings by modified HVOF spraying, *Surface and Coatings Technology*, 201 (2006)

1250-1255 %@ 0257-8972.

[19] M. Oksa, E. Turunen, T. Suhonen, T. Varis, S.-P. Hannula, Optimization and Characterization of High Velocity Oxy-fuel Sprayed Coatings: Techniques, Materials, and Applications, *Coatings*, 1 (2011) 17-52.

[20] J.R. Davis, *Handbook of Thermal Spray Technology*, ASM International, 2004.

[21] M. Ivosevic, R.A. Cairncross, R. Knight, Modeling of the solvent-free thermal spray deposition of polymer and polymer-ceramic composite coatings, (2005).

[22] E. Dongmo, M. Wenzelburger, R. Gadow, Analysis and optimization of the HVOF process by combined experimental and numerical approaches, *Surface and Coatings Technology*, 202 (2008) 4470-4478.

[23] F. Gärtner, T. Stoltenhoff, T. Schmidt, H. Kreye, The Cold Spray Process and Its Potential for Industrial Applications, *Journal of Thermal Spray Technology*, 15 (2006) 223-232.

[24] D. Sciti, L. Zoli, L. Silvestroni, A. Cecere, G.D. Di Martino, R. Savino, Design, fabrication and high velocity oxy-fuel torch tests of a C f -ZrB₂ - fiber nozzle to evaluate its potential in rocket motors, *Materials & Design*, 109 (2016) 709-717.

[25] Q. Wang, S. Luo, S. Wang, H. Wang, C.S. Ramachandran, Wear, erosion and corrosion resistance of HVOF-sprayed WC and Cr₃C₂ based coatings for electrolytic hard chrome replacement, *International Journal of Refractory Metals and Hard Materials*, 81 (2019) 242-252.

[26] M. Mardali, H. Salimijazi, F. Karimzadeh, B. Luthringer-Feyerabend, The effect of an MgO intermediate layer on a nanostructured HA coating fabricated by HVOF on an Mg alloy, *Surface and Coatings Technology*, 374 (2019) 1071-1077.

[27] R.S. Lima, K.A. Khor, H. Li, P. Cheang, B.R. Marple, HVOF spraying of nanostructured hydroxyapatite for biomedical applications, *Materials Science and Engineering: A*, 396 (2005) 181-187.

[28] X.-T. Luo, G.M. Smith, Y. Wang, E. Gildersleeve, S. Sampath, C.-J. Li, Cracking induced tribological behavior changes for the HVOF WC-12Co cermet coatings, *Ceramics International*, 45 (2019) 4718-4728.

[29] P. Mi, T. Wang, F. Ye, Influences of the compositions and mechanical properties of HVOF sprayed bimodal WC-Co coating on its high temperature wear performance, *International Journal of Refractory Metals and Hard Materials*, 69 (2017) 158-163.

[30] M.S. Lamana, A.G.M. Pukasiewicz, S. Sampath, Influence of cobalt content and HVOF deposition process on the cavitation erosion resistance of WC-Co coatings, *Wear*, 398-399 (2018) 209-219.

[31] B.S. Mann, V. Arya, A.K. Maiti, M.U.B. Rao, P. Joshi, Corrosion and erosion performance of HVOF/TiAlN PVD coatings and candidate materials for high pressure gate valve application, *Wear*, 260 (2006) 75-82.

[32] W. Tillmann, E. Vogli, I. Baumann, G. Kopp, C. Weihs, Desirability-Based Multi-Criteria

Optimization of HVOF Spray Experiments to Manufacture Fine Structured Wear-Resistant 75Cr3C2-25(NiCr20) Coatings, *Journal of Thermal Spray Technology*, 19 (2009) 392-408.

[33] Y. Bai, X. Li, L. Xing, Z. Wang, Y. Li, A novel non-skid composite coating with higher corrosion resistance, *Ceramics International*, 43 (2017) 15095-15106.

[34] K. Bobzin, L. Zhao, M. Öte, T. Königstein, M. Steeger, Impact wear of an HVOF-sprayed Cr₃C₂-NiCr coating, *International Journal of Refractory Metals and Hard Materials*, 70 (2018) 191-196.

[35] W. Zhou, K. Zhou, C. Deng, K. Zeng, Y. Li, Hot corrosion behavior of HVOF-sprayed Cr₃C₂-WC-NiCoCrMo coating, *Ceramics International*, 43 (2017) 9390-9400.

[36] V. Matikainen, G. Bolelli, H. Koivuluoto, P. Sassatelli, L. Lusvarghi, P. Vuoristo, Sliding wear behaviour of HVOF and HVAF sprayed Cr₃C₂-based coatings, *Wear*, 388-389 (2017) 57-71.

[37] W. Zhou, K. Zhou, Y. Li, C. Deng, K. Zeng, High temperature wear performance of HVOF-sprayed Cr₃C₂-WC-NiCoCrMo and Cr₃C₂-NiCr hardmetal coatings, *Applied Surface Science*, 416 (2017) 33-44.

[38] D.G. Bhosale, W.S. Rathod, S.W. Rukhande, Sliding wear behavior of high velocity oxy-fuel sprayed WC-Cr₃C₂-Ni coating for automotive applications, *Materials Today: Proceedings*, (2019).

[39] Shabana, M.M.M. Sarcar, K.N.S. Suman, S. Kamaluddin, Tribological and Corrosion behavior of HVOF Sprayed WC-Co, NiCrBSi and Cr₃C₂-NiCr Coatings and analysis using Design of Experiments, *Materials Today: Proceedings*, 2 (2015) 2654-2665.

[40] T.S. Sidhu, S. Prakash, R.D. Agrawal, Hot corrosion studies of HVOF NiCrBSi and Stellite-6 coatings on a Ni-based superalloy in an actual industrial environment of a coal fired boiler, *Surface and Coatings Technology*, 201 (2006) 1602-1612.

[41] C.D. Prasad, S. Joladarashi, M.R. Ramesh, M.S. Srinath, B.H. Channabasappa, Effect of microwave heating on microstructure and elevated temperature adhesive wear behavior of HVOF deposited CoMoCrSi-Cr₃C₂ coating, *Surface and Coatings Technology*, 374 (2019) 291-304.

[42] T. Sahraoui, H.I. Feraoun, N. Fenineche, G. Montavon, H. Aourag, C. Coddet, HVOF-sprayed Tribaloy©-400: microstructure and first principle calculations, *Materials Letters*, 58 (2004) 2433-2436.

[43] Z. Yuduo, Y. Zhigang, Z. Chi, L. Hao, Effect of Rhenium Addition on Isothermal Oxidation Behavior of Tribaloy T-800 Alloy, *Chinese Journal of Aeronautics*, 23 (2010) 370-376.

[44] L. Qiao, Y. Wu, S. Hong, J. Cheng, Ultrasonic cavitation erosion mechanism and mathematical model of HVOF sprayed Fe-based amorphous/nanocrystalline coatings, *Ultrason Sonochem*, 52 (2019) 142-149.

[45] J. Zhang, M. Liu, J. Song, C. Deng, C. Deng, Microstructure and corrosion behavior of Fe-based amorphous coating prepared by HVOF, *Journal of Alloys and Compounds*, 721 (2017) 506-511.

[46] B. Huang, C. Zhang, G. Zhang, H. Liao, Wear and corrosion resistant performance of thermal-sprayed Fe-based amorphous coatings: A review, *Surface and Coatings Technology*, 377

(2019).

[47] Méthodes optiques de mesure de vitesse, in, http://olivier.sigwarth.free.fr/TpTs1_fichiers/velocimetrie.pdf, 2012.

[48] T. LIU, Implémentation de méthodes d'intelligence artificielle pour le contrôle du procédé de projection thermique, in, Université de Technologie de Belfort - Montbéliard, 2013.

[49] TECNAR, Accuraspray, https://www.tecnar.com/wp-content/themes/tecnar-oz/pdf/Brochure-Accuraspray-4-0_WEB.pdf, in.

[50] Oseir, SprayWatch, <http://oseir.com/spraywatch-4s/>, in.

[51] W. Swank, J. Fincke, D. Haggard, A particle temperature sensor for monitoring and control of the thermal spray process, in, EG and G Idaho, Inc., Idaho Falls, ID (United States), 1995.

[52] W. Swank, J. Fincke, D. Haggard, C. Berndt, S. Sampath, Thermal Spray Science and Technology, in, ASM International, Materials Park, OH, 1995.

[53] D. Hale, W. Swank, D.J.J.o.t.s.t. Haggard, In-flight particle measurements of twin wire electric arc sprayed aluminum, 7 (1998) 58-63.

[54] T. Renault, M. Vardelle, P. Fauchais, H. Hoffmann, F. Braillard, On-line monitoring (SDC) through coating surface temperature of residual stresses in APS WC-Co17wt% coatings on Hastelloy X, in: Thermal Spray 2001 New Surfaces for a New Millennium: Proceedings of the International Thermal Spray Conference, 2001, pp. 743-750.

[55] L. Qiao, Y. Wu, S. Hong, J. Cheng, Z.J.S. Wei, C. Technology, Influence of the high-velocity oxygen-fuel spray parameters on the porosity and corrosion resistance of iron-based amorphous coatings, 366 (2019) 296-302.

[56] Y. Qin, Y. Wu, J. Zhang, S. Hong, W. Guo, L. Chen, H.J.J.o.M.E. Liu, Performance, Optimization of the HOVF spray parameters by Taguchi method for high corrosion-resistant Fe-based coatings, 24 (2015) 2637-2644.

[57] A.S. Praveen, J. Sarangan, S. Suresh, B.J.C.I. Channabasappa, Optimization and erosion wear response of NiCrSiB/WC-Co HVOF coating using Taguchi method, 42 (2016) 1094-1104.

[58] S. Nourouzi, M.J. Azizpour, H.J.M. Salimijazi, M. Processes, Parametric study of residual stresses in HVOF thermally sprayed WC-12Co coatings, 29 (2014) 1117-1125.

[59] S. Hasan, J.J.J.o.t.s.t. Stokes, Design of experiment analysis of the Sulzer Metco DJ high velocity oxy-fuel coating of hydroxyapatite for orthopedic applications, 20 (2011) 186-194.

[60] K. Balan, S. Manimaran, A.J.J.P.E. Rajan, Prediction Of Interactions Between Various Input Process Parameters Involved In Detonation Gun Coating Technique Through Response Surface Methodology, 97 (2014) 1399-1405.

[61] C. Thiruvikraman, V. Balasubramanian, K.J.J.o.T.S.T. Sridhar, Optimizing HVOF spray parameters to maximize bonding strength of WC-CrC-Ni coatings on AISI 304L stainless steel, 23 (2014) 860-875.

[62] K. Murugan, A. Ragupathy, V. Balasubramanian, K.J.P.M.S. Sridhar, Developing Empirical Relationship to Predict Hardness in WC-10Co-4Cr HVOF Sprayed Coatings, 5 (2014) 918-927.

[63] M. Mahrukh, A. Kumar, S.J.S. Gu, C. Technology, Effects of angular injection, and effervescent atomization on high-velocity suspension flame spray process, 302 (2016) 368-382.

[64] V. Sobolev, J. Guilemany, J.J.J.o.T.S.T. Calero, Prediction of powder particle behavior during high-velocity oxyfuel spraying, 4 (1995) 287-296.

[65] E. Dongmo, R. Gadow, A. Killinger, M.J.J.o.t.s.t. Wenzelburger, Modeling of combustion as well as heat, mass, and momentum transfer during thermal spraying by HVOF and HVFS, 18 (2009) 896.

[66] Machine learning, in, https://en.wikipedia.org/wiki/Machine_learning.

[67] machine learning algorithms, in, https://wordstream-files-prod.s3.amazonaws.com/s3fs-public/styles/simple_image/public/images/machine-learning1.png?SnePeroHk5B9yZaLY7peFkULrfW8Gtaf&itok=yjEJbEKD.

[68] H. Taghavifar, S. Khalilarya, S.J.E. Jafarmadar, Diesel engine spray characteristics prediction with hybridized artificial neural network optimized by genetic algorithm, 71 (2014) 656-664.

[69] C. Einerson, D. Clark, B. Detering, Intelligent control strategies for the plasma spray process, in: Thermal Spray Coat.: Res., Design Appl., Proc. Natl. Spray Conf., 1993, pp. 205-211.

[70] S. Guessasma, G. Montavon, C.J.J.o.T.S.T. Coddet, Neural computation to predict in-flight particle characteristic dependences from processing parameters in the APS process, 13 (2004) 570-585.

[71] S. Guessasma, G. Montavon, P. Gougeon, C. Coddet, Designing expert system using neural computation in view of the control of plasma spray processes, Materials & Design, 24 (2003) 497-502.

[72] S. Guessasma, G. Montavon, C. Coddet, Modeling of the APS plasma spray process using artificial neural networks: basis, requirements and an example, Computational Materials Science, 29 (2004) 315-333.

[73] S. Guessasma, Z. Salhi, G. Montavon, P. Gougeon, C.J.M.S. Coddet, E. B, Artificial intelligence implementation in the APS process diagnostic, 110 (2004) 285-295.

[74] S. Guessasma, C. Coddet, Microstructure of APS alumina–titania coatings analysed using artificial neural network, Acta Materialia, 52 (2004) 5157-5164.

[75] S. Guessasma, G. Montavon, C. Coddet, Plasma spray process modelling using artificial neural networks: Application to Al₂O₃-TiO₂ (13% by weight) ceramic coating structure, in: Journal de Physique IV (Proceedings), EDP sciences, 2004, pp. 363-370.

[76] S. Guessasma, C. Coddet, Neural computation applied to APS spray process: Porosity analysis, Surface and Coatings Technology, 197 (2005) 85-92.

[77] S. Guessasma, F.-I. Trifa, G. Montavon, C.J.M. Coddet, design, Al₂O₃-13% weight TiO₂ deposit profiles as a function of the atmospheric plasma spraying processing parameters, 25 (2004) 307-315.

[78] S. Guessasma, D. Hao, L. Moulla, H. Liao, C. Coddet, Neural Computation to Estimate Heat Flux in an Atmospheric Plasma Spray Process, *Heat Transfer Engineering*, 26 (2005) 65-72.

[79] A.-F. Kanta, G. Montavon, M.-P. Planche, C. Coddet, Artificial Intelligence Computation to Establish Relationships Between APS Process Parameters and Alumina–Titania Coating Properties, *Plasma Chemistry and Plasma Processing*, 28 (2008) 249-262.

[80] A.-F. Kanta, G. Montavon, M. Vardelle, M.-P. Planche, C.C. Berndt, C. Coddet, Artificial Neural Networks vs. Fuzzy Logic: Simple Tools to Predict and Control Complex Processes—Application to Plasma Spray Processes, *Journal of Thermal Spray Technology*, 17 (2008) 365-376.

[81] A.-F. Kanta, G. Montavon, M.-P. Planche, C. Coddet, Artificial neural networks implementation in plasma spray process: Prediction of power parameters and in-flight particle characteristics vs. desired coating structural attributes, *Surface and Coatings Technology*, 203 (2009) 3361-3369.

[82] A.-F. Kanta, G. Montavon, C. Berndt, M.-P. Planche, C.J.E.s.w.a. Coddet, Intelligent system for prediction and control: Application in plasma spray process, 38 (2011) 260-271.

[83] T.A. Choudhury, N. Hosseinzadeh, C.C. Berndt, Artificial Neural Network application for predicting in-flight particle characteristics of an atmospheric plasma spray process, *Surface and Coatings Technology*, 205 (2011) 4886-4895.

[84] T.A. Choudhury, N. Hosseinzadeh, C.C. Berndt, Improving the Generalization Ability of an Artificial Neural Network in Predicting In-Flight Particle Characteristics of an Atmospheric Plasma Spray Process, *Journal of Thermal Spray Technology*, 21 (2012) 935-949.

[85] T. Choudhury, C. Berndt, Z.J.E.A.o.A.I. Man, Modular implementation of artificial neural network in predicting in-flight particle characteristics of an atmospheric plasma spray process, 45 (2015) 57-70.

[86] L. Wang, J.C. Fang, Z.Y. Zhao, H.P. Zeng, Application of backward propagation network for forecasting hardness and porosity of coatings by plasma spraying, *Surface and Coatings Technology*, 201 (2007) 5085-5089.

[87] M.-D. Jean, B.-T. Lin, J.-H. Chou, Application of an Artificial Neural Network for Simulating Robust Plasma-Sprayed Zirconia Coatings, *Journal of the American Ceramic Society*, 91 (2008) 1539-1547.

[88] S. Datta, D.K. Pratihar, P.P. Bandyopadhyay, Modeling of input–output relationships for a plasma spray coating process using soft computing tools, *Applied Soft Computing*, 12 (2012) 3356-3368.

[89] T. Liu, M. Planche, A. Kanta, S. Deng, G. Montavon, K. Deng, Z.J.P.C. Ren, P. Processing, Plasma spray process operating parameters optimization based on artificial intelligence, 33 (2013) 1025-1041.

[90] C.-M. Lin, S.-H. Yen, C.-Y.J.M. Su, Measurement and optimization of atmospheric plasma sprayed CoMoCrSi coatings parameters on Ti-6Al-4V substrates affecting microstructural and

properties using hybrid abductor induction mechanism, 94 (2016) 157-167.

[91] A.H. Pakseresht, E. Ghasali, M. Nejati, K. Shirvanimoghaddam, A.H. Javadi, R.J.T.I.J.o.A.M.T. Teimouri, Development empirical-intelligent relationship between plasma spray parameters and coating performance of Yttria-Stabilized Zirconia, 76 (2015) 1031-1045.

[92] M. Cherigui, S. Guessasma, N. Fenineche, C. Coddet, FeNb magnetic properties correlated to microstructure features, *Materials Science and Engineering: B*, 116 (2005) 40-46.

[93] M. Cherigui, S. Guessasma, N. Fenineche, C. Coddet, Neural computation to correlate HVOF thermal spraying parameters with the magnetic properties of FeNb alloy deposits, *Materials Chemistry and Physics*, 93 (2005) 181-186.

[94] R. Hamzaoui, M. Cherigui, S. Guessasma, O. ElKedim, N. Fenineche, Artificial neural network methodology: Application to predict magnetic properties of nanocrystalline alloys, *Materials Science and Engineering: B*, 163 (2009) 17-21.

[95] G. Zhang, A.-F. Kanta, W.-Y. Li, H. Liao, C.J.M. Coddet, Design, Characterizations of AMT-200 HVOF NiCrAlY coatings, 30 (2009) 622-627.

[96] S. Kamnis, K. Malamousi, A. Marrs, B. Allcock, K. Delibasis, Aeroacoustics and Artificial Neural Network Modeling of Airborne Acoustic Emissions During High Kinetic Energy Thermal Spraying, *Journal of Thermal Spray Technology*, 28 (2019) 946-962.

[97] M.A.R. Mojena, A.S. Roca, R.S. Zamora, M.S. Orozco, H.C. Fals, C.R.C.J.W. Lima, Neural network analysis for erosive wear of hard coatings deposited by thermal spray: Influence of microstructure and mechanical properties, 376 (2017) 557-565.

[98] S. Agatonovic-Kustrin, R. Beresford, Basic concepts of artificial neural network (ANN) modeling and its application in pharmaceutical research, *Journal of Pharmaceutical and Biomedical Analysis*, 22 (2000) 717-727.

[99] W.S. McCulloch, W. Pitts, A logical calculus of the ideas immanent in nervous activity, *The bulletin of mathematical biophysics*, 5 (1943) 115-133.

[100] D. Hebb, *Organization of behavior*. New York: Wiley, (1949).

[101] B. Farley, W.J.T.o.t.I.P.G.o.I.T. Clark, Simulation of self-organizing systems by digital computer, 4 (1954) 76-84.

[102] N. Rochester, J. Holland, L. Haibt, W.J.I.T.o.i.T. Duda, Tests on a cell assembly theory of the action of the brain, using a large digital computer, 2 (1956) 80-93.

[103] F. Rosenblatt, *The perceptron, a perceiving and recognizing automaton Project Para*, Cornell Aeronautical Laboratory, 1957.

[104] B.J.Y. Widrow, MC, Jacobi, GT., G.e. Goldstein, Generalization and Information Storage in Networks of ADALINE Neurons. *Self Organizing Systems*, (1962) 435-461.

[105] T. Bouwmans, S. Javed, M. Sultana, S.K. Jung, Deep neural network concepts for background subtraction: A systematic review and comparative evaluation, *Neural Netw*, 117 (2019) 8-66.

- [106] P.J. Werbos, *Beyond Regression: New Tools for Prediction and Analysis in the Behavioral Sciences*, Harvard University, 1975.
- [107] C. Cortes, V.J.M.I. Vapnik, *Support-vector networks*, 20 (1995) 273-297.
- [108] G.E. Hinton, S. Osindero, Y.-W.J.N.c. Teh, *A fast learning algorithm for deep belief nets*, 18 (2006) 1527-1554.
- [109] W. Liu, Z. Wang, X. Liu, N. Zeng, Y. Liu, F.E.J.N. Alsaadi, *A survey of deep neural network architectures and their applications*, 234 (2017) 11-26.
- [110] K.L. Priddy, P.E. Keller, *Artificial Neural Networks: An Introduction*, 2005.
- [111] E.s.P.L. Vu-Quoc), <https://commons.wikimedia.org/wiki/File:Neuron3.png>, in, 2018.
- [112] M.H. Beale, M.T. Hagan, H.B.J.U.s.G. Demuth, *MathWorks, Neural network toolbox*, 2 (2010) 77-81.
- [113] J.J.N.n. Schmidhuber, *Deep learning in neural networks: An overview*, 61 (2015) 85-117.
- [114] A. Poznyak, I. Chairez, T. Poznyak, *A survey on artificial neural networks application for identification and control in environmental engineering: Biological and chemical systems with uncertain models*, *Annual Reviews in Control*, (2019).
- [115] M. Puri, A. Solanki, T. Padawer, S.M. Tipparaju, W.A. Moreno, Y. Pathak, *Introduction to Artificial Neural Network (ANN) as a Predictive Tool for Drug Design, Discovery, Delivery, and Disposition*, in: *Artificial Neural Network for Drug Design, Delivery and Disposition*, 2016, pp. 3-13.
- [116] H.B. Demuth, M.H. Beale, O. De Jess, M.T. Hagan, *Neural network design*, Martin Hagan, 2014.
- [117] G.W. Dombi, P. Nandi, J.M. Saxe, A.M. Ledgerwood, C.E.J.J.o.T. Lucas, A.C. Surgery, *Prediction of rib fracture injury outcome by an artificial neural network*, 39 (1995) 915-921.
- [118] J.L. Jiang, X. Su, H. Zhang, X.H. Zhang, Y.J.J.C.b. Yuan, d. design, *A novel approach to active compounds identification based on support vector regression model and mean impact value*, 81 (2013) 650-657.
- [119] J.-L. Jiang, Z.-D. Li, H. Zhang, Y. Li, X.-H. Zhang, Y.-f. Yuan, Y.-j.J.P.m. Yuan, *Feature selection for the identification of antitumor compounds in the alcohol total extracts of Curcuma longa*, 80 (2014) 1036-1044.
- [120] X. Jiang, J. Hu, M. Jia, Y.J.E. Zheng, *Parameter matching and instantaneous power allocation for the hybrid energy storage system of pure electric vehicles*, 11 (2018) 1933.
- [121] G. Xu, P. Schwarz, H.J.E.p. Yang, *Determining China's CO2 emissions peak with a dynamic nonlinear artificial neural network approach and scenario analysis*, 128 (2019) 752-762.

Chapter 2. Spray equipment, coating characterization, and performance test

Introduction

As discussed in [Chapter 1](#), this present work thoroughly investigates the HVOF spray process by applying ANN models. Therefore, a series of physical experiments and characterizations need to be carried out in order to obtain data to implement ANN models. This section presents all relevant experimental equipment and characterized methods. First, a homemade HVOF control system is briefly introduced, which controls and records the HVOF process, and also integrates ANN models. Then, the details for elaborating HVOF sprayed coatings are given, including the setup of the HVOF spray, the selection of powders, and the preparation of substrates. In addition, the characterizations of in-flight particles and coatings' performances are displayed separately. The environment for implementing ANN models is also been briefly introduced. Finally, a conclusion is given.

2.1. Coatings elaborating via HVOF spray

2.1.1. Setup of the HVOF spray process

In order to control and record the HVOF process, a recompiled control system has been developed for the HVOF thermal spray process. This control system was programmed using the Programmable Logic Controller (PLC, B&R Industrial Automation GmbH, Eggelsberg, Austria), as shown in [Figure 2.1](#). Both systems for controlling the CDS torch and Diamond-Jet 2701/2702 torch were developed and integrated into the same controller. Details about how the intelligent HVOF spray control system was constructed will be presented in [Chapter 5](#). In addition to controlling the spray process, this also provides the interface that relates the relationships among the HVOF spray process parameters, behaviors of the in-flight particles, and coating properties.

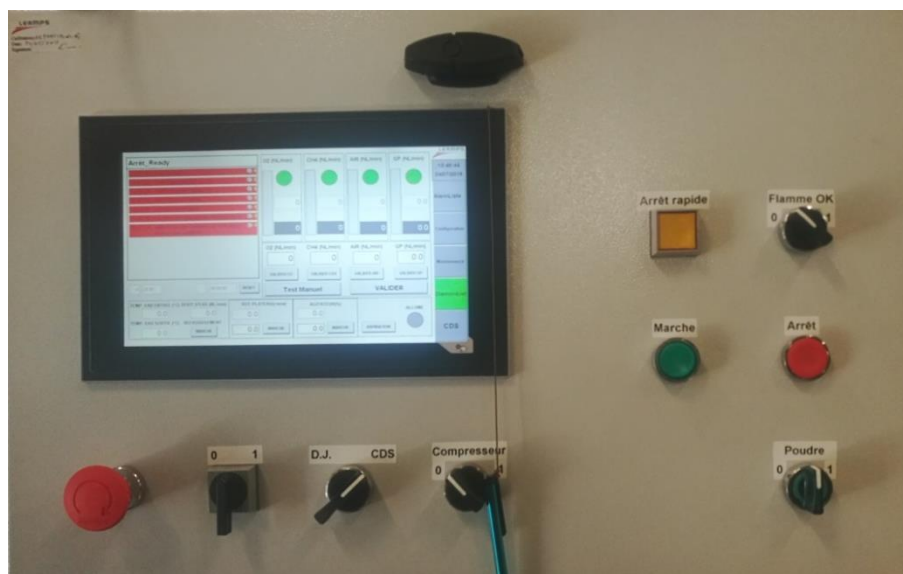


Figure 2.1 Interface of the HVOF spray control system

The recompiled control system enables the HVOF spray experiments to be carried out. The HVOF spray experiment was conducted using the experimental setup that is shown in [Figure 2.2](#). The HVOF spray system consists of the commercial DJ-2701 hybrid gun (Sulzer-Metco, Westbury, NY) and the homemade recompiled control system as previously mentioned. Methane (CH_4) was employed as the fuel gas to produce the flame, using as the heat source for the HVOF spray process. The hybrid gun was carried by a six-axis industrial robot (IRB2600-20 ABB, Switzerland), to control the moving trajectory and velocity of the depositing coatings, while also horizontally and vertically scanning the substrate surface. Multiple scans were adopted to produce suitable coatings. The feedstock was fed by the powder feeder. Characterizations of the in-flight particles were detected by the Accuraspray-g3 system.

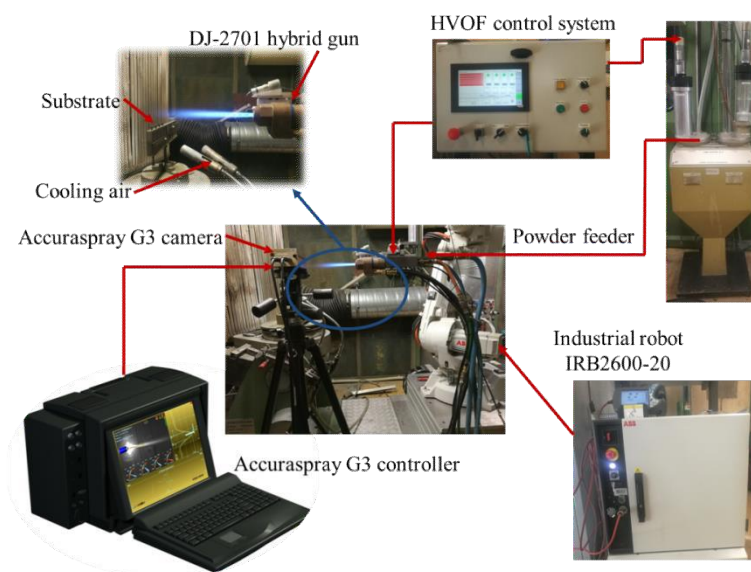


Figure 2.2 Schematic diagram of the experimental setup

2.1.2. Selection and treatment of powder

The commercial $\text{Cr}_3\text{C}_2\text{-}25(\text{Ni}20\text{Cr})$ powder (METCO 81 VF-NS: Oerlikon Metco AG, Wohlen, Switzerland), with particle size ranges $-45+5 \mu\text{m}$, were used as feedstock powders in this study. These chromium carbide materials are blends of chromium carbide and nickel-chromium powders, the density of which is 7.04 g/cm^3 . The nickel-chromium alloy, with melting point of 1374 to 1420°C , serves as a matrix that improves overall coating integrity and corrosion resistance, while the chromium carbide constituent, with melting point of 1890°C , serves as a hard phase that assures wear resistance. The chemical composition of feedstock is given in Table 2.1 [1].

Table 2.1 Chemical composition of the feedstock powder

Product	Nominal chemistry	Weight percent (nominal)			
		Cr	Ni	C	Other (max)
Metco 81VF-NS	$\text{Cr}_3\text{C}_2\text{-}25(\text{Ni}20\text{Cr})$	Balance	18.75	9.75	2.25

The feedstock's morphology was captured by a scanning electron microscope (SEM, JSM-5800LV, JEOL) with a secondary electronic mode, which is presented in Figure 2.3 (a). This also shows that the feedstock contains a mixture of fine and coarse particles. The size distribution was measured by a laser diffraction particle size measuring instrument (Mastersizer 2000, Malvern Instruments Ltd). This is presented in Figure 2.3 (b), which indicates that the particle size featured is $D_{10} = 5 \mu\text{m}$, $D_{50} = 22.6 \mu\text{m}$, and $D_{90} = 45 \mu\text{m}$.

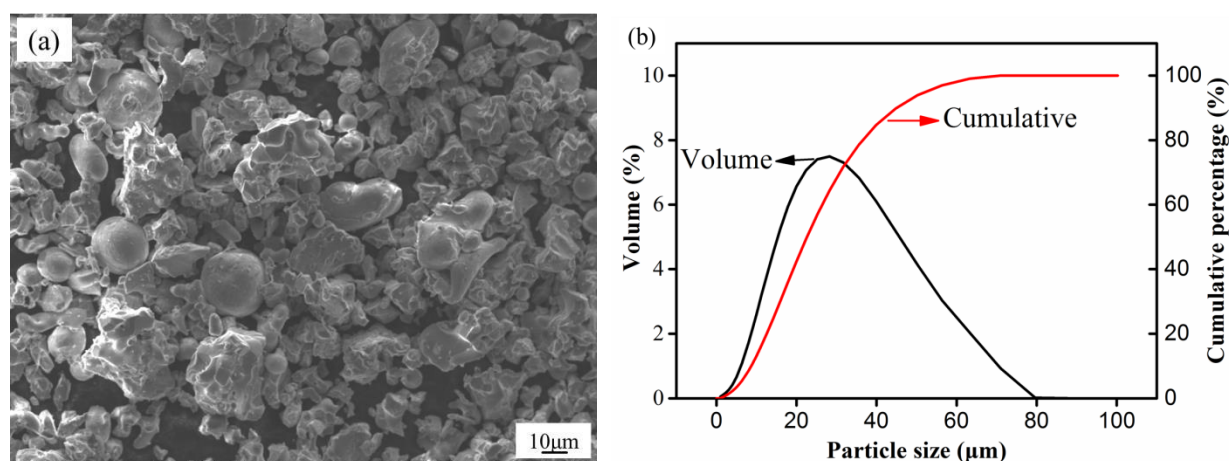


Figure 2.3 The feedstock's morphology (a) and diameter distribution (b)

2.1.3. Selection and treatment of substrate

Coatings were sprayed on 316L stainless steel substrates (Ø25 mm×10 mm), which originated from a cylinder bar (Ø25 mm×3000m) that had undergone cutting and turning procedures. The substrates had been grit-blasted and then ultrasonically cleaned in ethanol for ten minutes, before spraying. The roughness of the substrate's surface was about $Ra = 5.0\mu\text{m}$.

2.2. Characterization of in-flight particles

During the HVOF spray process, the behaviors of in-flight particles were observed and recorded. A commercial diagnostic system, Accuraspray-g3 (Tecnar, St-Bruno, PQ, Canada), was employed to capture the average velocity and temperature of the in-flight particles. The sensor was oriented perpendicularly to the spray stream and placed at a laterally distance of 20cm from the spray stream, and with an axial distance of stand-off distance from the torch outlet, as shown in Figure 2.4. The particle surface temperature measurement is based on the twin wavelength pyrometer principle. The particle flying velocity was detected by a dual fiber optical device.

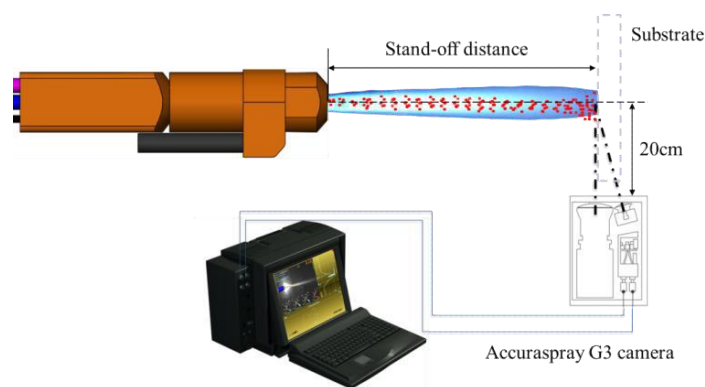


Figure 2.4 Installation of Accuraspray-g3 sensor

2.3. Characterization of coatings

After the HVOF spray process, the coatings were treated and their properties were characterized. From the perspective of this work's materials science and research requirements, the morphologies, phase compositions, microhardness, and wear resistance were observed and measured.

2.3.1. Preparation of samples

Both the coatings' surface and cross section need to be characterized for subsequent performance characterization. The samples were prepared with the sequential grinding procedure, with P220 SiC paper and MD-Largo disc, and were then polished with 3 μm diamond suspensions and 0.04 μm non-drying colloidal silica suspensions. This pre-treatment was applied to all the samples, in order to test porosity, microhardness, and wear test.

2.3.2. Observation of the morphologies of coatings

In order to calculate the porosity of coatings, the cross-sectional microstructure of prepared coatings was examined by the SEM with a secondary electronic mode. More than 15 consecutive pictures were captured and an average value was calculated using imaging software (Image J).

2.3.3. Determination of the phase compositions

The phase compositions of the films were determined by X-ray diffraction (XRD, Bruker AXS D8 focus, Germany) with a cobalt anticathode ($\lambda = 1.78897 \text{ \AA}$) at 35 kV, 40 mA. The fast-scanning speed of 0.1o/s was used to determine the phase composition, to calculate the relative intensities of the different

diffraction peaks, and to evaluate the crystal size.

2.3.4. Measurement of the microhardness

The microhardness of the coatings was measured on the coating's cross-section by a Vickers microhardness indenter (Leiz-Wetzlar, Germany), with a load of 300 gf (i.e., 2.94 N) and a dwelling time of 25 s. Twenty indentations were randomly measured, which subsequently gave an average microhardness value for each coating..

2.3.5. Abrasive test of coatings

Dry sliding wear tests were carried out in a CSEM tribometer (Switzerland), which had a ball-on-disc configuration, as shown in Figure 2.5 (a). The tests were performed in an atmospheric environment with a temperature of 15-20°C and humidity of 40–50%. An Al₂O₃ ball (6 mm diameter) was employed as the counterpart material and was cleaned with alcohol before the test. This was fixed on the stationary shaft, while the sample was mounted on the rotating shaft. The test was then conducted at the same sliding condition with a normal load (F_N) of 5 N, a rotation radius (R) of 7 mm, a linear rotation speed (v) of 10 mm/s, and a sliding distance (S) of 500 m, as displayed in Figure 2.5 (b). An example of the sample mounted on the fixture is shown in Figure 2.5 (c).

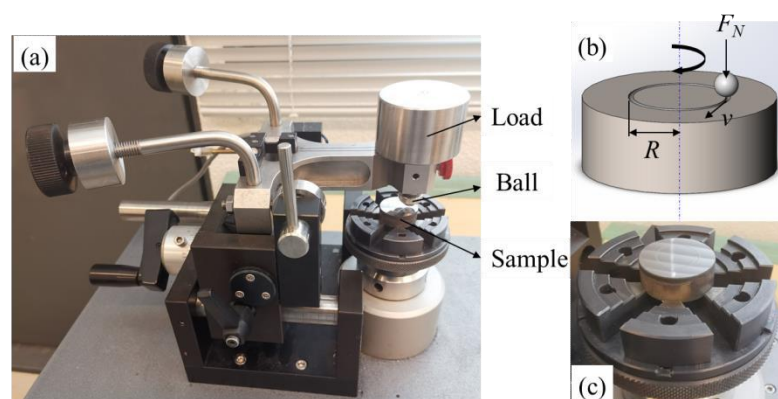


Figure 2.5 Equipment setup of ball-on-disc CSEM Tribometer (a), schematic diagram (b), and physical sample (c)

The cross-sectional profiles of the worn track were measured using a profilometer (Altisurf 500, France). At least ten profiles were conducted, in order to obtain an average wear volume. Then, the wear rate of the samples, which indicates the amount of material removed from the surface, was used

to evaluate the wear resistance of the coatings. This is expressed by:

$$K = \frac{\Delta V}{SF_N} \quad \text{Eq. (2.1)}$$

, where ΔV is the volume loss of the material [mm^3], S is the sliding distance [m], and F_N is the applied normal load [N].

2.4. Environment for implementing ANN models

In this work, MATLAB software was chosen to design, train, and test the ANN models. MATLAB is an advanced technical computing language and interactive environment, which can be used for algorithm development, data visualization, data analysis, and numerical computing. In addition to common functions, such as matrix operations and drawing functions/data images, MATLAB can also be used to create user interfaces and programs that are written in other languages (including C, C++, Java, Python, and FORTRAN). The ANN models were implemented with the Neural Network Toolbox in MATLAB. Finally, the trained ANN models were integrated into the recompiled HVOF control system.

2.5. Conclusions

This chapter has presented the deposition method (HVOF) that was used in this study, as well as the corresponding setups and feedstock. The characterization methods and performance tests of the coatings have also been outlined, which incorporates the different experimental aspects of this thesis. The environment for designing the ANN models was also briefly described. All these pieces of physical and virtual equipment provide the foundation for further experiments and analysis, which are presented in the following sections.

Reference of chapter 2

- [1] Oerlikon, Nickel Chromium Powder Blends <https://www.oerlikon.com>, in, 2017.

Chapter 3. Experimental procedure and analysis of the results

Introduction

The instruments that were introduced in [Chapter 2](#) enable the implementation of the HVOF spray experiments, the characterizations of in-flight particles, and tests of coating properties. Consequently, this chapter explains how the process parameters were selected and then the experimental results will be displayed. The behaviors of in-flight particles and the coating performances will be discussed, in order to obtain a preliminary understanding of the correlation among the process parameters, behaviors of in-flight particles, and coating properties. A brief conclusion will subsequently be given.

3.1. Selection of HVOF process parameters and experimental procedure

3.1.1. HVOF spray process parameters

HVOF spray process parameters are known to significantly influence the velocity and temperature of in-flight particles and, thus, coating performances. A large number of variables are involved in the process, including spray process parameters (e.g., oxygen flow rates, fuel and air flow rate, and powders' feed rate), robot operating parameters (e.g., stand-off distance, spraying angle, and scanning step), feedstock powders properties (e.g., particle size and particle size distribution), and hardware characteristics (e.g., nozzle geometry). Some of these variables are shown in [Figure 3.1](#).

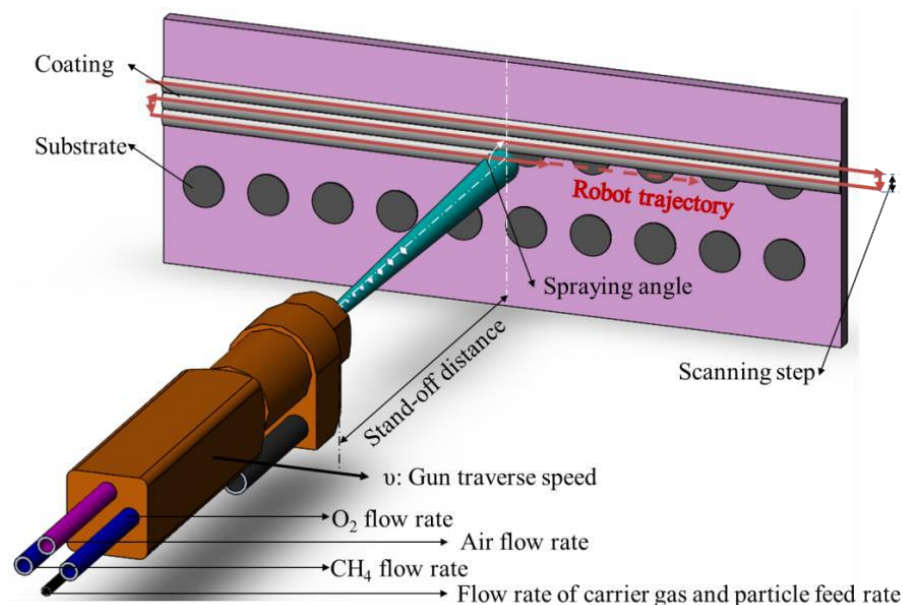


Figure 3.1 Some of the variables involved in the HVOF spray process

Since the feedstock powders' properties and the hardware characteristics are unchangeable in this study and the robot operating parameters (except stand-off distance) mostly affect the surface topography and deposition rate of coatings [1-3], attention is mainly concentrated on the influence of the process parameters and stand-off distance. This illustrates that the powder feed rate and stand-off distance are the main factors that affect particle temperature, and, for the particle speed, these are the stand-off distance and oxygen flow rate in the HVOF process [4]. The important sequences of the spray parameters on the performance of coatings can also be concluded, which are as follows: fuel flow rate > spray distance > powder feed rate > oxygen flow rate for hardness, spray distance > fuel flow rate > powder feed rate > oxygen flow rate for porosity, oxygen flow rate > fuel flow rate > powder feed rate > spray distance for fracture toughness [5]. However, another study asserts a different importance sequence of the spray parameters for the HVOF spray, which is: stand-off distance > powder feed rate > fuel flow rate > oxygen flow rate [6]. Although the powder feed rate has an obvious effect on the properties of the coatings in these pieces of research [5-7], this will not be considered, due to economic reasons. To summarize, only focusing on the most influential parameters, the experiments were conducted by varying three process parameters: namely, O₂ flow rate, fuel (CH₄) flow rate, and stand-off distance.

According to existing knowledge and analysis of the parameters outlined above, the full DOE was not conducted in this work, in order to save both costs and time. As previously discussed, only the most important parameters were considered and used to build the experiment setup. With these selected process parameters, the experimental procedure and its results are outlined in the following sections.

3.1.2. Experimental procedure

After selecting the most influential parameters, the HVOF spray experiments were conducted according to the parameters that are listed in [Table 3.1](#). Considering the capacity of the gas that was supplied in the HVOF spray system, the O₂ flow rate (i.e., Q(O₂)) varies from 200 to 240 slpm, and the fuel (CH₄) flow rate (i.e. Q(CH₄),) varies from 120 to 200 slpm. Existing literature asserts that the stand-off distance (SOD) of the HVOF spray varies from 160 to 400 mm [8-12], wherein the stand-off distance of 200 to 350 mm is most frequently employed. Considering the literature's conclusions and

the performance of the torch used, in this work the SOD was set from 200 to 320 mm, with an increment of 40 mm. The air flow rate was set as 300 slpm, which is the highest value supplied by the spray system under a steady state. The flow rate of the carrier gas was 40slpm, which resulted in a continuous supply of powder. Other optimized values were set as 400 mm/s for the gun traverse speed, 6 mm for the scanning step, and 30 g/min for the powder feed rate.

Table 3.1 HVOF spray process parameters

Parameters	Levels				
CH ₄ flow rate (slpm)	120	140	160	180	200
O ₂ flow rate (slpm)	200	240			
Stand-off distance(mm)	200	240	280	320	
Air flow rate(slpm)	300				
Flow rate of carrier gas(slpm)	40				
Gun traverse speed(mm/s)	400				
Scanning step (mm)	6				
Powder feed rate(g/min)	30				

With the selected parameters and parameter values, 40 sets of experiments were conducted to investigate their interrelationships and combined impacts on the behavior of in-flight particles and coating properties. The experiment was designed as outlined in Table 3.2. However, due to the low capacity of the gas supplied in the HVOF system, some of the nominal values of the gas flow rates were not achieved, as marked in red in Table 3.2. Analysis of the behaviors of in-flight particles and coating properties will be presented and discussed in Sections 3.2 and 3.3.

Table 3.2 Experimental design of the HVOF spray process

No.	Parameters			No.	Parameters		
	SOD/mm	Q(O ₂)/slpm	Q(CH ₄)/slpm		SOD/mm	Q(O ₂)/slpm	Q(CH ₄)/slpm
1	200	200	120	21	280	200	120
2	200	200	140	22	280	200	140
3	200	200	160	23	280	200	160
4	200	200	180	24	280	200	180

5	200	200	200	25	280	200	200
6	200	240	120	26	280	240	120
7	200	240	140	27	280	240	140
8	200	240	160	28	280	240	160
9	200	240	180	29	280	230	180
10	200	240	186	30	280	225	200
11	240	200	120	31	320	200	120
12	240	200	140	32	320	200	140
13	240	200	160	33	320	200	160
14	240	200	180	34	320	200	180
15	240	200	200	35	320	200	200
16	240	240	120	36	320	240	120
17	240	240	140	37	320	240	140
18	240	240	160	38	320	240	160
19	240	240	180	39	320	233	180
20	240	240	188	40	320	230	200

, where SOD stands for stand-off distance, $Q(O_2)$ for O_2 flow rate, and $Q(CH_4)$ for CH_4 flow rate.

3.2. Analysis of the behaviors of in-flight particles

The temperature and velocity of in-flight particles were detected and recorded by Accuraspray-g3. Forty sets of experimental results were tabulated, as presented in Table 3.3. The values were organized according to the order shown in Table 3.2. From this, it can be summarized that the velocity of in-flight particles varies from 254 m/s to 531 m/s, with an average of 373 m/s. In addition, the temperature of in-flight particles varies from 2064 K to 2460 K, with an average of 2284K. The maximums of the standard deviation for velocity and temperature were 5.0 m/s and 9.0 K, respectively, which indicates that the Accuraspray-g3 is a reliable means of carrying out these measurements. A detailed analysis of the behaviors of in-flight particles is presented in the following section.

Table 3.3 The temperature and velocity of in-flight particles

No.	Behaviors of in-flight particles		No.	Behaviors of in-flight particles	
	v /[m/s]	T /K		v /[m/s]	T /K
1	467±1.9	2223±2.4	21	292±3	2455±4
2	476±0.3	2186±2.1	22	298±5	2432±7.5
3	468±0.1	2139±1.8	23	300±1	2390±4.5
4	461±0.8	2099±2.3	24	314±2.7	2400±4.4
5	455±0.4	2064±3.1	25	297±0.6	2354±1.5
6	508±0.3	2239±1.4	26	301±1	2457±5
7	509±0.7	2204±1.8	27	312±1.8	2460±3.4
8	531±1.1	2170±2.3	28	328±1.3	2453±3.4
9	518±0.9	2120±1.7	29	317±0.7	2433±5
10	515±0.4	2096±0.6	30	306±1.1	2406±9
11	389±3.2	2234±1.6	31	269±2	2395±5
12	409±0.6	2201±1.4	32	270±1	2388±5
13	404±1.5	2151±2	33	265±2	2350±4
14	400±0.2	2127±1.7	34	263±1.5	2341±2.5
15	399±0.8	2097±3.4	35	254±4.5	2269±2.5
16	423±0.2	2256±1.5	36	274±1	2405±2.5
17	450±0.1	2233±1.6	37	281±1.5	2432±4
18	462±1.9	2204±1.2	38	278±0.5	2423±2
19	463±1.2	2167±1.4	39	273±1.5	2406±4
20	468±0.4	2145±4.1	40	269±1	2368±5

, where v and T stand for the velocity and temperature of in-flight particles, respectively.

3.2.1. Temperature of the in-flight particles

The experimental results of the temperature of in-flight particles are shown in [Figure 3.2](#). From this, it can be concluded that, along with the increase of $Q(\text{CH}_4)$, temperature exhibits an overall tendency of decline, particularly for the smaller SOD. When the SOD is 200 mm, the temperature continuously decreases from 2223 to 2064 K (7.15% variation), and from 2239 to 2096 K (6.38%

variation) for the $Q(O_2)$ of 200 and 240 slpm. When the SOD increases to 240 mm, the temperature continuously decreases from 2234 to 2097 K (6.13% variation), and from 2256 to 2145 K (4.92% variation) for the $Q(O_2)$ of 200 and 240 slpm. However, different tendencies occur for the longer SOD. For the $Q(O_2)$ of 200 slpm, with increasing $Q(CH_4)$, the temperature continuously decreases from 2455 to 2354 K (4.11% variation), and from 2395 to 2269 K (5.26% variation) for SOD of 280 mm and 320 mm, respectively. However, for the $Q(O_2)$ of 240 slpm, with the increase of $Q(CH_4)$, the temperature increases and reaches the maximum value at $Q(CH_4)$ of 140 slpm, after which it decreases with variation of 2.22% and 2.70% for SOD of 280 mm and 320 mm, respectively.

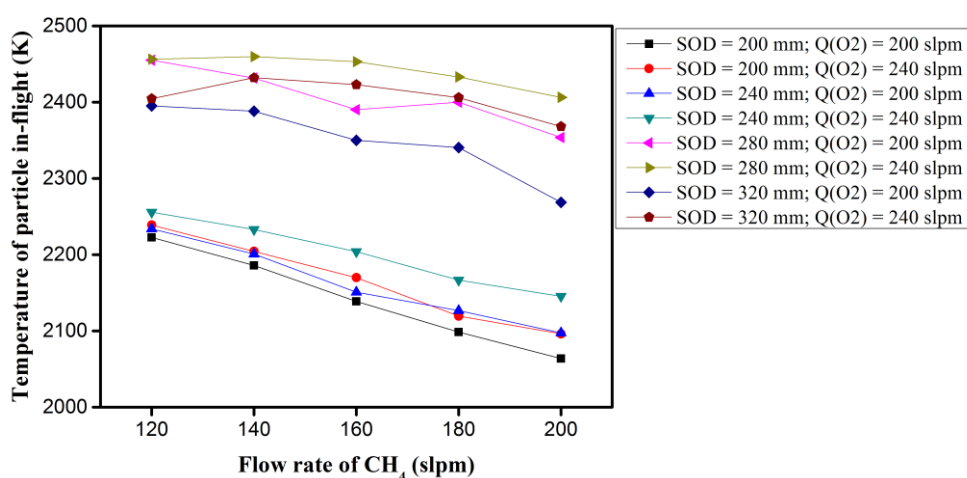


Figure 3.2 The experimental results of the temperature of in-flight particles for SOD from 200 to 320 mm, $Q(O_2)$ from 200 to 240 slpm, and $Q(CH_4)$ from 120 to 200 slpm

To better understand the influence of gas flow rate, the experimental results of the temperature of in-flight particles, with respect to different $Q(O_2)$ and $Q(CH_4)$, were rescheduled, as shown in Figures 3.3 and 3.4. Figure 3.3 indicates that, for the same SOD and $Q(CH_4)$, the red points are always higher than the black points. This suggests that the temperature exhibits a tendency to grow, as the $Q(O_2)$ increases. The impact of the $Q(O_2)$ on the behaviors of in-flight particles is complex [14]. In one respect, increasing $Q(O_2)$ contributes to the increased temperature of in-flight particles, due to the increased reaction rate of the gases. Conversely, the increasing $Q(O_2)$ increases the velocity of in-flight particles and enhances their cooling effect, which results in the decreased temperature of in-flight particles. From this perspective, it can be deduced that the influence of the reaction rate of the gases on the in-flight particles is greater than the cooling effect during the HVOF process.

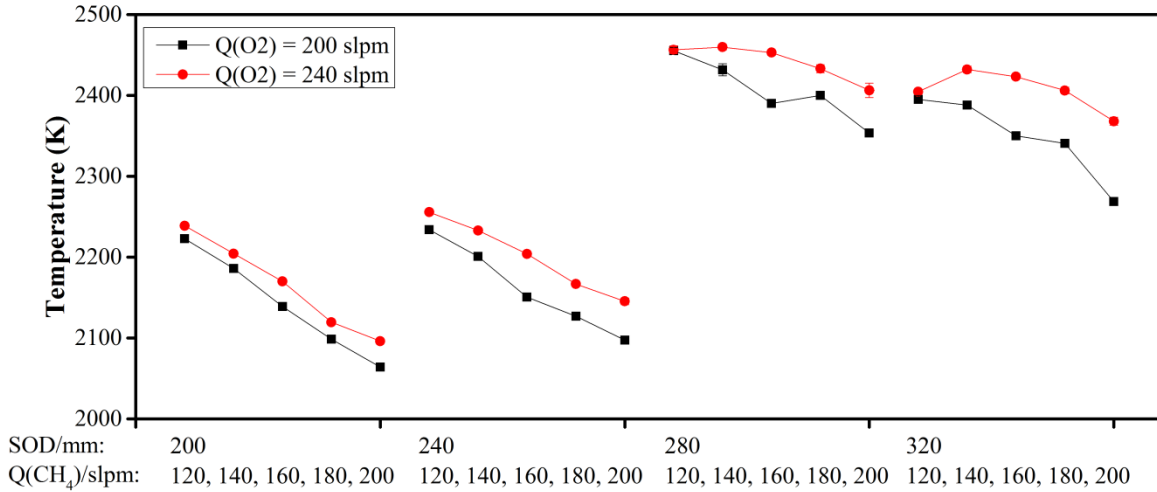


Figure 3.3 Comparison of the temperature of the in-flight particles, for different O₂ flow rates

An opposing result can be obtained for Q(CH₄), as indicated in Figure 3.4. Here, the temperature generally decreases as Q(CH₄) increases, except for some fluctuations with a longer SOD.

Different tendencies occur for the SOD of 280 and 320 mm, which can be explained considering the influence of the combustion reaction. The stoichiometric reaction for methane, $\text{CH}_4 + 2\text{O}_2 \rightarrow 2\text{H}_2\text{O} + \text{CO}_2$, gives a stoichiometric ratio $(Q_{\text{O}_2}/Q_{\text{CH}_4})_{st}$ of 0.5. The fuel-to-oxygen equivalence ratio (Φ), defined as $\Phi = (Q_{\text{O}_2}/Q_{\text{CH}_4}) / (Q_{\text{O}_2}/Q_{\text{CH}_4})_{st}$, gives the flame temperature profile, with maximum values of temperature reached for Φ close to 1.1 [13]. Compared to other sets of process parameters, Φ is 1.2 and 1.16 for Q(O₂)/Q(CH₄) flows of 200/120 slpm and 240/140 slpm, which are closest to $\Phi \sim 1.1$, resulting in a more complete combustion and thus maximum temperature, which explains the different tendencies for different Q(O₂).

However, Φ has no significant effect on the temperature of in-flight particles for SOD of 200 and 240 mm, as indicated by the continuous downtrend in their temperature. This suggests that the influence of fuel-to-oxygen ratio is more obvious with longer SOD.

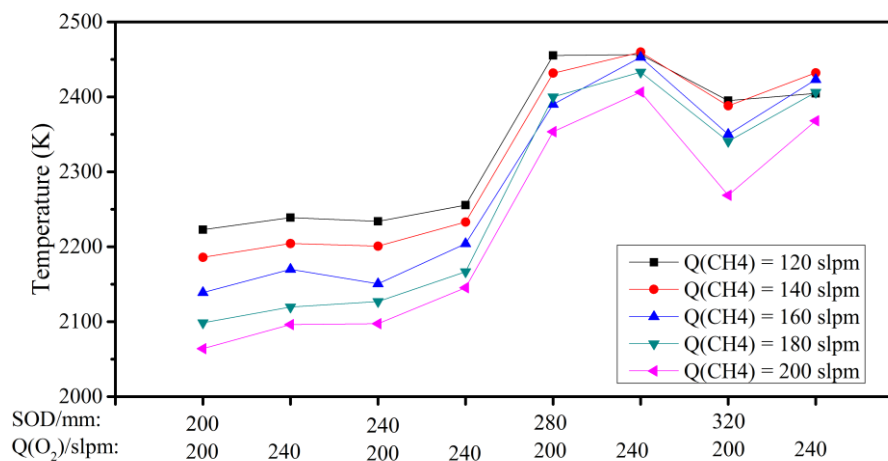


Figure 3.4 Comparison of the temperature of the in-flight particles for different CH₄ flow rates

In order to comprehend the influence of SOD, the experimental results of the temperature of in-flight particles were also rescheduled, as displayed in Figure 3.5. This illustrates that, with the increase of the SOD, the temperature increases for the SOD from 200 to 280 mm and then decreases for the SOD from 280 to 320 mm, with a nonlinear rate. Taking the condition of $Q(O_2)$ of 200 slpm and $Q(CH_4)$ of 120 slpm as an example, the temperature of in-flight particles increases from 2223 K (SOD of 200 mm) to 2234 K (SOD of 240 mm), then to 2455 K (SOD of 280 mm), and finally decreases to 2395 (SOD of 320 mm), responding to the increasing rate of 0.49%, 9.89%, and -2.44%. Variations in the temperature of in-flight particles, which is caused by the SOD, are explained in the following paragraph.

The dwell time of the particles in the flame greatly impacts the temperature of in-flight particles. With increasing SOD, the dwell time of the in-flight particles also increases, resulting in the increased temperature of the in-flight particles, as the high temperature of the flame continuously exchanges energy with the in-flight particles. Simultaneously, there is also a continuous energy exchange between the flame and its surroundings during flight, which results in the decreased temperature of the flame and, subsequently, of the in-flight particles [15]. Furthermore, with longer SOD, the in-flight particles may fly out of the flame before depositing on the substrate, which also leads to a decrease in the temperature of the in-flight particles. The variation of the temperature of the in-flight particles can contribute to the coupling effect of the energy exchanges.

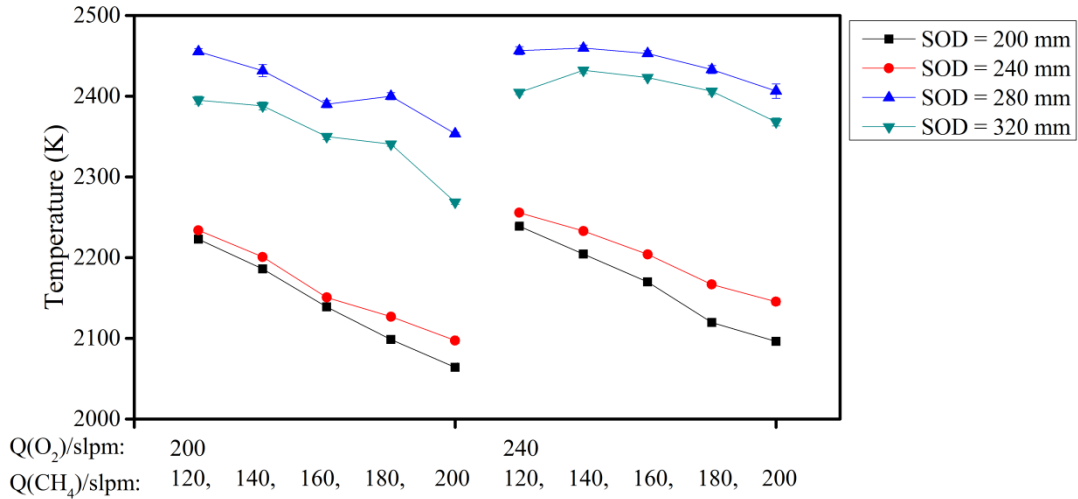


Figure 3.5 Comparison of the temperature of the in-flight particles for different SOD

3.2.2. Velocity of the in-flight particles

Similar analysis can be conducted for the velocity of in-flight particles. The experimental values of velocity of the in-flight particles are presented in Figure 3.6. Generally speaking, the velocities of the in-flight particles primarily increase and then decrease when the $Q(\text{CH}_4)$ increases. However, the process parameters that correspond to the maximums of the velocity are different. For the $Q(\text{O}_2)$ of 200 slpm, the velocity reaches the maximum values of 476 m/s, 409 m/s, and 270 m/s for the SOD of 200 mm, 240 mm, and 320 mm, respectively, when the $Q(\text{CH}_4)$ is 140 slpm. Meanwhile, for SOD of 280 mm, the velocity reaches the maximum (314) when $Q(\text{CH}_4)$ is 180 slpm. The differences between the extreme values of velocity are 4.56%, 5.34%, 7.64%, and 6.30% for the SOD in ascending order. For the $Q(\text{O}_2)$ of 240 slpm, the velocity reaches the maximum values of 531 m/s, 468 m/s, 328 m/s, and 281 m/s for the $Q(\text{CH}_4)$ of 160 slpm, 200 slpm, 160 slpm, and 140 slpm, respectively, with the increase of SOD. The differences between the extreme values of velocity are 4.52%, 10.60%, 8.95%, and 4.46%, with increasing SOD.

The mounting velocity mainly contributes to the increase of the total gas flow rate, which provides more momentum to the in-flight particles. This can be further verified by the tendency of the velocity to increase as $Q(\text{O}_2)$ increases. Nevertheless, the decrease of the velocity differs substantially from the findings of previous research studies [16].

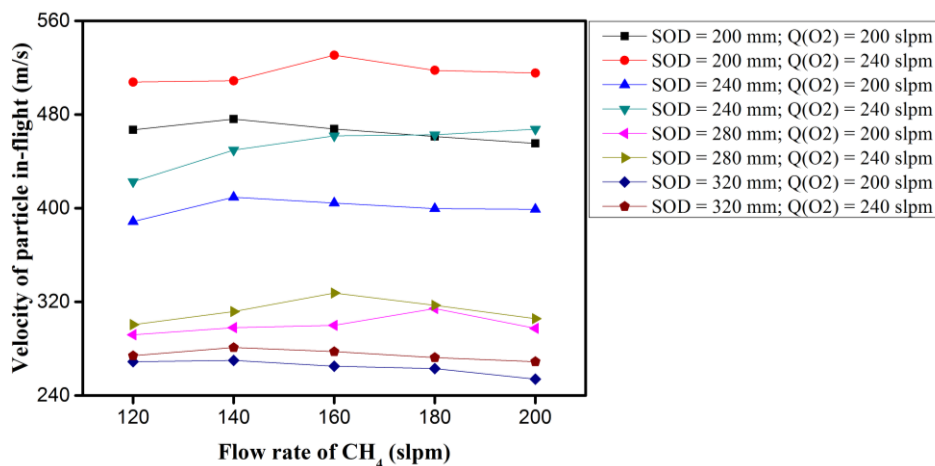


Figure 3.6 The experimental results of velocity of the in-flight particles for SOD from 200 to 320 mm, O₂ flow rate from 200 to 240 slpm, and CH₄ flow rate from 120 to 200 slpm

Figure 3.7 presents the comparison results for different Q(O₂), which clearly indicate that, for the same SOD and Q(CH₄), the red points are always higher than the black points. This demonstrates the tendency of the velocity to increase as Q(O₂) increases. The increase of Q(O₂) increases the velocity of in-flight particles, which contributes to the increase of the total gas flow rate and which, in turn, provides more momentum to the in-flight particles. Figure 3.7 also illustrates that the difference between the Q(O₂) of 200 slpm and 240 slpm for SOD of 200 mm and 240 mm is much higher than that for SOD of 280 mm and 320 mm. The maximum differences between the velocity for different Q(O₂) are 63m/s, 68m/s, 27 m/s, and 12m/s, with increasing SOD. From this, it can be deduced that, with the increase of SOD, the effect of the Q(O₂) on the velocity of in-flight particles fades out. Unfortunately, there is not an obvious tendency that can be summarized to study the impact of Q(CH₄), as illustrated in Figure 3.8.

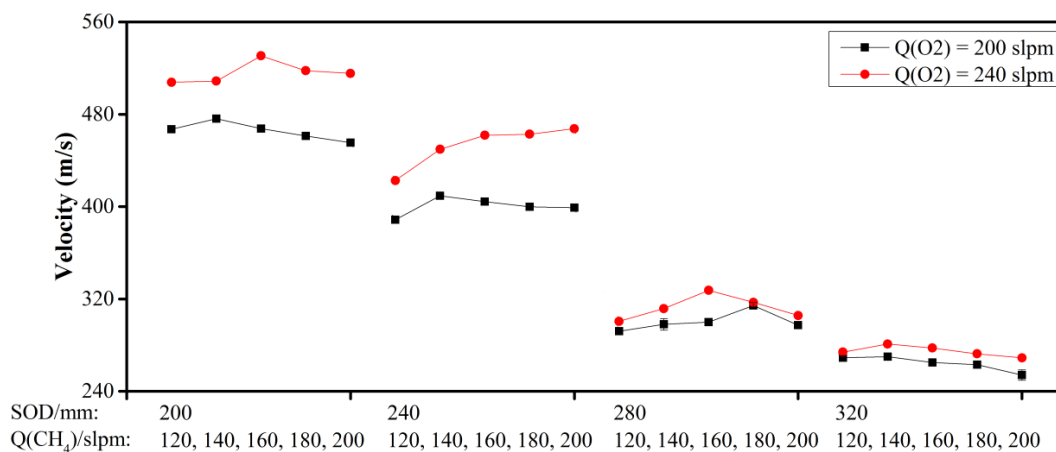


Figure 3.7 Comparison of the velocity of the in-flight particles for different O₂ flow rates

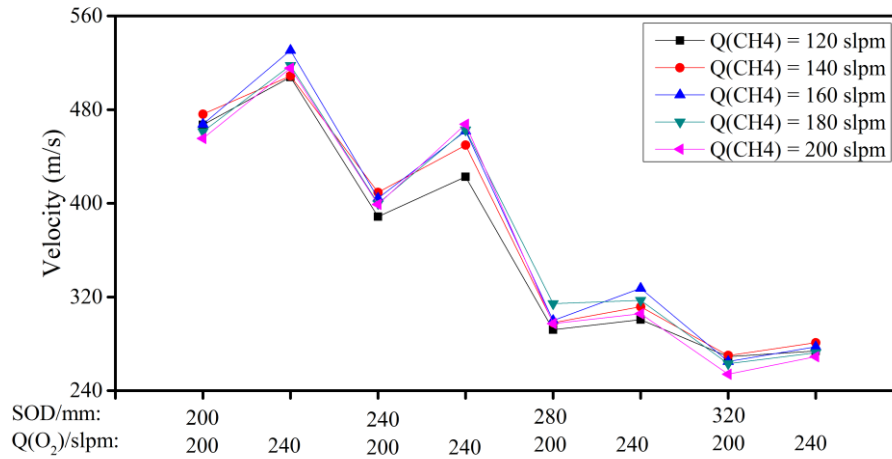


Figure 3.8 Comparison of the velocity of the in-flight particles for different CH₄ flow rates

The SOD clearly affects the velocity of the in-flight particles, as displayed in Figure 3.9. With the increase of SOD, the velocity decreases progressively. The reduction of velocity, when SOD increases, relates to the loss of the kinetic energy of the in-flight particles during flight, resulting from the loss of drag force that is generated by the expansion of gases [17].

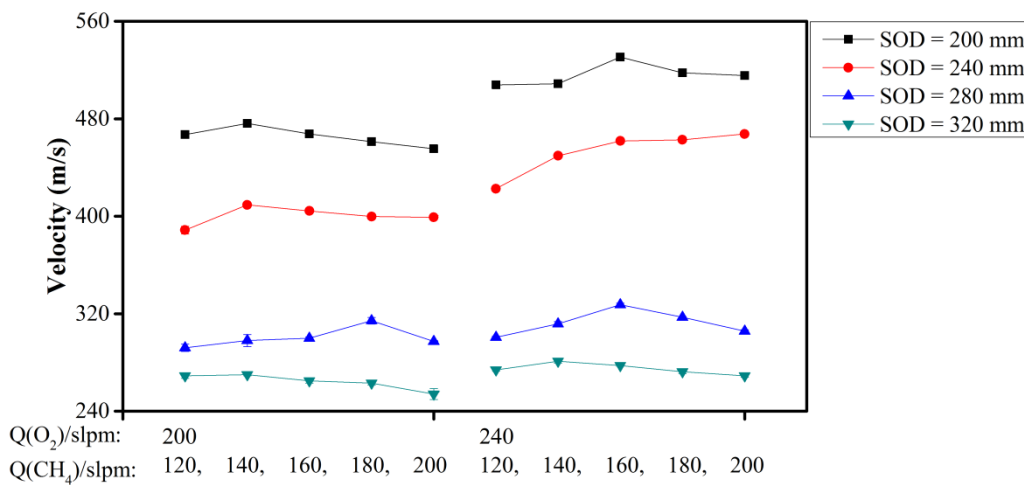


Figure 3.9 Comparison of the velocity of the in-flight particles for different SOD

3.3. Phase composition and coating structure

In the HVOF spray process, the NiCr-Cr₃C₂ powders experience a high temperature that tends to modify the initial powder phases. The carbides are partially dissolved during the process, creating a range of Cr compositions in the matrix, from Cr-rich to the original alloy composition [18]. In addition, dissolved carbon may be lost as CO or CO₂ [19], further promoting the formation of

degradation phases Cr_7C_3 and Cr_{23}C_6 . Furthermore, oxide formation can also occur in flight [18]. Upon depositing on the substrates, a non-equilibrium microstructure is formed, which is composed of metastable carbides (e.g., Cr_7C_3 and Cr_{23}C_6) and of a partly amorphous and/or nanocrystalline matrix [20].

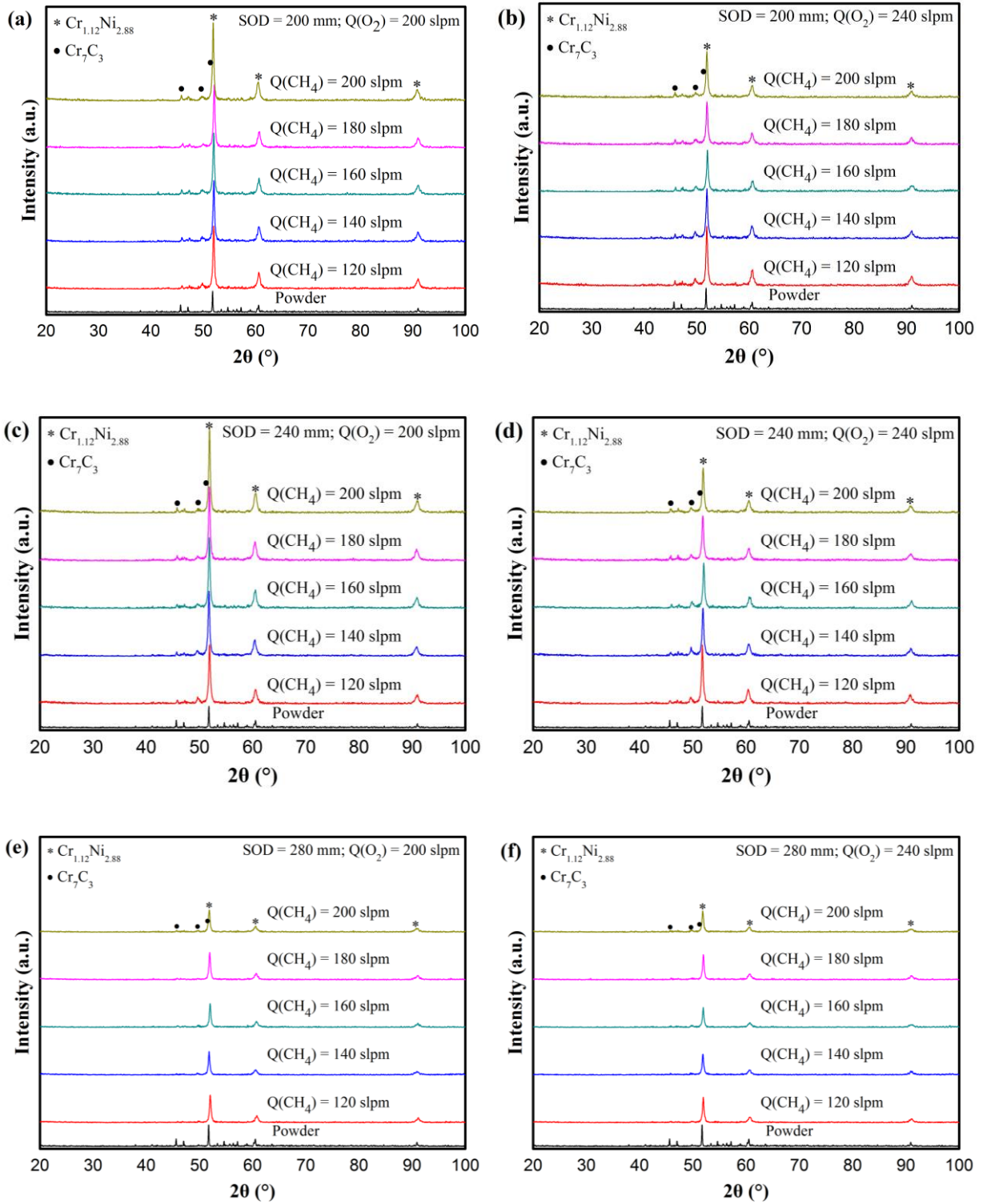
The coating's phase composition and microstructure have a significant influence on the coating's properties. For example, plasma-sprayed coatings usually exhibit extensive carbide dissolution and the formation of brittle carbides and oxy-carbides during the HVOF spray processes, due to the higher temperature of the in-flight particles and residence time [21]. This, together with the higher porosity and lower hardness of the coatings, displays poorer coating performances [22]. Carbide dissolution acts as a key impact in terms of changing the binder hardness and the coating's phase [20]. Therefore, it is necessary to analyze the phase composition and microstructure of coatings in order to analyze coating properties.

3.3.1. The phase composition of coatings

Figure 3.10 displays the XRD patterns of feedstock powers and as-sprayed coatings that result from different spraying conditions. The different phases are also indicated in Figure 3.10, where the main peaks in as-sprayed coatings are identified as $\text{Cr}_{1.12}\text{Ni}_{2.88}$, Cr_7C_3 , and Cr_{23}C_6 . The Bragg peaks (crystalline material) are well defined in the case of the feedstock powders, while a significant peak broadening is observed in all the as-sprayed coatings, due to the dissolution of the carbides and the presence of amorphous phases in the coatings [20, 23].

Strong peaks (at $2\theta = 51.91^\circ$, 60.71° , and 91.23° , according to PDF#65-5559) of the phase $\text{Cr}_{1.12}\text{Ni}_{2.88}$ are recognizable in the coatings. Peaks (at $2\theta = 45.84^\circ$, 49.83° , and 51.77° , according to PDF#36-1482) of the phase Cr_7C_3 , are also obvious in the coatings that are assumed to form because of the decarburization of Cr_3C_2 during spraying. High intensity of the phase Cr_7C_3 has been observed in Figure 3.10 (a)–(d), indicating that the extent of decarburization is significant during deposition, for all the spraying conditions with SOD of 200 mm and 240 mm. Moreover, Figures 3.10 (a), (c), (e), and (g) illustrate that the intensity of the phase $\text{Cr}_{1.12}\text{Ni}_{2.88}$ in as-sprayed coatings that have an oxygen flow rate of 200 slpm, is higher than that in as-sprayed coatings that have an oxygen flow rate of 240 slpm, as indicated in Figures 3.10 (b), (d), (f), and (h). This can be attributed to the higher temperature

of the in-flight particles during spraying with an oxygen flow rate of 240 slpm. A higher temperature of in-flight particles results in a lower crystallinity level, due to greater degradation of the powder [20].



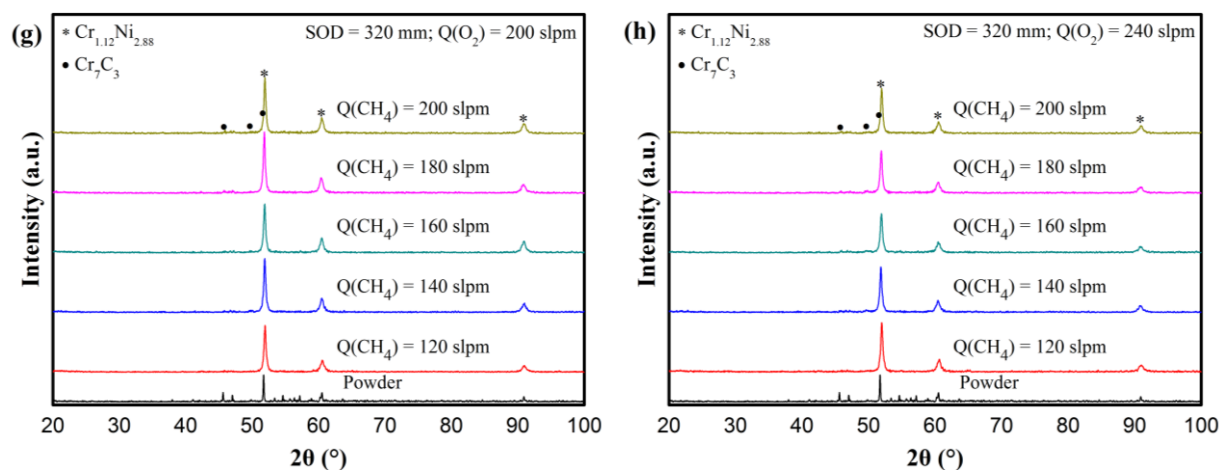
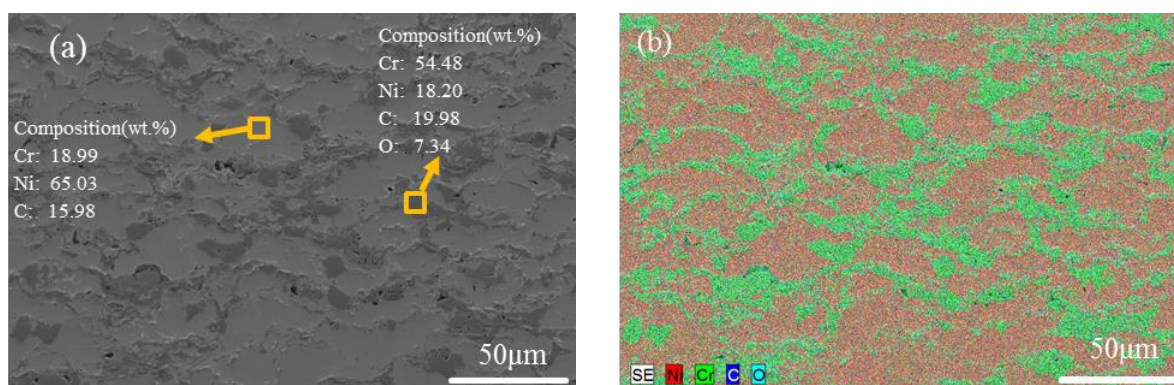


Figure 3.10 XRD patterns of feedstock powders and as-sprayed coatings

Different process parameters produce different phase compositions and structures in the as-sprayed coatings. In this part, a typical morphology (Set 31 in Table 3.2) has been considered as an example to analyze. The Energy Dispersive Spectroscopy (EDS) analysis has also been carried out on the example of Set 31, to further confirm the existence of the desired elements. As shown in Figure 3.11 (a), in the back scattered images of the section of coating, the dark area represents the pores or uneven carbon particles, the dark gray area is the hard carbide phase (polygonal), and the gray area is the NiCr binder phase. Figure 3.11 (b) shows the distribution of all the elements contained in the coatings, while Figure 3.11 (c)–(f) display the distribution of Ni, Cr, C, and O in the coatings.



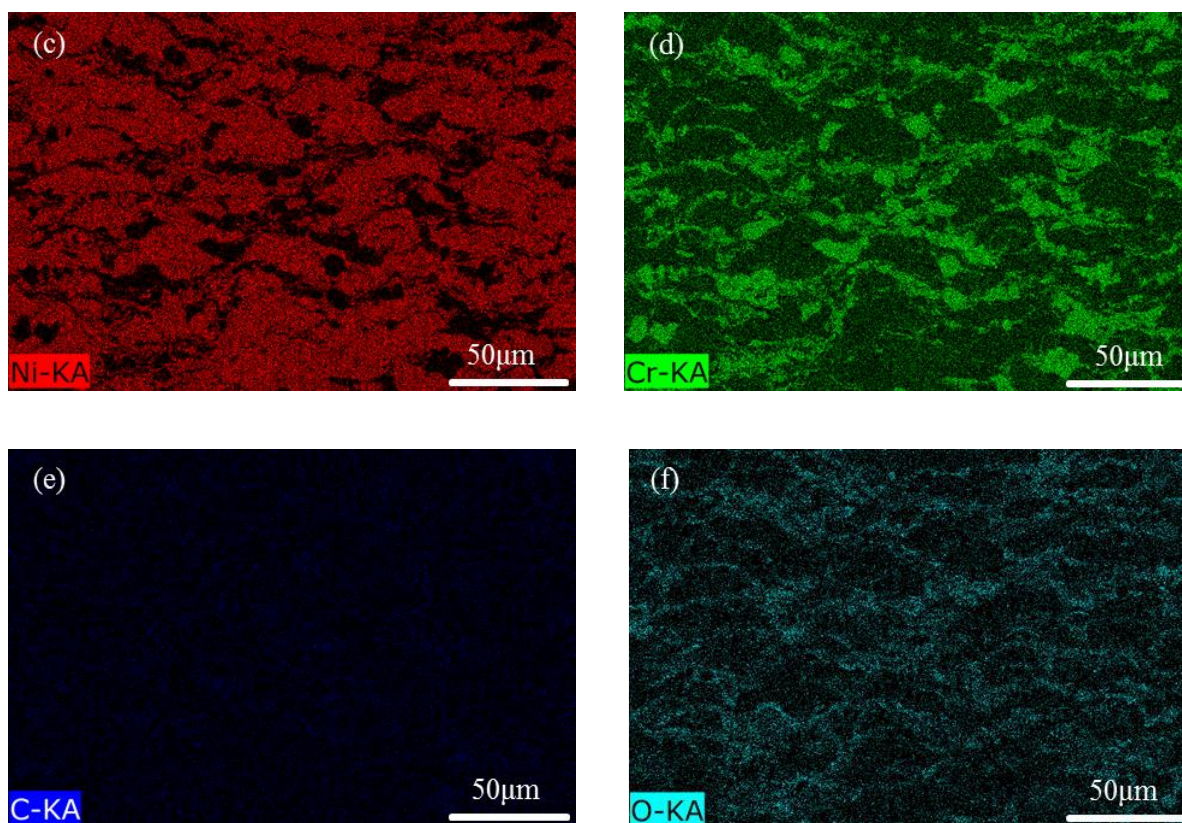


Figure 3.11 EDS spectra analysis of the as-sprayed coatings section

3.3.2. The microstructure of the coatings

Figure 3.12 presents the microstructure of the as-sprayed coatings in Sets 8, 35, 27, and 5 in Table 3.2, which correspond to the spraying conditions that lead to the highest velocity, lowest velocity, highest temperature, and lowest temperature, respectively. Observation of the microstructures in different coatings reveals that the spraying process is robust, as uniform coatings, made of a distribution of the hard carbide phase (in dark gray) in the NiCr binder phase matrix (in light gray), which is obtained for all conditions.

All the coatings are characterized with a few pores visible and with dense lamellae, which is elongated along the direction parallel to the coating surface. The pores are distributed throughout the coating and assumed to be carried into the coatings, resulting from the poor carbide/binder contact and insufficient melting of the binder during spraying. Moreover, upon impact, the particles deformed enough to become incorporated into the coating but not enough to fully collapse the porosity within the particles [24]. Set 8, presented in Figure 3.12 (a), corresponds to the highest particles velocity and exhibits less porosity than Set 35 (Figure 3.12 (b)), which is the “slowest” condition. This can be

attributed to the higher kinetic energy provided by the high velocity in Set 8, which collapses the pores in the coatings. It can also be visually observed that the percentage of the hard carbide phase (in dark gray) in Set 8 is higher than that of Set 35. In addition, the phases also distribute less homogeneously in Set 8. **Figure 3.12 (c)** presents Set 27, which corresponds to the highest particle temperature and exhibits the highest level of porosity of all the spraying conditions. A higher particle temperature aggregates the extent of carbide dissolution into the molten binder and the loss of dissolved carbon as CO/CO₂, which increases the time for oxidation of the particles and generates a more porous feature [24].

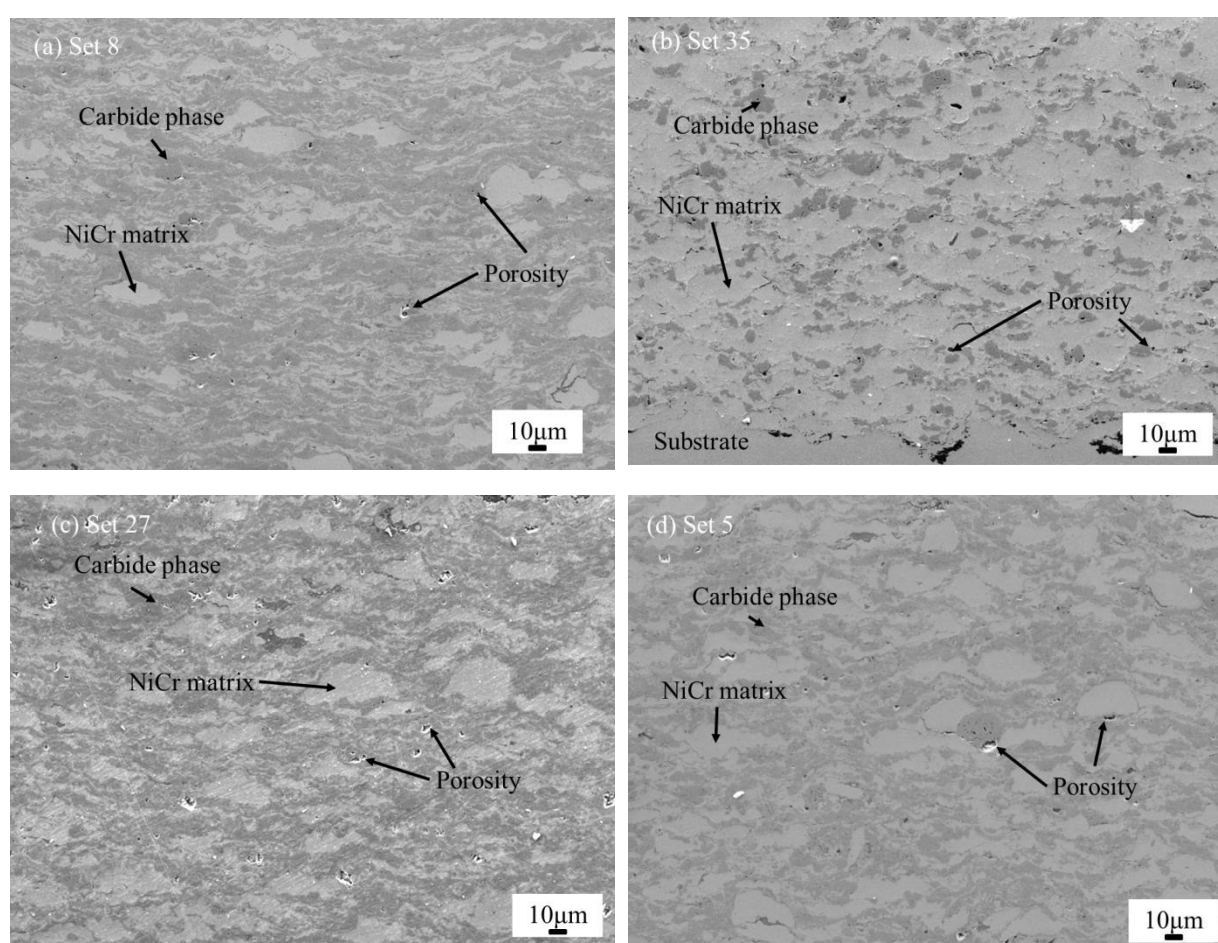


Figure 3.12 Microstructure of the as-sprayed coatings in Set 8 (a), 35 (b), 27 (c), and 5 (d), which correspond to the spraying conditions that lead to the highest velocity, lowest velocity, highest temperature, and lowest temperature

3.4. Analysis of the coating properties

As mentioned in [Section 1.1.4.3](#), the porosity, microhardness, and wear behavior of NiCr-Cr₃C₂

coatings are selected as the representative coating properties to be evaluated and studied. Forty sets of tests were carried out and their results are listed in Table 3.4, where the values are organized into the same order as in Table 3.2. This suggests that the coatings' porosity (PO) varies from $0.144\pm 0.064\%$ to $1.777\pm 0.308\%$, with an average of 0.850% . The coatings' microhardness (MH) varies in the range of 469 ± 33 HV_{0.3} to 958 ± 53 HV_{0.3}, with an average of 662 HV_{0.3}. Additionally, the coatings' wear rate shifts from $0.926\pm 0.053\times 10^{-5}$ mm³/N/m to $15.732\pm 3.950\times 10^{-5}$ mm³/N/m, with an average of 6.244×10^{-5} mm³/N/m. A detailed analysis of the coatings' performance is presented in the following section.

Table 3.4 The porosity, microhardness, and wear rate of coatings

Coatings performances			Coatings performances				
No.	MH [HV _{0.3}]	PO [%area]	WR $\times 10^{-5}$ [mm ³ /N/m]	No.	MH [HV _{0.3}]	PO [%area]	WR $\times 10^{-5}$ [mm ³ /N/m]
1	664 \pm 47	1.08 \pm 0.127	6.039 \pm 0.9	21	565 \pm 39	1.473 \pm 0.23	15.589 \pm 1.561
2	661 \pm 47	1.159 \pm 0.182	5.175 \pm 0.801	22	592 \pm 20	1.372 \pm 0.28	7.122 \pm 1.728
3	727 \pm 66	0.204 \pm 0.065	1.516 \pm 0.335	23	706 \pm 48	1.777 \pm 0.308	6.122 \pm 1.46
4	699 \pm 23	0.182 \pm 0.046	2.217 \pm 0.79	24	624 \pm 50	1.697 \pm 0.158	10.172 \pm 1.537
5	678 \pm 66	0.799 \pm 0.088	1.944 \pm 0.726	25	604 \pm 56	1.231 \pm 0.19	11.741 \pm 2.263
6	721 \pm 39	0.206 \pm 0.094	2.962 \pm 0.708	26	543 \pm 51	1.558 \pm 0.244	10.249 \pm 1.202
7	843 \pm 40	0.151 \pm 0.027	1.624 \pm 0.663	27	659 \pm 36	0.871 \pm 0.203	4.203 \pm 2.156
8	958 \pm 53	0.361 \pm 0.068	1.197 \pm 0.453	28	759 \pm 42	0.996 \pm 0.17	4.467 \pm 1.145
9	893 \pm 66	0.655 \pm 0.161	0.926 \pm 0.315	29	618 \pm 58	1.03 \pm 0.233	4.997 \pm 0.859
10	781 \pm 62	0.144 \pm 0.064	1.764 \pm 0.794	30	678 \pm 35	0.83 \pm 0.333	4.001 \pm 1.304
11	598 \pm 23	0.731 \pm 0.063	10.587 \pm 0.865	31	469 \pm 33	1.113 \pm 0.213	5.061 \pm 0.912
12	707 \pm 18	0.863 \pm 0.179	7.142 \pm 0.771	32	502 \pm 36	0.915 \pm 0.183	9.154 \pm 2.807
13	625 \pm 60	1.134 \pm 0.282	10.144 \pm 0.723	33	544 \pm 45	0.671 \pm 0.124	9.698 \pm 1.606

14	628±67	0.237±0.103	9.235±0.989	34	541±31	0.856±0.119	7.693±0.927
15	650±46	0.266±0.233	6.955±0.943	35	538±18	0.977±0.308	8.92±3.063
16	637±35	1.597±0.324	6.585±0.754	36	483±33	0.883±0.138	15.732±3.95
17	738±38	1.274±0.121	2.802±0.326	37	598±43	0.721±0.2	9.927±3.04
18	832±41	0.444±0.115	2.926±0.823	38	596±34	0.803±0.09	5.54±1.567
19	833±61	0.299±0.179	2.221±0.912	39	597±41	0.995±0.084	6.941±1.646
20	802±53	0.576±0.112	1.59±0.534	40	578±39	0.87±0.173	6.881±1.659

, where MH, PO, and WR represent the microhardness, porosity, and wear rate of coatings, respectively.

3.4.1. The porosity of the coatings

Figure 3.13 illustrates the characterization results of coating porosity, in relation to the velocity and temperature of in-flight particles. In Figure 3.13 (a), the bigger symbol refers to the three-dimensional coordinate value and the small symbol refers to the projection on the XY plane, which is also clearly displayed in Figure 3.13 (b). Variations of the value of porosity are represented by variations of color. The porosity of coatings varies from $0.144\pm 0.064\%$ to $1.777\pm 0.308\%$. The highest value occurs with a velocity of 274 m/s and a temperature of 2409 K, while the lowest value corresponds to the velocity of 518 m/s and temperature of 2120 K. The higher values of porosity mainly occur with relatively lower velocity (250 to 330 m/s) and higher temperatures (2250 to 2451 K). However, there are also some high values located in the region of moderate velocity (380 to 480 m/s) and moderate temperature (2100 to 2250 K). The histogram of coatings porosity is shown in Figure 3.14, which indicates that the majority of coating porosity values are located in the range of 0.6% to 1.2% and the percentage of coating porosity from 0.8% to 1.0% can reach up to 27.5%.

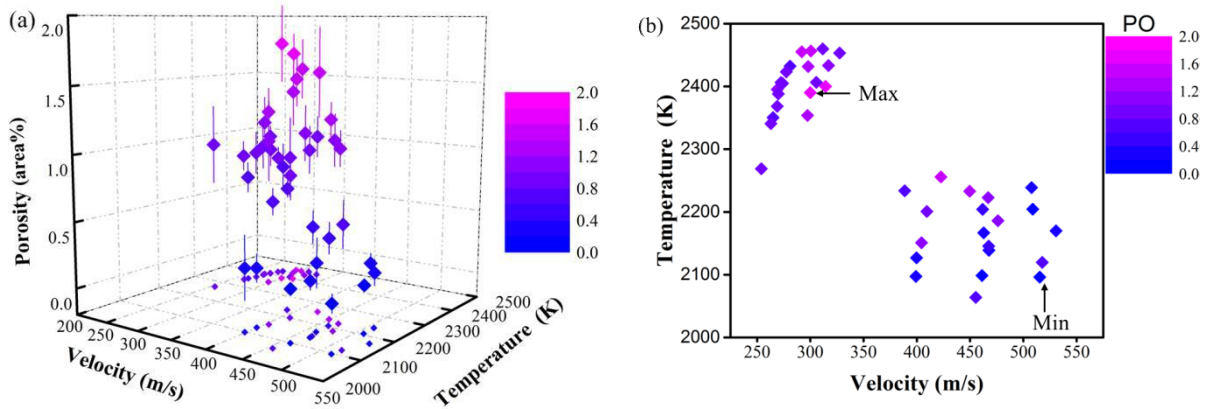


Figure 3.13 The 3D (a) and 2D (b) distribution of the coating's porosity, with respect to the temperature and velocity of in-flight particles

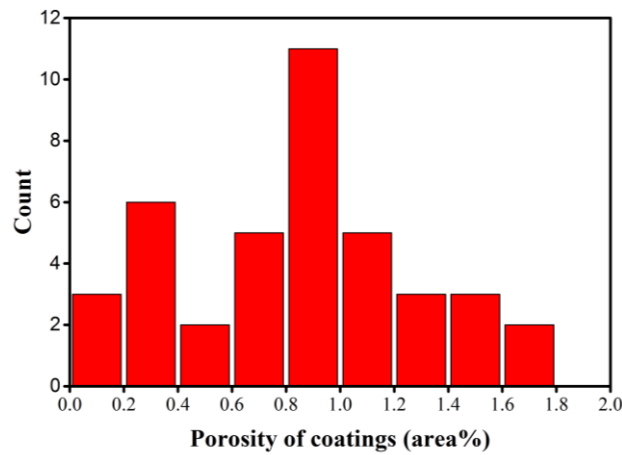


Figure 3.14 Histogram of the coating's porosity

It can be deduced that both velocity and temperature significantly influence coating porosity. However, there are no obvious relationships between the behaviors of in-flight particles and coating porosity. Further research needs to be undertaken that explores predicting coating porosity, with respect to the behaviors of in-flight particles (the temperature and velocity of in-flight particles).

3.4.2. The microhardness of the coatings

The distribution of the coating microhardness is mainly concentrated in the range of 469 ± 33 to 958 ± 53 HV_{0.3}, as shown in Figure 3.15. The same illustrating method is taken as in Figure 3.13. Figure 3.15 (a) demonstrates the 3D distribution, while Figure 3.15 (b) gives the projection on the XY plane. Most of the relatively higher values for microhardness are related to higher velocity (460 to 550 m/s) and lower temperature (< 2200 K). The higher values of microhardness are generally related to higher velocity, while the lower values normally correspond to lower velocity. The histogram of

coating microhardness (Figure 3.16) shows that coating microhardness is limited to the range of 400 HV_{0.3} to 1000 HV_{0.3}, with the majority from 500 HV_{0.3} to 700 HV_{0.3} (possessing proportion high up to 62.5%).

Although the velocity of in-flight particles obviously has a greater impact on coating microhardness than the temperature, it is impossible to directly correlate the performances of in-flight particles and microhardness. Therefore, a more precise model is needed to predict and study the influence of the performances of in-flight particles on coating microhardness.

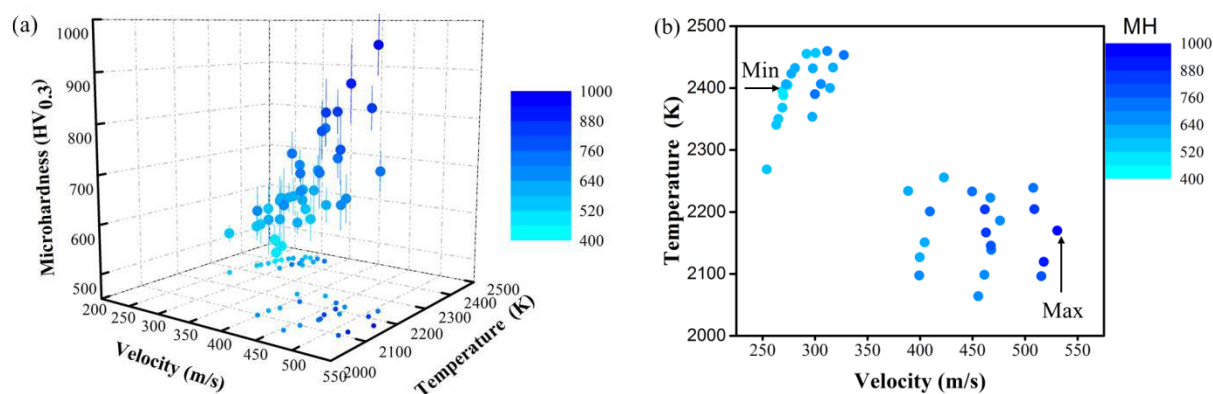


Figure 3.15 The 3D (a) and 2D (b) distribution of coating's microhardness, with respect to temperature and velocity of in-flight particles

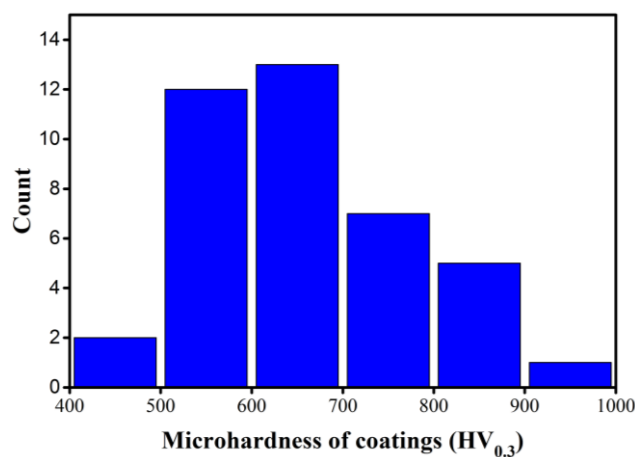


Figure 3.16 Histogram of coating's microhardness

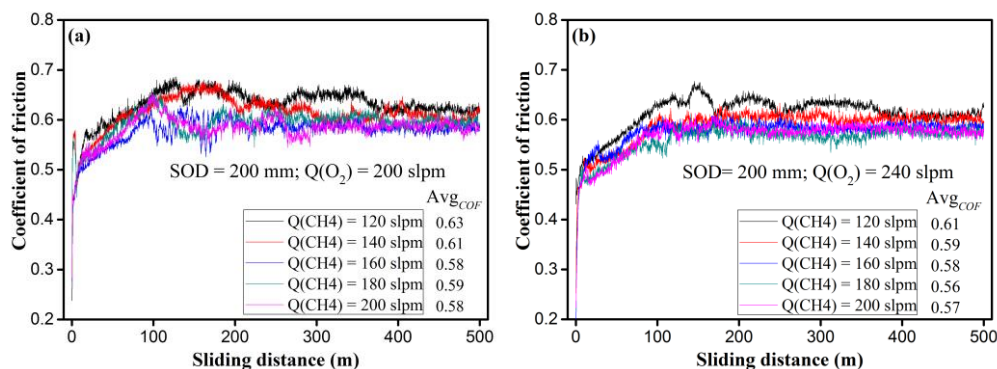
3.4.3. The wear performance of the coatings

The HVOF sprayed NiCr-Cr₃C₂ coatings, with dispersion of hard ceramic particles in a relatively ductile and tough matrix, have been used for wear-resistant applications, as they offer considerable mechanical strength, hardness, and toughness. This section outlines the wear abrasive characteristic

for NiCr-Cr₃C₂ coatings. First, the coefficient of friction (COF) of the coatings is analyzed, with respect to different process parameters that are listed in Table 3.2, in order to observe the effect of the process parameters on the coatings' wear behaviors. Then, the influence of in-flight particles on coating wear rate is discussed further. Finally, the investigation into the abrasive wear behavior of coatings is briefly described.

Effect of process parameters on coating' COF

The COF vs. sliding distance plots for NiCr-Cr₃C₂ coatings at different process parameters are listed in Table 3.2 and shown in Figure 3.17 (a)–(h). This illustrates that, initially, the COF normally increases sharply for a sliding distance of 50–100 m, which is followed by a fluctuation, before it finally reaches a steady state regime, which occurs after a sliding distance of 150–200 m. Greater fluctuation can be observed for the CH₄ flow rate of 120 slpm (black line in the figures) and for the average value of COF (Avg_{COF}), which is also higher than the other CH₄ flow rates in all the figures. The Avg_{COF} was also calculated and is listed in Figure 3.17 (a)–(h), which focuses on the range of 0.57 to 0.68. Generally speaking, it can be observed that the Avg_{COF} increases as the SOD increases. An opposite result can be summarized for the influence of the O₂ flow rate. Comparing the Avg_{COF} that corresponds to the O₂ flow rate of 200 slpm (Figure 3.17 (a), (c), (e), (g)) with that of the O₂ flow rate of 240 slpm, which are presented in Figure 3.17 (b), (d), (f), and (h), clearly indicates that the Avg_{COF} decreases along with the increase of the O₂ flow rate. However, different tendencies of the Avg_{COF} can be concluded for the influence of variations in the CH₄ flow rate. For instance, the Avg_{COF} first decreases and then increases with the increase in the CH₄ flow rate, as shown in Figure 3.17 (a) and (e). Meanwhile, the Avg_{COF} continuously decreases with the increase of the CH₄ flow rate which is presented in Figure 3.17 (g). Random fluctuation can be observed in other figures.



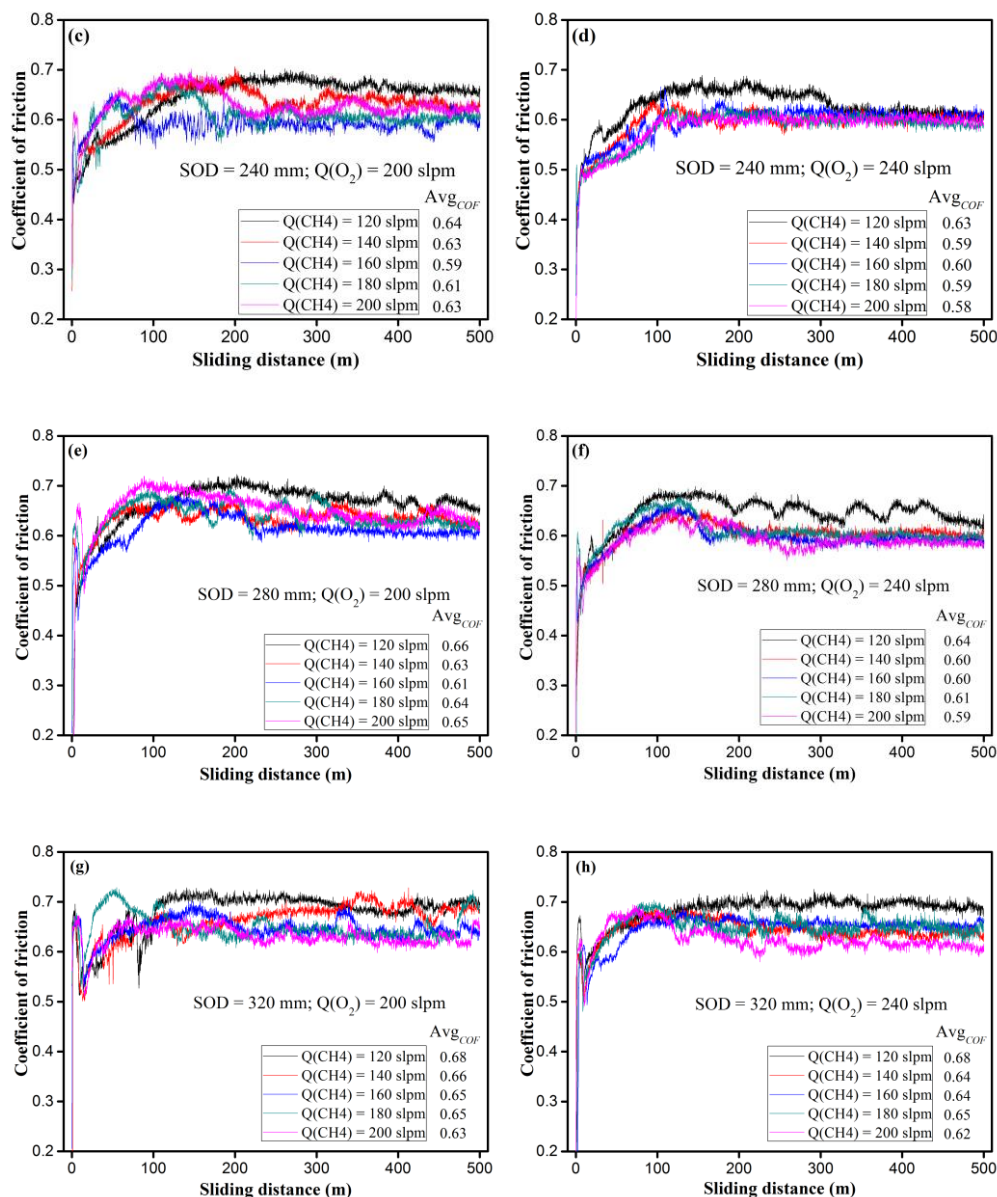


Figure 3.17 Variation of COF with sliding distance at process parameters of SOD of 200 mm (a and b), 240 mm (c and d), 280 mm (e and f), and 320 mm (g and h), as well as an O₂ flow rate of 200 slpm (a, c, e, and g) and 240 slpm (b, d, f, and h)

Effect of the behavior of in-flight particles on coatings' wear rate

The abrasive wear rates were plotted vs. the temperature and velocity of in-flight particles, as shown in Figure 3.18 (a) (3D distribution) and (b) (projection on the XY plane). The coating's wear rate distributes randomly and varies in the range of $0.926 \pm 0.053 \times 10^{-5} \text{ mm}^3/\text{N}/\text{m}$ to $15.732 \pm 3.950 \times 10^{-5} \text{ mm}^3/\text{N}/\text{m}$. Most of the relatively higher values of the wear rate are related to lower velocity (250 to 330 m/s) and higher temperature ($> 2250 \text{ K}$). Generally speaking, the higher values of coatings' wear rate are related to lower velocity, while the lower values normally correspond to higher velocity. The

highest value of coatings' wear rate occurs with the temperature of 2405 K and velocity of 274 m/s, while the lowest values correspond to a temperature of 2120 K and velocity of 518 m/s. The histogram of coatings' wear rate (Figure 3.19) shows that the wear rate distributes nearly homogeneously, in the range of 0 and $12 \times 10^{-5} \text{ mm}^3/\text{N/m}$, with the highest proportion of 22.5% for the wear rate from $6 \times 10^{-5} \text{ mm}^3/\text{N/m}$ to $8 \times 10^{-5} \text{ mm}^3/\text{N/m}$.

From this, it can be visually summarized that the velocity of in-flight particles has a greater impact on coatings' wear rate than the temperature, even though some low values of wear rate exist in the region of low velocity. Overall, it is still impossible to directly relate the performances of in-flight particles to coatings' wear rate. Therefore, a more precise model is needed to predict and study the influence of the performances of in-flight particles on coatings' wear rate.

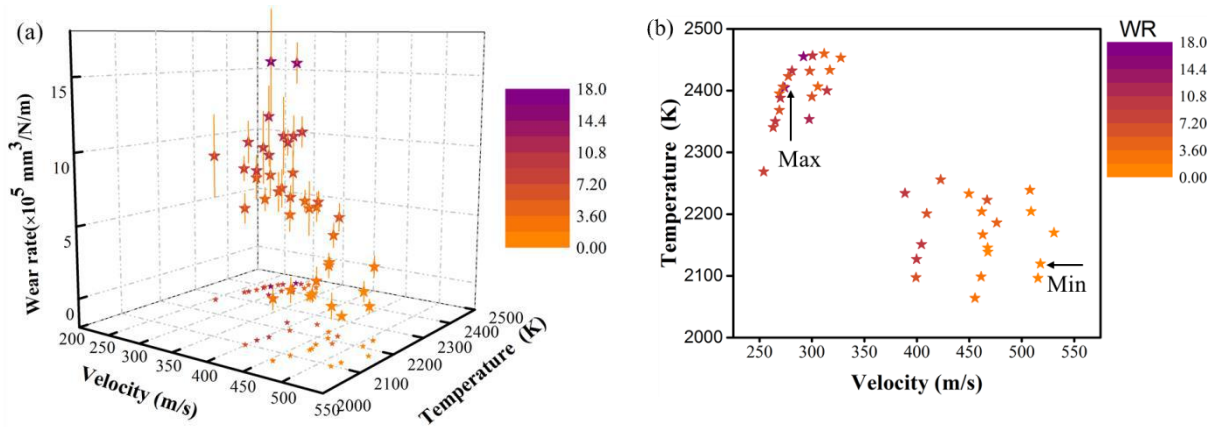


Figure 3.18 The 3D (a) and 2D (b) distribution of coatings' wear rate with respect to the temperature and velocity of in-flight particles

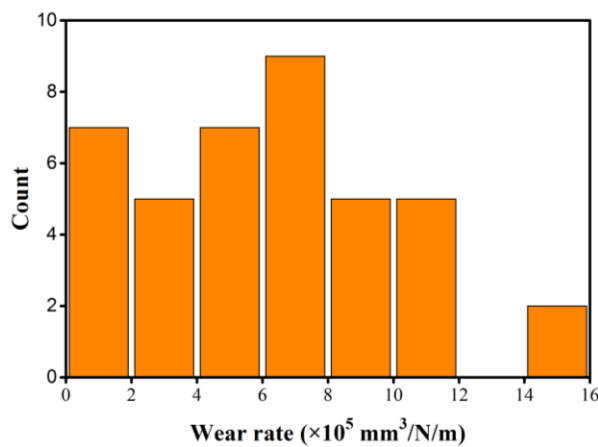


Figure 3.19 Histogram of coating's wear rate

3.5. Conclusions

This chapter has introduced the experimental procedure of the HVOF spray process and discussed the investigation into the relationship between process parameters, behaviors of in-flight particles, and coating properties. Together, this offers a preliminary understanding of the HVOF process and HVOF sprayed coatings.

HVOF experiments were scheduled and 40 sets of spray were subsequently conducted, based on the selection of three main factors: SOD, O₂ flow rate, and CH₄ flow rate.

The temperature and velocity of the in-flight particles have been analyzed, with respect to the HVOF process parameters. From this, it can be concluded that the temperature tends to grow as the O₂ flow rate increases. In addition, an initially increasing then decreasing trend can be observed, as SOD increases. The increased O₂ flow rate increases the velocity of the in-flight particles. However, with the increase of SOD, the effect of the O₂ flow rate on the velocity of the in-flight particles gradually disappears. The velocity decreases progressively, as SOD increases. Although the effect of HVOF process parameters on the behaviors of in-flight particles can be approximately summarized, it is impossible to establish a direct connection between them. Thus, a more precise prediction is necessary.

The phase components and microstructure of NiCr-Cr₃C₂ coatings, which has been discussed prior to analysis of the coating properties, provide fundamental knowledge about HVOF sprayed NiCr-Cr₃C₂ coatings. Subsequently, the porosity, microhardness, and wear rate of coatings have been discussed, considering the influence of the behaviors of in-flight particles. From this, it can be concluded that both the velocity and temperature of in-flight particles have an impact on coatings' properties. However, it remains impossible to directly relate the performances of in-flight particles to coating properties. Thus, a more accurate model is needed to predict and study the influence of the behaviors of in-flight particles on coating properties. Therefore, machine learning methods, particularly the ANN models, are introduced in the following chapters, in order to address this challenge.

Reference of chapter 3

- [1] F.-I. Trifa, G. Montavon, C. Coddet, On the relationships between the geometric processing parameters of APS and the Al₂O₃–TiO₂ deposit shapes, *Surface and Coatings Technology*, 195 (2005) 54-69.
- [2] D. Fang, S. Deng, H. Liao, C.J.J.o.t.s.t. Coddet, The effect of robot kinematics on the coating thickness uniformity, 19 (2010) 796-804.
- [3] Z. Cai, S. Deng, H. Liao, C. Zeng, G.J.J.o.t.s.t. Montavon, The effect of spray distance and scanning step on the coating thickness uniformity in cold spray process, 23 (2014) 354-362.
- [4] W.-C. Lih, S. Yang, C. Su, S. Huang, I. Hsu, M.J.S. Leu, C. Technology, Effects of process parameters on molten particles speed and surface temperature and the properties of HVOF CrC/NiCr coatings, 133 (2000) 54-60.
- [5] Q. Wang, Z. Chen, L. Li, G.J.S. Yang, C. Technology, The parameters optimization and abrasion wear mechanism of liquid fuel HVOF sprayed bimodal WC–12Co coating, 206 (2012) 2233-2241.
- [6] A.S. Praveen, J. Sarangan, S. Suresh, B.J.C.I. Channabasappa, Optimization and erosion wear response of NiCrSiB/WC–Co HVOF coating using Taguchi method, 42 (2016) 1094-1104.
- [7] M. Xie, Y. Lin, P. Ke, S. Wang, S. Zhang, Z. Zhen, L.J.C. Ge, Influence of process parameters on high velocity oxy-fuel sprayed Cr₃C₂-25% NiCr coatings, 7 (2017) 98.
- [8] G.-C. Ji, C.-J. Li, Y.-Y. Wang, W.-Y.J.S. Li, C. Technology, Microstructural characterization and abrasive wear performance of HVOF sprayed Cr₃C₂–NiCr coating, 200 (2006) 6749-6757.
- [9] W. Zhou, K. Zhou, Y. Li, C. Deng, K.J.A.S.S. Zeng, High temperature wear performance of HVOF-sprayed Cr₃C₂-WC-NiCoCrMo and Cr₃C₂-NiCr hardmetal coatings, 416 (2017) 33-44.
- [10] V. Matikainen, G. Bolelli, H. Koivuluoto, P. Sassatelli, L. Lusvarghi, P.J.W. Vuoristo, Sliding wear behaviour of HVOF and HVAF sprayed Cr₃C₂-based coatings, 388 (2017) 57-71.
- [11] L. Janka, L.-M. Berger, J. Norpoth, R. Trache, S. Thiele, C. Tomastik, V. Matikainen, P.J.S. Vuoristo, C. Technology, Improving the high temperature abrasion resistance of thermally sprayed Cr₃C₂-NiCr coatings by WC addition, 337 (2018) 296-305.
- [12] H. Zhang, X. Dong, S.J.A.i.M.E. Chen, Solid particles erosion-wear behaviour of Cr₃C₂–NiCr coating on Ni-based superalloy, 9 (2017) 1687814017694580.
- [13] F. Fanicchia, D. Axinte, J. Kell, R. McIntyre, G. Brewster, A.J.S. Norton, C. Technology, Combustion flame spray of CoNiCrAlY & YSZ coatings, 315 (2017) 546-557.
- [14] C.-J. Li, G.-C. Ji, Y.-Y. Wang, K.J.T.S.F. Sonoya, Dominant effect of carbide rebounding on the carbon loss during high velocity oxy-fuel spraying of Cr₃C₂–NiCr, 419 (2002) 137-143.
- [15] J. Saedi, T. Coyle, H. Arabi, S. Mirdamadi, J.J.J.o.t.s.t. Mostaghimi, Effects of HVOF process parameters on the properties of Ni-Cr coatings, 19 (2010) 521-530.

- [16] X. Guo, M.-P. Planche, J. Chen, H.J.J.o.M.P.T. Liao, Relationships between in-flight particles characteristics and properties of HVOF sprayed WC-CoCr coatings, 214 (2014) 456-461.
- [17] A. Pukasiewicz, H. De Boer, G. Sucharski, R. Vaz, L.J.S. Procopiak, C. Technology, The influence of HVOF spraying parameters on the microstructure, residual stress and cavitation resistance of FeMnCrSi coatings, 327 (2017) 158-166.
- [18] S. Matthews, M. Hyland, B.J.J.o.T.S.T. James, Long-term carbide development in high-velocity oxygen fuel/high-velocity air fuel Cr₃C₂-NiCr coatings heat treated at 900 C, 13 (2004) 526-536.
- [19] J. Guilemany, J. Miguel, S. Vizcaino, C. Lorenzana, J. Delgado, J.J.S. Sanchez, C. Technology, Role of heat treatments in the improvement of the sliding wear properties of Cr₃C₂-NiCr coatings, 157 (2002) 207-213.
- [20] D. Poirier, J.-G. Legoux, R.S.J.J.o.t.s.t. Lima, Engineering HVOF-sprayed Cr₃C₂-NiCr coatings: the effect of particles morphology and spraying parameters on the microstructure, properties, and high temperature wear performance, 22 (2013) 280-289.
- [21] V. Shukla, V. Tewari, R.J.I.J.M.S.E. Jayaganthan, Comparison of tribological behavior of Cr₃C₂/NiCr coatings deposited by different thermal spray techniques: a review, 2 (2011) 55-58.
- [22] X. Li, Y. Yang, T. Shao, Y. Jin, G.J.W. Barbezat, Impact wear performances of Cr₃C₂-NiCr coatings by plasma and HVOF spraying, 202 (1997) 208-214.
- [23] C. Verdon, A. Karimi, J.-L.J.M.S. Martin, E. A, A study of high velocity oxy-fuel thermally sprayed tungsten carbide based coatings. Part 1: Microstructures, 246 (1998) 11-24.
- [24] S. Matthews, A. Asadov, S. Ruddell, L.-M.J.J.o.A. Berger, Compounds, Thermally induced metallurgical processes in Cr₃C₂-NiCr thermal spray coatings as a function of carbide dissolution, 728 (2017) 445-463.
- [25] N. Vashishtha, R. Khatirkar, S.J.T.I. Sapate, Tribological behaviour of HVOF sprayed WC-12Co, WC-10Co-4Cr and Cr₃C₂-25NiCr coatings, 105 (2017) 55-68.

Chapter 4. Setup, training, and test of the artificial intelligence

Introduction

As discussed in [Chapter 3](#), the coating properties are sensitive to the behaviors of in-flight particles, which are mainly influenced by the processing parameters of the HVOF technology. However, due to the complex chemical and thermodynamic reactions that occur during the deposition procedure, obtaining a comprehensive multi-physical modeling or analytical analysis of the HVOF process remains a challenge.

This thesis develops a robust methodology via the ANN to address this problem, for the HVOF sprayed NiCr-Cr₃C₂ coatings under different operating parameters. The ANN methodology is used for applications in which formal analysis is difficult or impossible, such as pattern recognition and nonlinear system identification and control [1]. This is a powerful statistical method that recognizes correlations between the parameters of a given problem and its responses. This chapter reports on a comparison of the ANN model and other machine learning methods, which was carried out to confirm the superiority of ANN models. Subsequently, two ANN models have been implemented to predict coating performances (microhardness, porosity, and wear rate) and to analyze the influence of operating parameters (SOD, O₂ flow rate, and CH₄ flow rate), considering the intermediate process (temperature [T] and velocity [v] of the in-flight particles), as displayed in [Figure 4.1](#). A detailed procedure was presented that considered two optimized ANN structures, which encode the implicitly physical phenomena that governs the HVOF process. Finally, the importance of the inputs on the specific output has been assessed using MIV-based analysis.

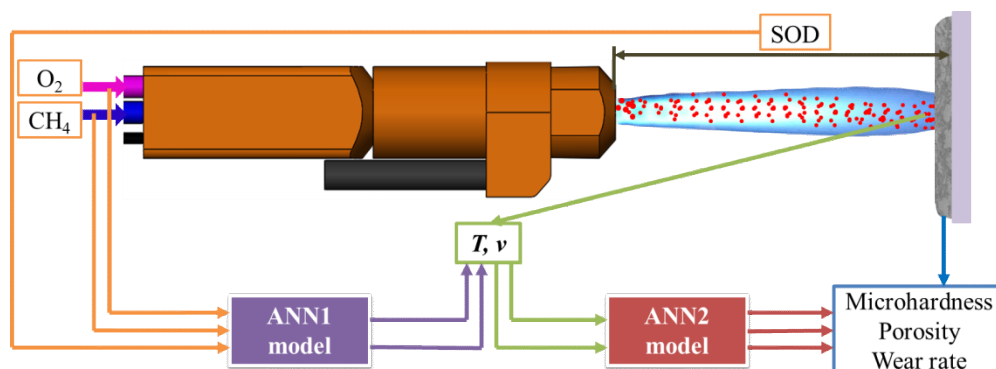


Figure 4.1 Data flow diagram of ANN models

4.1. Collection and pre-processing of the dataset

The first step in terms of modeling is to collect data and pre-process that data for follow-up learning and training. A robust and sufficiently large database is essential for the construction of a model that generalizes well [2]. As introduced in Chapter 3, HVOF experiments, the measurement of in-flight particles, and coatings' characterization have been carried out to collect data for modeling. A database of 320 pieces of data that derive from 40 sets of experiments and tests were created. The data required a linear transformation, before being used for modeling. In this work, the data was normalized according to Eq. (4.1), to fall into the range [-1, 1], in order to avoid the calculation error related to different parameter magnitudes and to ensure equal treatment from the ANN model and other machine learning methods during training and learning [2].

$$X_{NORM} = 2 (X - X_{MIN}) / (X_{MAX} - X_{MIN}) - 1 \quad \text{Eq. (4.1)}$$

, where, X_{NORM} is the normalized value; X is the real value; X_{MAX} is the maximum of the real value, X_{MIN} is the minimum of the real value.

X_{MAX} and X_{MIN} are the maximum and minimum possible values of the parameters, based on their physical limitations in the process, as opposed to the values from the experimental sets. In this work, the limitations of each input and output variable were assessed, which are presented in Table 4.1. For the spray system that used gas as fuel, the SOD is supposed to be expanded to range from 150 mm to 400 mm, considering the real spraying condition and the data collected from the existing literature [3-5]. The maximum oxygen flow rate ($Q(O_2)$) and CH₄ flow rate ($Q(CH_4)$) were set according to the gas capacities that were supplied by the system. The minimum values were set considering the maintenance of the shock diamond, which is the symbol of the HVOF flame. The range of the other variables, including velocity (V_E) and the temperature (T_E) of the in-flight particles, as well as the coating's microhardness (MH), porosity (PO), and wear rate (WR), are, were all expanded based on the data obtained in this work. After normalization, the datasets were employed for the following training and learning.

Table 4.1 Physical limits of the input and output variables

	<i>SOD</i>	<i>Q(O₂)</i>	<i>Q(CH₄)</i>	<i>V_E</i>	<i>T_E</i>	<i>MH</i>	<i>PO</i>	<i>WR</i>
	/mm	/slpm	/slpm	/[m/s]	/K	HV _{0.3}	/%	/[mm/N/m]
<i>X_{MIN}</i>	150	150	100	200	1500	400	0	0
<i>X_{MAX}</i>	400	300	250	600	3000	1000	2	20×10 ⁻⁵

4.2. Comparison of different machine learning methods

Machine learning methods, which are seen as a subset of artificial intelligence, are the scientific study of algorithms and statistical models that computer systems use to perform a specific task. This is completed using patterns and inference, instead of explicit instructions [6]. Thus, its powerful models can be applied to various applications, including ANN, decision trees, support vector machines, Bayesian networks, and genetic algorithms. In this work, the optimization and prediction of the outputs that are based on the inputs information are expected, which is a kind of regression problem. Therefore, various regression models are employed and the results are compared to obtain the best predicted model in MATLAB.

MATLAB offers various regression models for training, including linear regression models, regression trees, Gaussian process regression (GPR) models, SVM, and ensembles of regression trees. In this work, all of these models and their sub-models have been used and trained to select a suitable model. The root mean square error (RMSE), which is defined by Eq. (4.2), has been chosen as an indicator to evaluate the performance of models. It is for sure that the smaller the RMSE, the better the prediction performance.

$$RMSE = \sqrt{\left(\frac{1}{N}\right) \sum_{i=1}^N (e_i)^2} = \sqrt{\left(\frac{1}{N}\right) \sum_{i=1}^N (t_i - a_i)^2} \quad \text{Eq. (4.2)}$$

, where t_i is the experimental result; a_i is the predicted result; e_i is the difference between the experimental result and the predicted result; N is the number of the data sets.

As depicted in Figure 4.2, the temperature and velocity of the in-flight particles have been predicted based on the features of the SOD, O₂ flow rate, and CH₄ flow rate, with 19 regression

models. The GPR models demonstrate better performance than the other models. A detailed description of these GPR models is given in [7]. The best result was obtained using the squared exponential GPR model with a RMSE of 0.050 for velocity and 0.034 for temperature. Generally speaking, the prediction accuracy for temperature is better than that for velocity, which can be attributed to the relatively higher regular tendency of the temperature of in-flight particles.

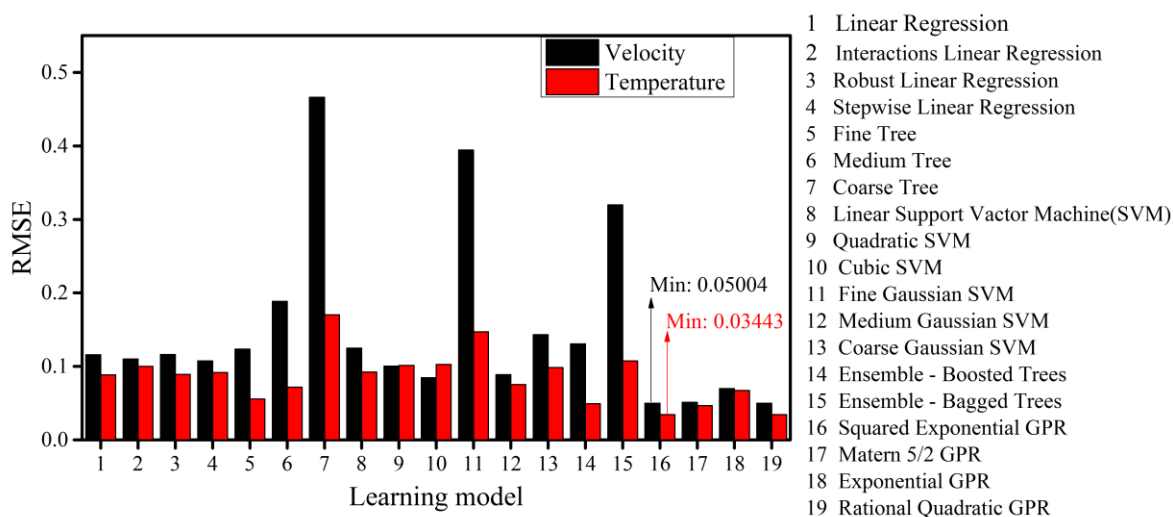


Figure 4.2 RMSEs of some regression models for predicting the temperature and velocity of in-flight particles

Similarly, the microhardness, porosity, and wear rate of coatings have been forecasted based on the features of the temperature and velocity of in-flight particles, as depicted in Figure 4.3. From this, it is clear that the best results have been obtained by the squared exponential GPR model for microhardness, with a RMSE of 0.206, the exponential GPR model for porosity, with a RMSE of 0.362, and the medium tree regression model for wear rate with a RMSE of 0.267. A comparison of the RMSE suggests that the prediction performance for predicting coating properties is worse than forecasting the behaviors of in-flight particles. This can be explained by the more complex mechanism of the coating properties.

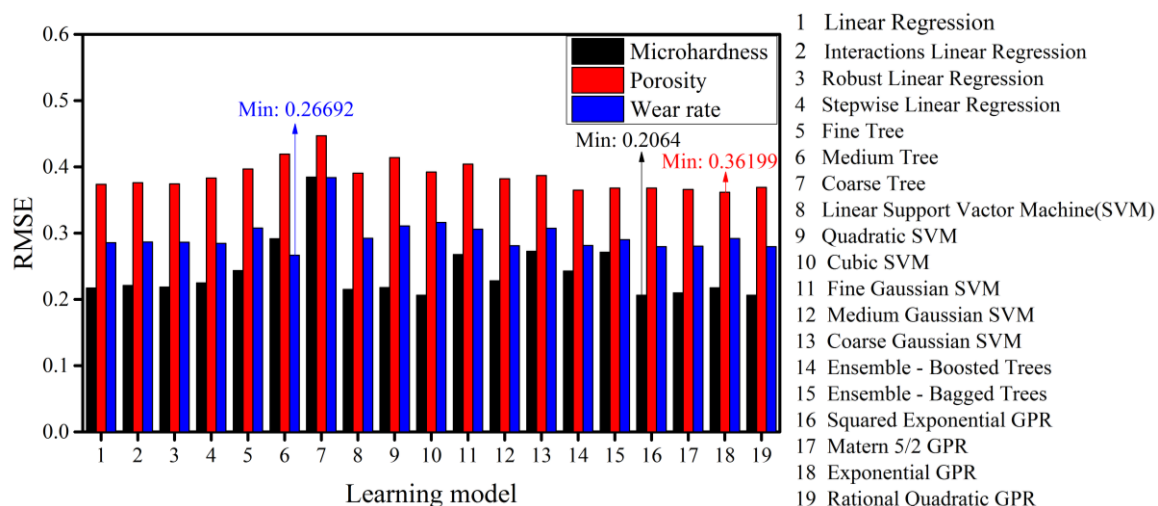
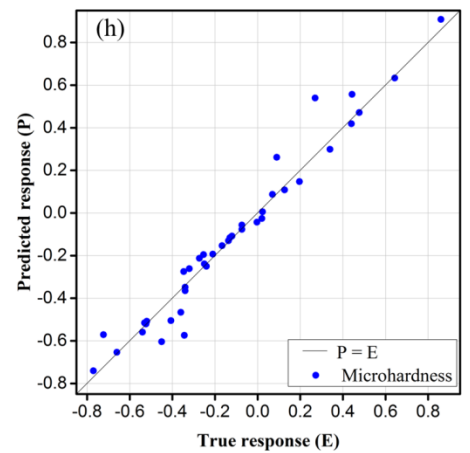
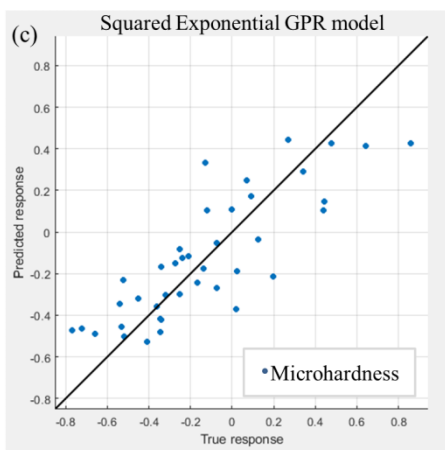
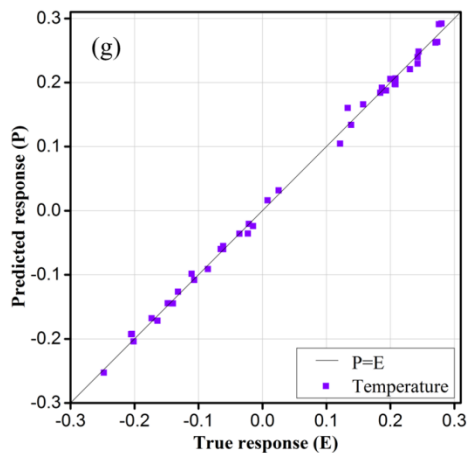
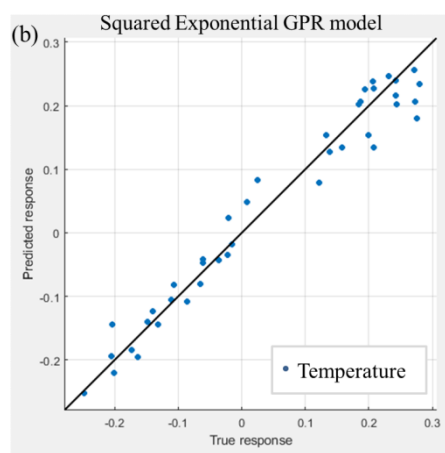
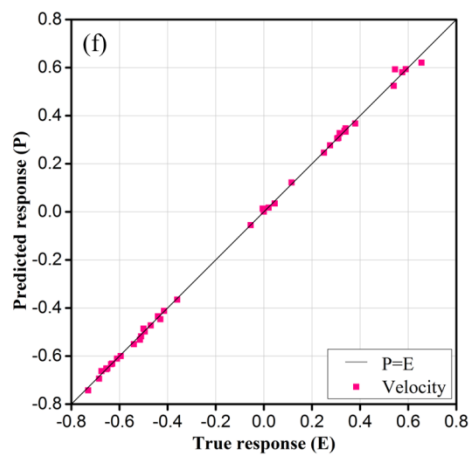
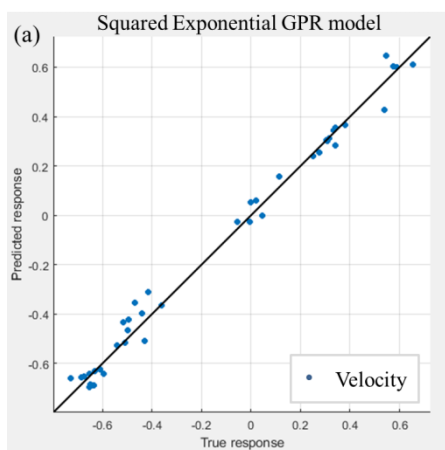


Figure 4.3 RMSEs of some regression models for predicting the microhardness, porosity, and wear rate of coatings

The model with the best performance, as discussed and obtained by the aforementioned comparison, is compared to the performance of the ANN model to predict a specific response, as showed in Figure 4.4. The functions and parameters for training the ANN models were set as default, and the architectures were all set as five neurons in the first and second hidden layers. Figure 4.4 (a)–(e) illustrates the comparison between the true response and predicted response of selected machine learning models, while Figure 4.4 (f)–(j) display that of the ANN models. The solid line represents the perfect result, which means the predicted results are exactly equal to the true responses. Therefore, the closer the point are to the solid line, the better the predict performance. From this, it is clear that the response predicted by the ANN model is highly consistent with the experimental values and is located closer to the solid line than the result of selected machine learning models. This demonstrates that the ANN model performs better with these prediction requirements. Consequently, the ANN model could be applied and further optimized to predict the in-flight particles' behaviors and coating performances.



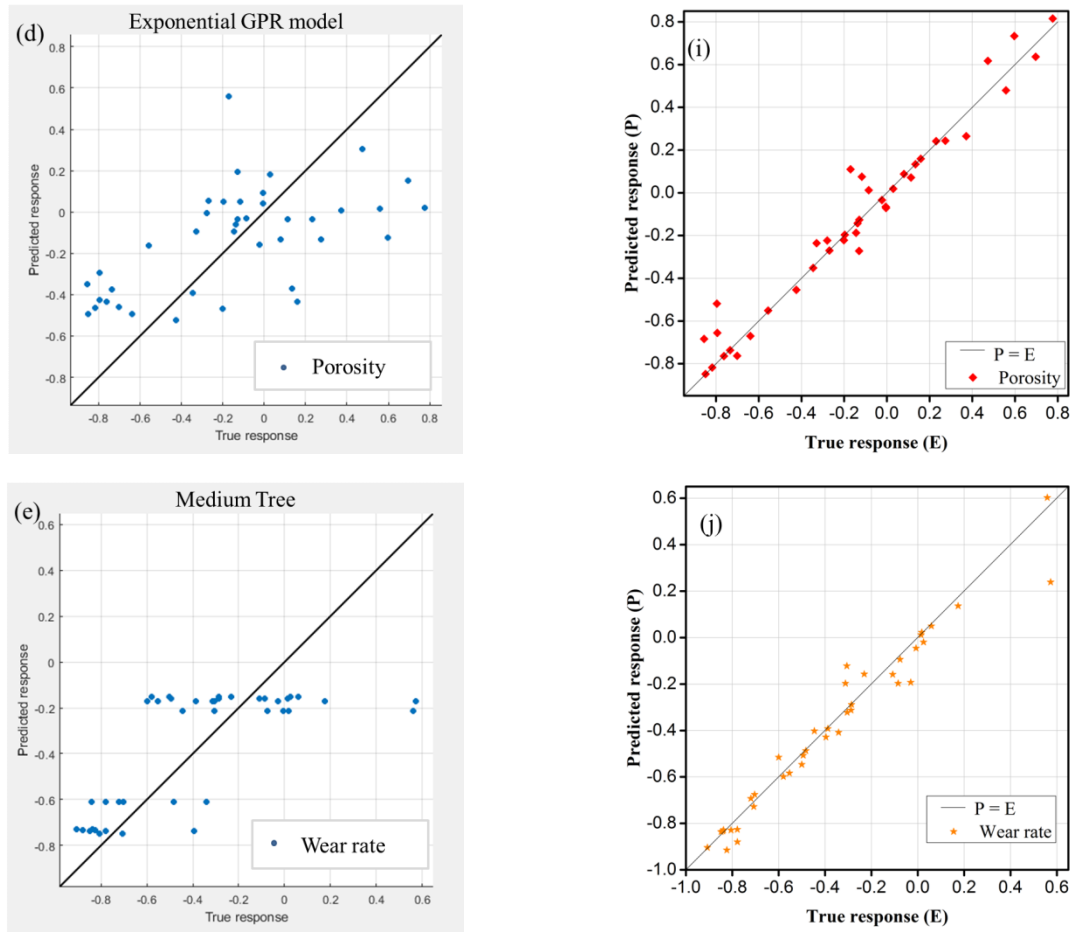


Figure 4.4 The true response vs. predicted response of selected machine learning models (a–e) and ANN models (f–j) for predicting velocity (a, f), temperature (b, g), microhardness (c, h), porosity (d, i), and wear rate (e, j)

4.3. Implementation of ANN1 model for forecasting the behaviors of in-flight particles

For the ANN1 model, three process parameters were selected as inputs: O_2 flow rate ($Q(O_2)$), CH_4 flow rate ($Q(CH_4)$), and SOD. In addition, the temperature and velocity of the in-flight particles (i.e., V_E and T_E) were targets. After normalization, the data was randomly divided according to the data division function of “dividerand”. Then, it was divided into three sets: a training set, a testing set, and a validation set, with the ratio of 70%, 15%, and 15%, respectively. Indicator R is an indication of the relationship between the predicted result and the true result, which has been selected to evaluate the regression performance of the models, as depicted in Eq. (4.3). Usually, the higher the correct evaluation value R, the better the fitting result of the ANN model.

$$R^2 = 1 - \frac{\sum_{i=1}^N (t_i - a_i)^2}{\sum_{i=1}^N (t_i - \bar{t}_i)^2} \tag{Eq. (4.3)}$$

, where t_i is the experimental result, a_i is the predicted result, \bar{t}_i is the average of the experimental result, and N is the number of datasets.

4.3.1. Optimization process for the ANN1 model

As discussed in Section 1.4.3, the MLP neural network, which is characterized with a back-propagation algorithm, has been chosen to analyze, predict, and optimize the HVOF spray process and HVOF-sprayed coatings. The MLP ANN architecture consists of three main parts: the input layer, the output layer, and the layers in between, which are termed hidden layers. A typical architecture of the ANN1 model is shown in Figure 4.5 (a). The transfer function (f) introduces non-linearity into the output of a neuron, as illustrated in Figure 4.5 (b). The transfer functions used need to be optimized, including the function from the input layer to the first hidden layer (TF1), the function between hidden layers (TF2), and the function from the second hidden layer to the output layer (TF3). Furthermore, the learning function, performance function, and the number of neurons in hidden layers should all also be optimized, in order to acquire the most suitable ANN models.

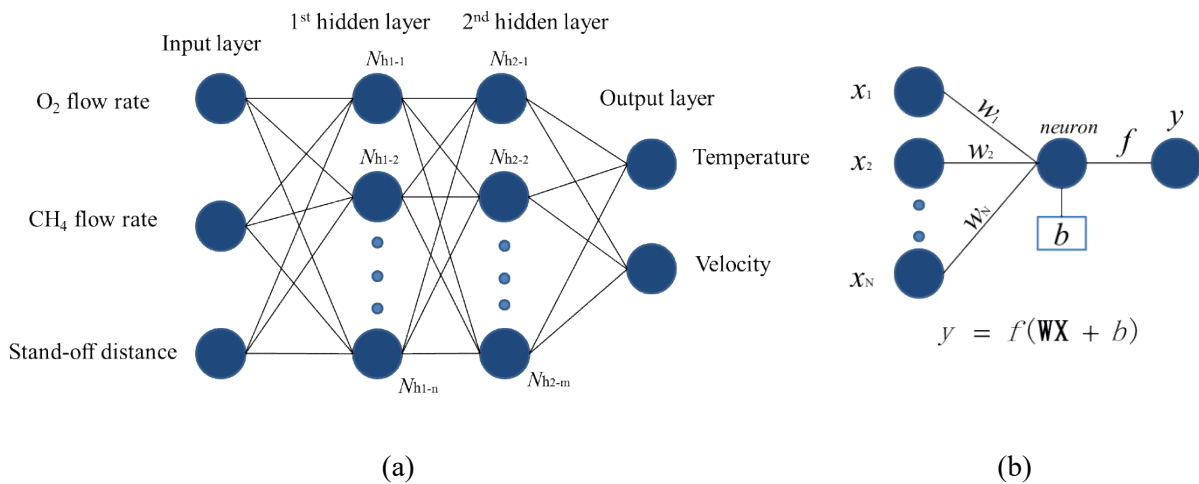


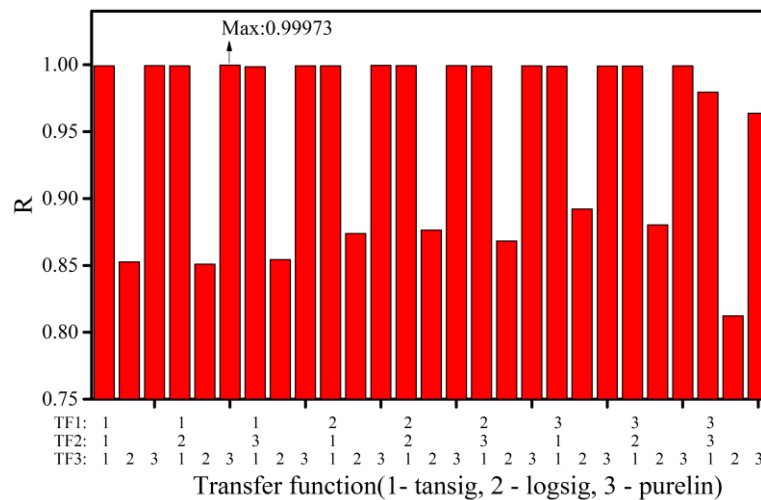
Figure 4.5 A typical architecture of the ANN1 model (a) and its transfer function (b)

Initially, the functions and parameters were set as the default setting for solving regression problems, with the ANN model in MATLAB, as listed in Table 4.2. The optimizations were carried out by varying specific functions or parameters based on the default setting.

Table 4.2 Default setting for functions and parameters for the ANN models

Function and parameter	Value
Transfer functions	tansig (TF1), tansig (TF2), purelin (TF3)
Training function	trainlm
Performance function	mse
Architecture of hidden layers	5 for 1 st and 5 for 2 nd hidden layers

A full factor analysis has been carried out to select the best combination of transfer functions. As shown in Figure 4.6, the models taking “logsig” as the transfer function between hidden layers perform relatively poorly, normally returning an R of less than 0.9. The highest R (0.99973) was obtained with the combination of “tansig” as the transfer function from the input layer to the first hidden layer, “logsig” as the transfer function between the hidden layers, and “purelin” as the transfer function from the second hidden layer to the output layer. Therefore, this combination of transfer functions has been selected for the ANN1 model.

**Figure 4.6** Comparing the performance of the ANN1 model with different combinations of transfer functions

ANN trainings with different training functions have been conducted, the comparison results of which are presented in Figure 4.7. Both of the “trainlm” and “trainbr” training functions exhibit outstanding performance, with an R value of 0.99938 and 0.99974, respectively. These are all updates of weight and bias values, according to the Levenberg-Marquardt optimization. Often, “trainlm” was the fastest back-propagation algorithm in the toolbox. Although this requires more memory than other

algorithms, it is highly recommended as a first-choice supervised algorithm [8]. As a network training function, “trainbr” minimizes a combination of squared errors and weights, and then determines the correct combination, in order to produce a network that generalizes well. This process is called Bayesian regularization. Though the “trainbr” training function performs better than “trainlm” it requires almost 2–3 times more training time. Considering the tiny difference between their performances and the obvious difference in their training time, “trainlm” has been selected for the ANN1 model.

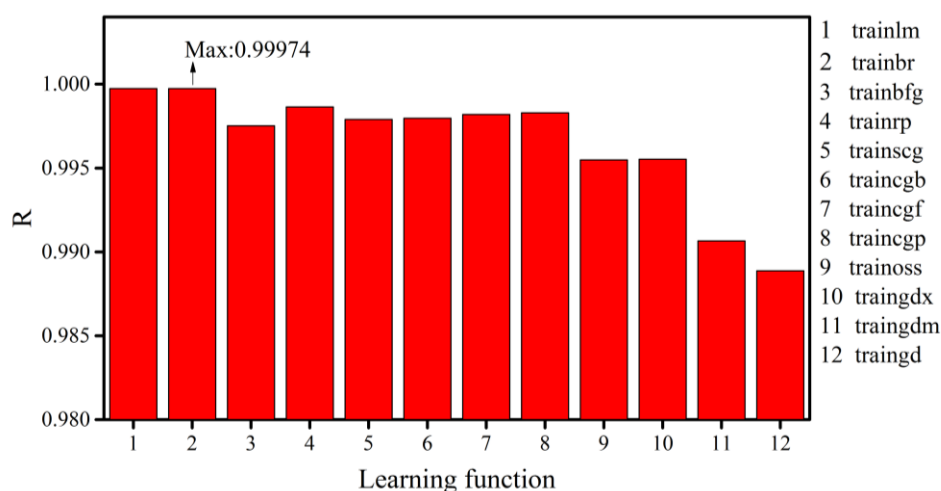


Figure 4.7 Comparing the performance of the ANN1 model with different training functions

Both the “trainlm” and “trainbr” training functions use the Jacobian calculation, which assumes that performance is a mean or sum of squared errors. Therefore, networks trained with these training functions must use either the “mse” or “sse” performance function. To compare the performance of ANN models with different performance functions, the default training function “trainlm” was replaced with “trainrp.” As [Figure 4.8](#) indicates, the performance function has limited influence over the training results. However, it can help to accelerate the calculation convergence. The considered performance functions produce similar results, wherein the “sse” gives relatively higher accuracy in terms of predictions. Furthermore, the “sse” performance function is also accepted for the “trainlm” training function. Accordingly, “sse” has been selected to train the ANN1 model.

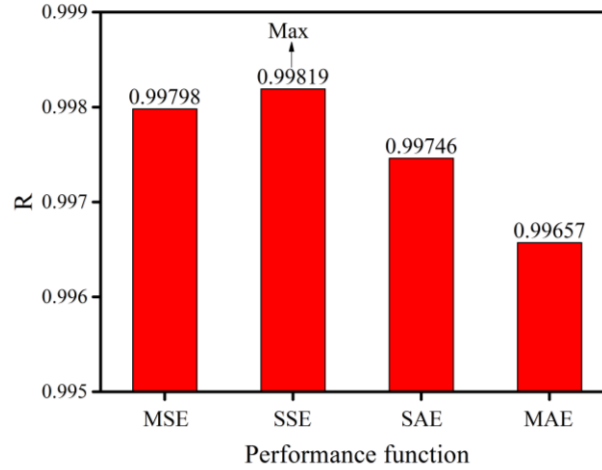


Figure 4.8 Comparing the performance of the ANN1 model with different performance functions

In the ANN model structure, the neuron numbers in both the input and output layers are determined by the number of the network's input and output variables. However, there is no general rule for determining the number of hidden layers and the neuron number in the hidden layer. Generally speaking, the number of hidden layers and the neuron number in the hidden layer are specified by considering the accuracy of the trained model and the complexity of the network structure. Higher accuracy with a lesser number of hidden layers and neurons in the hidden layer are expected. Several researchers have suggested that some formulas relate the neuron number in the hidden layer with the database size [9, 10]. S. Guessasma [11], for instance, suggests that the formula provided in [10] better describes the case with less of the database, which is estimated as explained in the following paragraph.

$$N_H \in \left[\frac{N_P N_S}{N_I + N_S}, \frac{2N_P N_S}{N_I + N_S} \right] \quad \text{Eq. (4.4)}$$

, where N_H is the total neuron number in the hidden layers, N_P is the database size, N_I and N_S are the input and output neuron size.

In the ANN1 model, the suitable neuron number in the hidden layers is estimated to be between 16 and 32. Therefore, 110 sets of training models with 0–10 neurons (with an interval of one neuron) in the first hidden layer and 1–10 in the second hidden layer were trained to optimize the architecture of the ANN1 model, as shown in Figure 4.9. As previously discussed, the optimized functions were applied directly, in order to simplify the training process. To clearly illustrate the predicted results,

pictures with different legends are used. Figure 4.9 (a) illustrates that two hidden layer models with only one neuron in the first or second hidden layer perform worse, particularly when the second hidden layer has one neuron (with an R value of less than 0.99). The simulation results indicate that a combination of six neurons in the first and second hidden layers, respectively, produces a relatively high R value of 0.99991 in the ANN1 model. Considering the relatively high accuracy of the model and the reduced complexity of the network structure, the number of hidden layers and the number of neurons in the hidden layer for the models are therefore selected to be six neurons in both the first and second hidden layer. The neuron number used in the ANN1 model (12 neurons in total) is less than the number estimated, which may have contributed to the regular tendency of the behaviors of the in-flight particles.

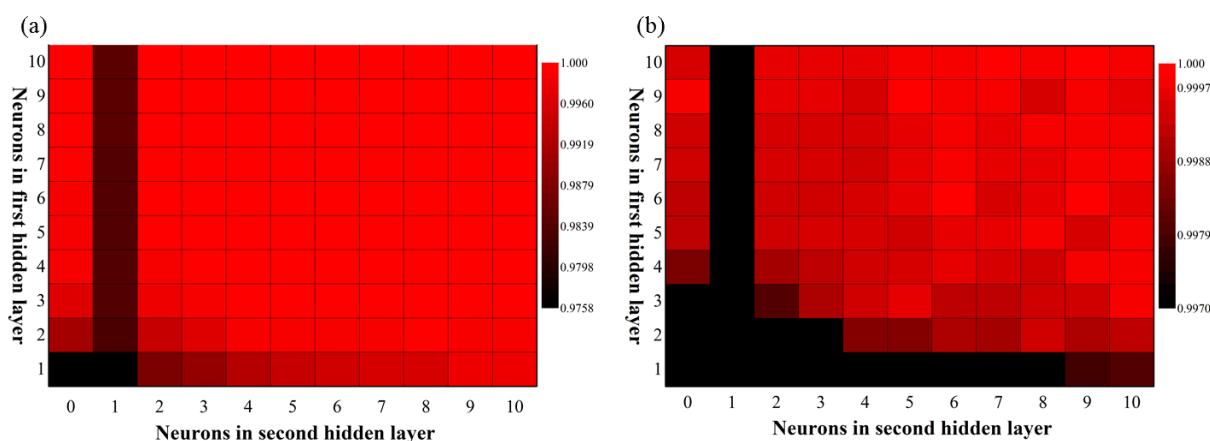


Figure 4.9 Comparing the performance of the ANN1 model with different structures

The functions and parameters, after optimization, are summarized in Table 4.3. The following analysis of the training and testing of the ANN1 model was carried out based on these functions and parameters.

Table 4.3 Optimized functions and parameters for the ANN1 model

Function and parameter	Value
Transfer functions	tansig (TF1), logsig (TF2), purelin (TF3)
Training function	trainlm
Performance function	sse
Architecture of hidden layers	6 for 1 st and 6 for 2 nd hidden layers

4.3.2. Training and testing of the ANN1 model

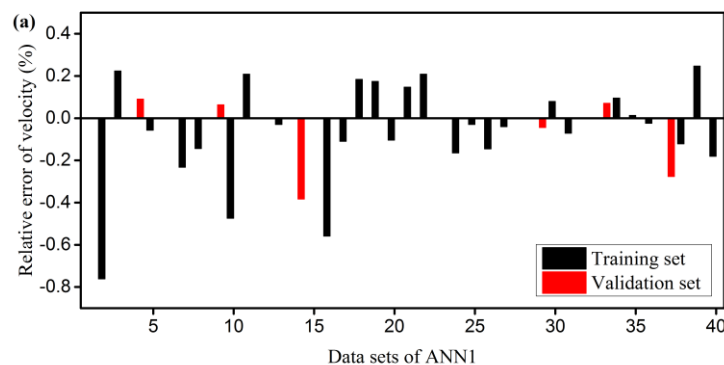
The training process for the ANN1 model was carried out and an R value of 0.99991 was obtained during the optimization process (training and validation) of the ANN1 model, which proves that the model is well trained and that there is a great similarity between the experimental values and predicted values.

The outputs (predicted values) of the training and validation set were inverse normalized after training according to Eq. (4.5).

$$X = 0.5(X_{MAX} - X_{MIN})(X_{NORM} + 1) + X_{MIN} \quad \text{Eq. (4.5)}$$

, where, X is the inverse normalized value; X_{NORM} is the normalized value; X_{MAX} is the maximum of the real value, X_{MIN} is the minimum of the real value.

The comparison between the experimental values and the predicted values of the ANN1 model are displayed in Figure 4.10, where the black and red columns in Figure 4.10 (a) represent the relative errors of the training and validation set for velocity and the black and orange columns in Figure 4.10 (b) represent temperature. The relative errors between the experimental values and the predicted values have been calculated with respect to the experimental values. The relative error between the experimental and predicted values of the velocity of the in-flight particles varies from -0.76% to 0.25%, with an average of -0.063%, as indicated in Figure 4.10 (a). The distribution of the velocity of the in-flight particles is larger and more scattered than that of the temperature of the in-flight particles, from -0.24% to 0.43%, with an average of 0.015% (Figure 4.10 (b)). This indicates that the ANN1 model is more accurate in terms of predicting the temperature of the in-flight particles, which is mainly attributed to the more regular tendency of the temperature of the in-flight particles.



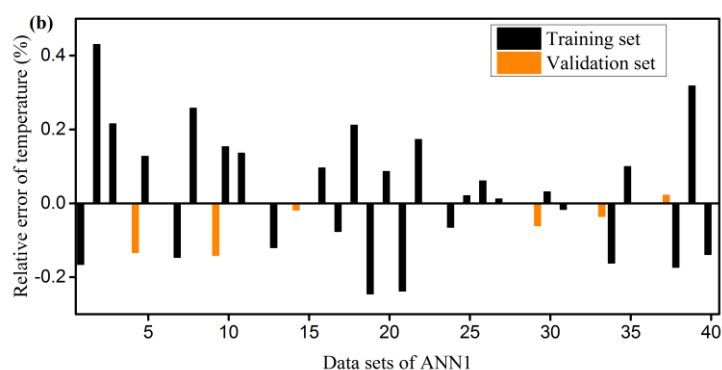


Figure 4.10 Relative error of velocity (a) and temperature (b) between experimental and predicted results, with respect to the experimental results

The reliability of the ANN1 model has been verified by the performance of the test set, which is independent from the training and optimization process of the ANN model. The test set, which is composed of data from Sets 6, 12, 15, 23, 28, and 32, has been randomly allocated from the dataset.

As shown in Figure 4.11, the maximum of the absolute relative errors for the velocity and temperature are 0.43% and 0.14%, which correspond to a difference of 3 K and 2 m/s. Additionally, the minimum is 0.08% and 0.01% for velocity and temperature. This indicates that the predicted values are consistent with the experimental values, which suggests that the ANN1 model has been properly trained to predict the temperature and velocity of in-flight particles from the HVOF spray process parameters.

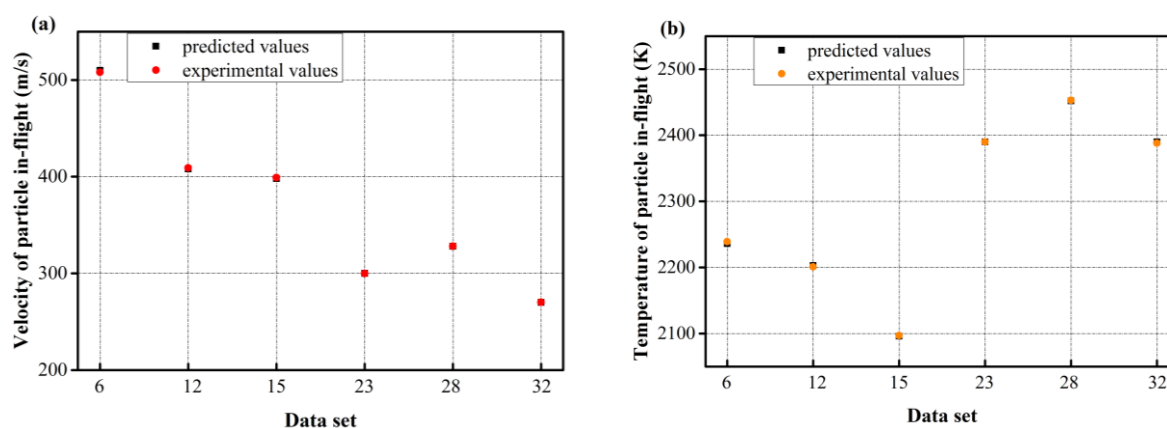


Figure 4.11 Comparison of the experimental and predicted values of velocity (a) and temperature (b), for the test set in the ANN1 model

4.4. Implementation of the ANN2 model for predicting coatings' properties

For the ANN2 model, the temperature and velocity of the in-flight particles (i.e., V_E and T_E) were selected as the inputs and three coating properties (microhardness, porosity, and wear rate) were chosen as targets, as depicted in Figure 4.12. Similar to the procedure outlined in Section 4.3, the data has been normalized and randomly divided into three sets: a training set, a validation set, and a test set, with ratios of 70%, 15%, and 15%, respectively. R was continuously selected as the indicator to evaluate the performance of the model. A similar optimization and training process of the ANN model are given as follows. The model was optimized by varying specific functions or parameters, based on the default settings that are listed in Table 4.1.

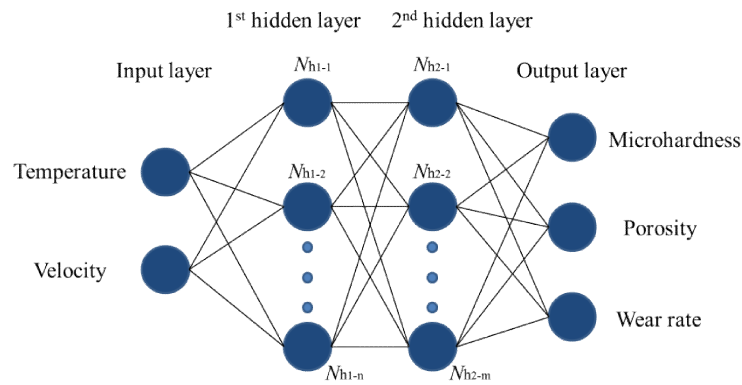


Figure 4.12 A typical architecture of the ANN2 model

4.4.1. Optimization process for the ANN2 model

A full factor analysis has been carried out to select the best combination of transfer functions. As shown in Figure 4.13, the R value varies from 0.54 to 0.94. Models with “logsig” as the transfer function from the first hidden layer to the second hidden layer always performed worse than other combinations, returning an R of less than 0.75. Models with “tansig” as the transfer function from the input layer to the first hidden layer exhibited better performance than others. The maximum R value (0.93695) was obtained with “tansig” as the transfer function from the input layer to the first hidden layer, as the transfer function between the hidden layers, and also as the transfer layer from the second hidden layer to the output layer. Therefore, this combination of transfer functions has been employed in the ANN2 model.

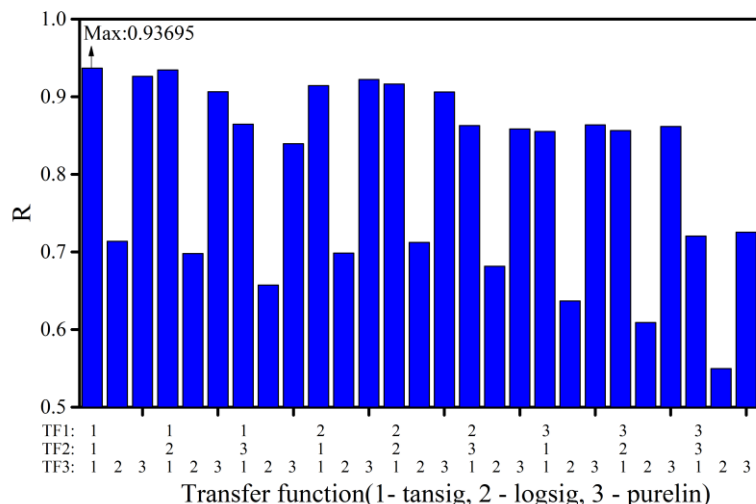


Figure 4.13 Comparing the performance of the ANN2 model with different combinations of transfer functions

The model with different training functions was trained and the results are displayed in Figure 4.14. This indicates that the R value for different training functions concentrates in the range of 0.8–0.93. It is evident that “trainlm” performed better than the other training functions, with an R value of 0.92612, while the others all obtained an R value of less than 0.9. Therefore, “trainlm” has been chosen as the training function for the ANN2 model.

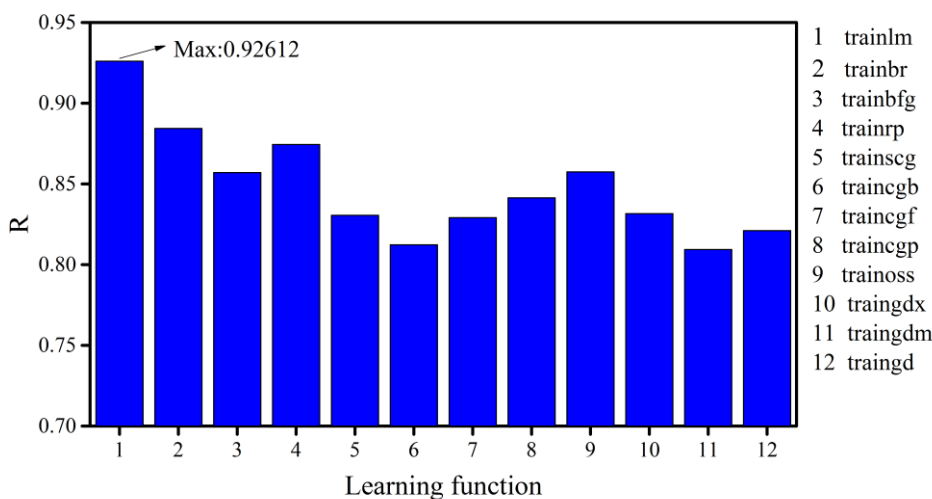


Figure 4.14 Comparing the performance of the ANN2 model with different training functions

To compare the performance of the ANN2 model with different performance functions, the default training function “trainlm” was replaced with “trainrp.” As depicted in Figure 4.15, the R value varies from 0.8462 to 0.86947, which reinforces that the performance function has limited

influence over the training results. Both “mse” and “sse” are relatively more accurate than the others. They were also accepted for the “trainlm” training function. Accordingly, “mse” was selected to train the ANN2 model.

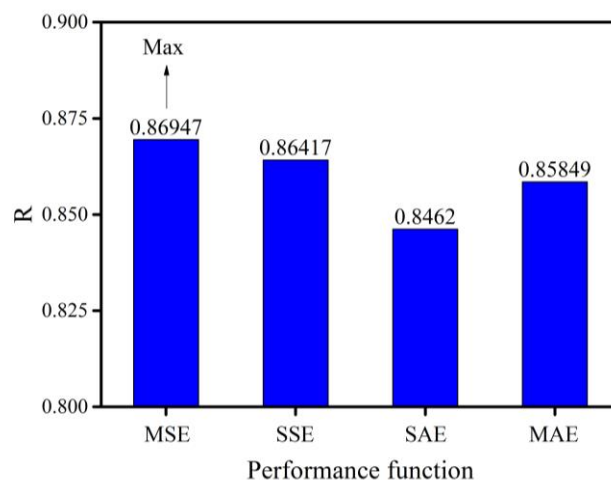


Figure 4.15 Comparing the performance of the ANN2 model with different performance functions

The optimized functions were applied directly to simplify the training process. According to the Eq(4.3), the suitable neuron number in the hidden layers is estimated to be between 24 and 48. Therefore, 110 sets of training models with 0–20 neurons (with an interval of two neurons) in the first hidden layer and 2–20 neurons in the second hidden layer were trained, as shown in Figure 4.16. The R value varies from 0.790 to 0.999. Pictures with different legends are used to clearly display the evolution of the R value, based on different combinations of hidden layers. As displayed in Figure 4.16 (a), models with only one hidden layer performed worse (with an R value of less than 0.9). For models with two hidden layers, the prediction accuracy increased as the number of neurons in the hidden layers increased (which can be seen in Figure 4.16 (a)). Models with less neurons in the hidden layers exhibited lower R values (which is illustrated in Figure 4.16 (a)–(b)). However, when the neuron number is higher than 10, the R value fluctuates and increases more slowly, as indicated in Figure 4.16 (b).

The simulation results indicate that a combination of 14 neurons in the first hidden layer and 20 neurons in the second hidden layer produces a relatively high R value of 0.99997 in the ANN2 model. Considering the relatively high accuracy of the model and the reduced complexity of the network structure, the number of hidden layers and the number of neurons in the hidden layer, for the models,

are determined as 14 neurons in the first hidden layer and 20 neurons in the second hidden layer.

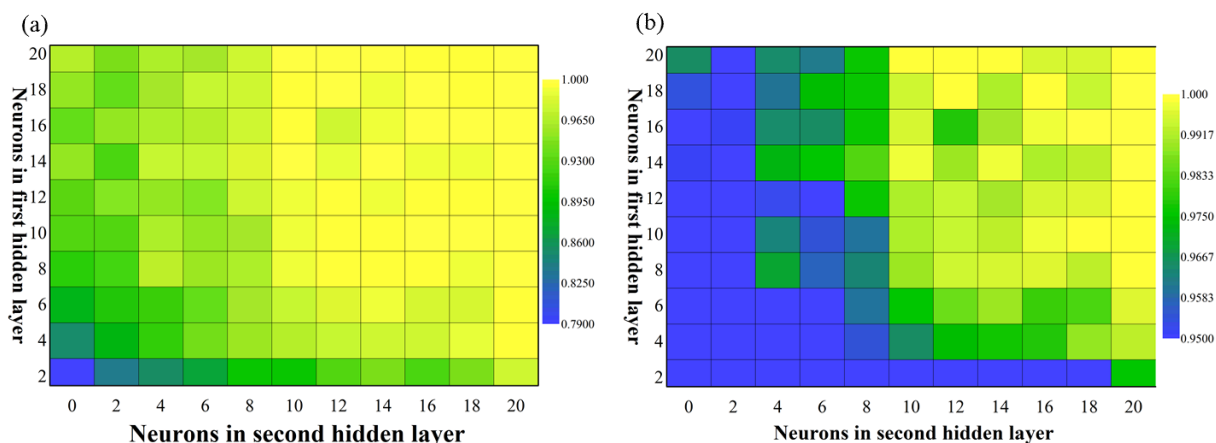


Figure 4.16 Comparing the performance of the ANN2 model with different structure

This suggests that the R value in the ANN2 model is generally smaller than that of the ANN1 model, even though the neuron number is higher than in the ANN1 model. This can be ascribed to the more complex relationship between the behaviors of the in-flight particles and the coating properties. The functions and parameters, after optimization, are summarized in Table 4.4. The following analysis of the training and testing of the ANN2 model was carried out, based on these functions and parameters.

Table 4.4. Optimized functions and parameters for the ANN2 model

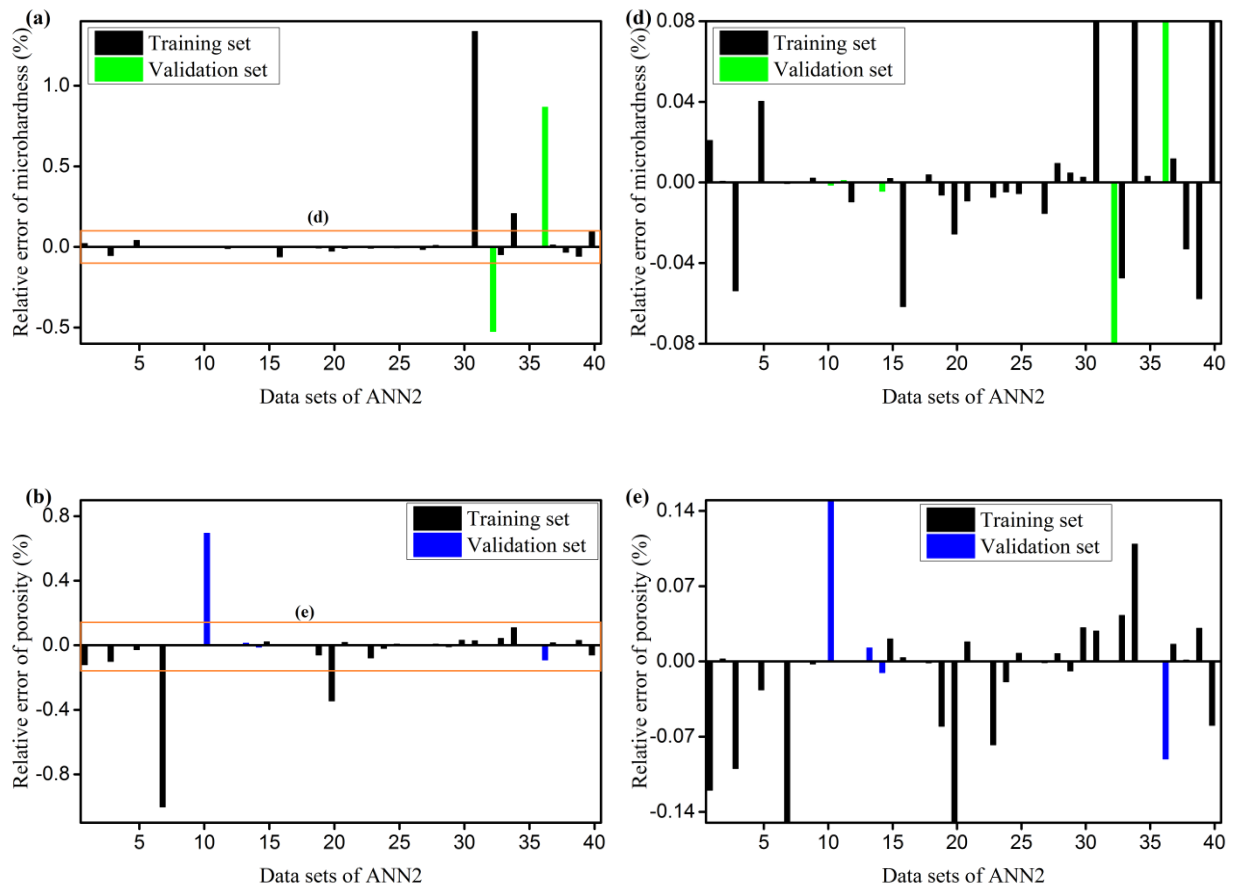
Function and parameter	Value
Transfer functions	tansig (TF1), tansig (TF2), tansig (TF3)
Training function	trainlm
Performance function	mse
Architecture of hidden layers	14 for 1 st and 20 for 2 nd hidden layers

4.4.2. Training and testing of the ANN2 model

The training process for the ANN2 model has been implemented with an R value of 0.99997, during the optimization process (training and validation). This confirms that the model is well trained and that there is a considerable similarity between the experimental values and predicted values. The dataset No. 10, 11, 13, 14, 32, and 36 have been automatically allocated as the validation set, and dataset of No. 4, 6, 7, 17, 22, and 26 were selected as the test set in the ANN2 model. The remaining

dataset constitutes the training set.

The targets and outputs of the training and validation set were inverse normalized after training. A comparison between the experimental values and the predicted values of the ANN2 model is displayed in Figure 4.17, where the black and green columns in Figure 4.17 (a) represent the relative errors of the training and validation sets for microhardness, the black and blue columns in Figure 4.17 (b) represent porosity, and the black and violet columns in Figure 4.17 (c) represent wear rate. To investigate further, the local regions have been amplified, as shown in Figure 4.17 (d)–(f). The relative error between the experimental and predicted values of coatings' microhardness varies from -0.52% to 1.34% with an average of 0.05%, as indicated in Figure 4.17 (a). Coatings' porosity is distributed from -1.00% to 0.69%, with an average of -0.02% (Figure 4.17 (b)) and wear rate is distributed from -1.55% to 3.15%, with an average of 0.09%. The wear rate distribution is larger and more scattered than that of the coating's microhardness or porosity, which indicates that the ANN2 model is more accurate in terms of predicting the coating's microhardness and porosity.



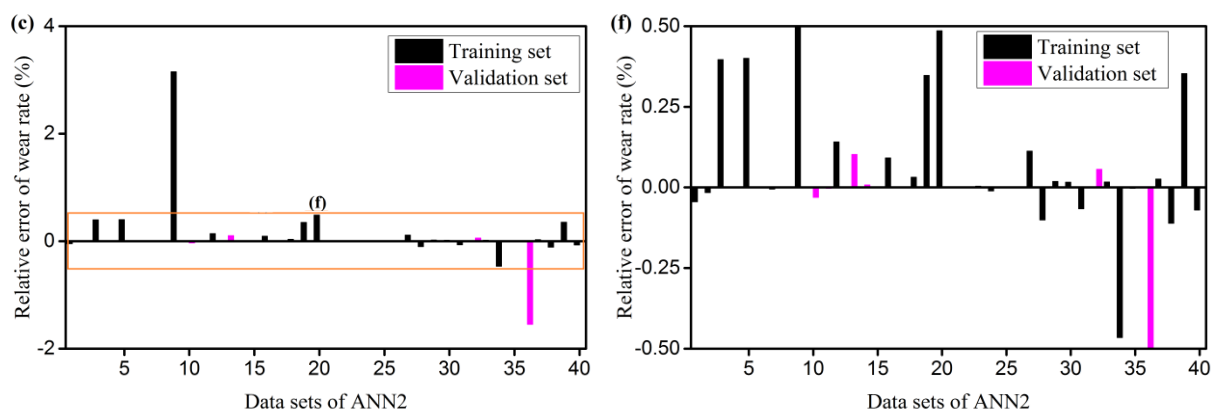
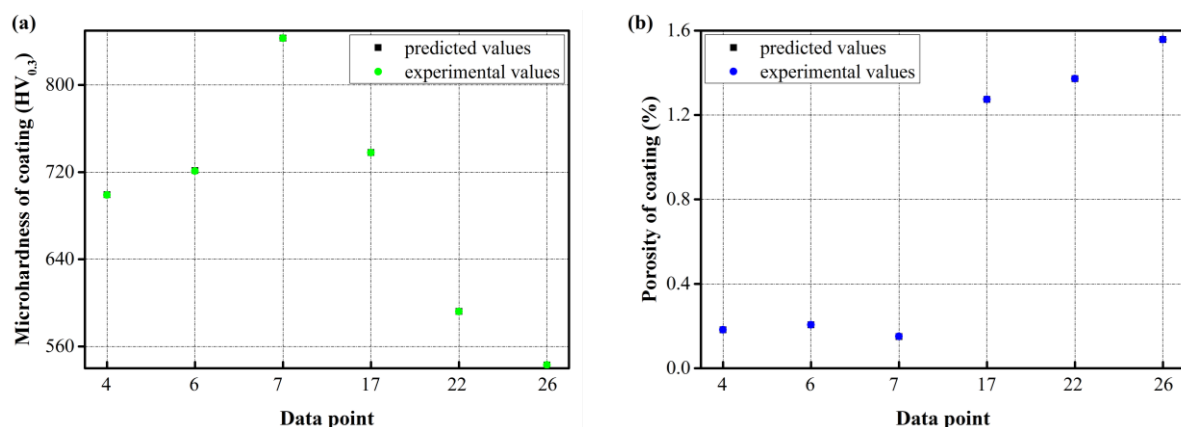


Figure 4.17 Relative error of microhardness (a, d), porosity (b, e), and wear rate (c, f), between the experimental and predicted results, with respect to the experimental results

The reliability of the ANN2 model has been verified by the performance of the test set, as shown in Figure 4.18. This indicates that the predicted values almost all cover the experimental values (black points). The maximum of the absolute relative errors are 0.06%, 0.15%, and 0.31%, which correspond to a difference of 0.41 HV_{0.3}, 0.0003%, and 0.009×10⁻⁵ mm³/N/m. This demonstrates that the predicted values are consistent with the experimental values and that the relative errors of the test set is within that of the training set and the validation set, which suggests that the ANN2 model has been properly trained to predict the coating properties according to the temperature and velocity of the in-flight particles. Although the relationships between the characteristics of the in-flight particles and the coating properties are complex, it is possible to directly predict the coating properties according to the input of the characteristics of in-flight particles, by employing the ANN2 model.



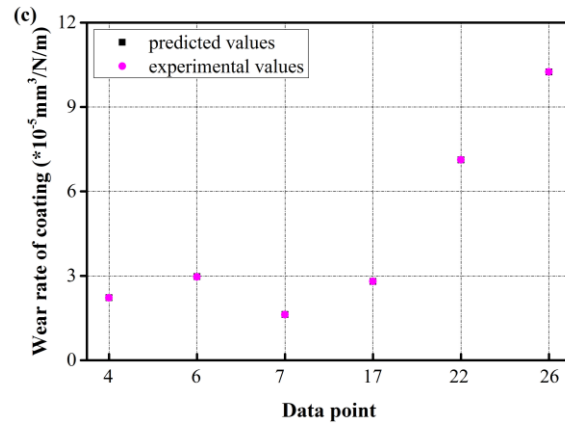


Figure 4.18 Comparison of the experimental and predicted values of microhardness (a), porosity (b), and wear rate (c), for the test set in the ANN2 model

4.5. MIV analysis in the ANN models

The MIV-based analysis method has been widely accepted as one of the evaluators of the value of a given coefficient for an ANN model [12-14]. The MIV value and contribution rate for each input variable on each output variable of both the ANN1 and ANN2 models are calculated and shown in Table 4.5 and Figure 4.19.

MIV analysis on the ANN1 model reveals that the important sequence of the factors for the velocity of in-flight particles is SOD > O₂ flow rate > CH₄ flow rate, and for the temperature of in-flight particle is SOD > CH₄ flow rate > O₂ flow rate. The SOD always exhibits the greatest influence over both velocity and temperature of the in-flight particles, which occupies 70% and 36% of the contribution rate, respectively. The impact of the CH₄ flow rate on velocity is limited, which corresponds to the irregular trend of velocity with regard to the CH₄ flow rate. This is depicted in Figure 3.8 and discussed in Section 3.2.2. In addition, the stand-off distance has a predominant effect on velocity, while the influence of the inputs on temperature is quite uniform, taking 36%, 29%, and 35% for SOD, Q(O₂), and Q(CH₄), respectively. This result is consistent with the analysis of the behaviors of in-flight particles that is presented in Section 3.2.

As displayed in Figure 4.19 (c)–(e), MIV analysis of the ANN2 model indicates that the velocity of in-flight particles represents a greater influence over coatings' microhardness, taking 72%. However, the temperature of the in-flight particles is more important for coatings' porosity and wear

rate, occupying 79% and 82%, respectively. Although the temperature possesses a similar weight in terms of both porosity and wear rate, it is impossible to directly relate coatings' porosity with wear rate. In addition, based on the MIV analysis, it is useful to tune the velocity for better coating microhardness. Conversely, in order to obtain better performance for coatings' porosity and wear rate, adjusting the temperature of the in-flight particles is highly recommended.

Table 4.5 MIV values for input variables

Inputs (ANN1)	Outputs (ANN1)		Inputs (ANN2)	Outputs (ANN2)		
	v	T		MH	PO	WR
SOD	-0.404	0.071	v	0.290	-0.203	-0.088
Q(O ₂)	0.161	0.058	T	-0.320	0.028	0.245
Q(CH ₄)	-0.013	-0.068				

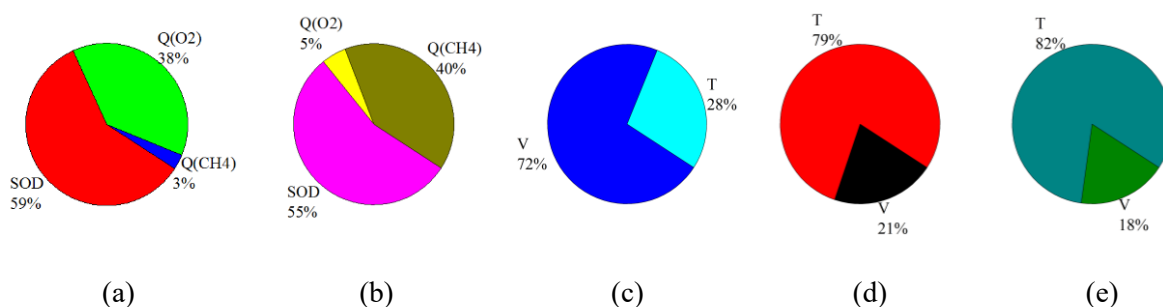


Figure 4.19 The contribution rate of input variables on the velocity (a) and temperature (b) of in-flight particles, as well as coating microhardness (c), porosity (d), and wear rate (e)

Previous works have also concluded that the spray distance performs greater influence over the microhardness and porosity of coatings than the oxygen flow rate for different kinds of feedstock, despite the fuel in the HVOF spray being different to that used in this study [4, 15, 16]. This indirectly confirms the importance of SOD on the behaviors of in-flight particles. Research [17] also suggests that the oxygen flow rate has a complex impact on coatings' wear performance. From one perspective, increased oxygen flow rate increases the velocity of in-flight particles and enhances their cooling effect, which results in the decreased temperature of in-flight particles and the coating's decreased wear resistance. Conversely, increasing the oxygen flow rate contributes to the increase in the

temperature of the in-flight particles, due to an increase in the reaction rate of the gases. Unfortunately, only limited research directly compares the importance of these process parameters. In this work, the MIV-based analysis is used to study the importance of these process parameters, particularly in terms of the ANN model.

4.6. Conclusions

In this chapter, two ANN models were developed and then optimized to predict the properties of HVOF sprayed NiCr-Cr₃C₂ coatings, and to analyze the influence of operating parameters, considering the intermediate process.

The ANN1 model has been trained to predict the relationship between HVOF process parameters (i.e., SOD, CH₄ flow rate, and O₂ flow rate) and the characteristics of in-flight particles (temperature and velocity), with a maximum relative error of 0.76% for velocity and 0.43% for temperature. The prediction of the properties of the coating (i.e., microhardness, porosity, and wear rate) according to the characteristics of in-flight particles has been performed by the ANN2 model, within a relative error of 1.34%, 1.00%, and 3.15% for microhardness, porosity, and wear rate of the coating, respectively. The reliability and accuracy of both the ANN1 and ANN2 models have been further verified by their test sets, where the relative errors (0.43% for velocity, 0.14% for temperature, 0.06% for microhardness, 0.15% for porosity, and 0.31% for wear rate) were smaller than the maximum errors.

The MIV-based analysis has been carried out to evaluate the factors' importance. The results indicate that the important sequence of the factors for the velocity of the in-flight particles is SOD > O₂ flow rate > CH₄ flow rate, for the temperature is SOD > CH₄ flow rate > O₂ flow rate, for the coating's microhardness is V > T, and for the coating's porosity and wear rate is T > V.

Overall, the two developed implicit models can be used to predict coatings' properties and in-flight particles' characters, as well as to optimize coatings. In addition, the MIV-based analysis explores the importance of the process parameters, particularly for the ANN model. These well-trained ANN models will be programmed and integrated into the HVOF spray control system, in order to create an intelligent control system. This novel ANN approach will also be promoted for other thermal spray techniques, which will result in better controls for coating performances.

Reference of chapter 4

- [1] D. Zissis, E.K. Xidias, D.J.A.S.C. Lekkas, A cloud based architecture capable of perceiving and predicting multiple vessel behaviour, 35 (2015) 652-661.
- [2] T. Choudhury, N. Hosseinzadeh, C.J.S. Berndt, C. Technology, Artificial Neural Network application for predicting in-flight particle characteristics of an atmospheric plasma spray process, 205 (2011) 4886-4895.
- [3] G.-C. Ji, C.-J. Li, Y.-Y. Wang, W.-Y.J.S. Li, C. Technology, Microstructural characterization and abrasive wear performance of HVOF sprayed Cr₃C₂-NiCr coating, 200 (2006) 6749-6757.
- [4] A.S. Praveen, J. Sarangan, S. Suresh, B.J.C.I. Channabasappa, Optimization and erosion wear response of NiCrSiB/WC-Co HVOF coating using Taguchi method, 42 (2016) 1094-1104.
- [5] J. Guilemany, J. Miguel, S. Vizcaino, C. Lorenzana, J. Delgado, J.J.S. Sanchez, C. Technology, Role of heat treatments in the improvement of the sliding wear properties of Cr₃C₂-NiCr coatings, 157 (2002) 207-213.
- [6] Machine learning, in, https://en.wikipedia.org/wiki/Machine_learning.
- [7] S.D. Veiga, A. Marrel, Gaussian process regression with linear inequality constraints, Reliability Engineering & System Safety, (2019) 106732.
- [8] I. The MathWorks, trainlm, in, <https://uk.mathworks.com/help/deeplearning/ref/trainlm.html>, 1994-2020.
- [9] L.G. Valiant, A theory of the learnable, in: Proceedings of the sixteenth annual ACM symposium on Theory of computing, ACM, 1984, pp. 436-445.
- [10] G. Brightwell, C. Kenyon, H. Paugam-Moisy, Multilayer neural networks: one or two hidden layers?, in: Advances in Neural Information Processing Systems, 1997, pp. 148-154.
- [11] S. Guessasma, Z. Salhi, G. Montavon, P. Gougeon, C.J.M.S. Coddet, E. B, Artificial intelligence implementation in the APS process diagnostic, 110 (2004) 285-295.
- [12] J.L. Jiang, X. Su, H. Zhang, X.H. Zhang, Y.J.J.C.b. Yuan, d. design, A novel approach to active compounds identification based on support vector regression model and mean impact value, 81 (2013) 650-657.
- [13] Y.-R. Zeng, Y. Zeng, B. Choi, L.J.E. Wang, Multifactor-influenced energy consumption forecasting using enhanced back-propagation neural network, 127 (2017) 381-396.
- [14] M. Qi, Z. Fu, F.J.A.T.E. Chen, Research on a feature selection method based on median impact value for modeling in thermal power plants, 94 (2016) 472-477.
- [15] Q. Wang, Z. Chen, L. Li, G.J.S. Yang, C. Technology, The parameters optimization and abrasion wear mechanism of liquid fuel HVOF sprayed bimodal WC-12Co coating, 206 (2012) 2233-2241.
- [16] W. Tillmann, E. Vogli, I. Baumann, G. Kopp, C.J.J.o.t.s.t. Weihs, Desirability-based

multi-criteria optimization of HVOF spray experiments to manufacture fine structured wear-resistant 75Cr 3 C 2-25 (NiCr20) coatings, 19 (2010) 392-408.

[17] C.-J. Li, G.-C. Ji, Y.-Y. Wang, K.J.T.S.F. Sonoya, Dominant effect of carbide rebounding on the carbon loss during high velocity oxy-fuel spraying of Cr₃C₂-NiCr, 419 (2002) 137-143.

Chapter 5. The development of the HVOF control system and the integration of ANN models

Introduction

In this chapter, the procedure to develop the HVOF spray control system and its interface will be introduced; this will be done using coding with the International Electrotechnical Commission (IEC) 61131-3 language in the Automation Studio™. The two packaged networks obtained in [Chapter 4](#) will then be integrated into the developed control system to realize an intelligent HVOF spray control system.

5.1. Development of the control system

5.1.1. The principle of the HVOF spray control system

The recompiled control system has been developed and programmed using the PLC. Two sets of systems for controlling the CDS and Diamond-Jet 2701/2702 torches have been developed and integrated using the same controller. The systems need to control the gases supply system, powder feeder, ventilation system, and cooling system, as displayed in [Figure 5.1](#). The detailed principle is provided below.

Although the torch and gases used for the CDS spray and Diamond-Jet spray systems are different, the main workflow is similar, as shown in [Figure 5.2](#). The system will remain on “Stand by” until the “Start” button is pressed. The pre-defined parameters and spraying environment (e.g., cooling water and air compressor) will then be checked. If all of the conditions are satisfactory, the gases are opened and ignition is attempted. If the conditions are not satisfactory, the system returns to “Stand by” for modification. If the ignition is successful within 20 s, the system will move into the “Transition” stage, in which the gases flow rate will gradually increase until it reaches the pre-defined values. If it does not succeed, it will move to the “Purge” step and, finally, return to the “Stand by” state. When the pre-defined values are reached and the environment condition is stable, the system is ready for spraying. After pressing the “Stop” button, the powder feeder is stopped immediately and the gases are decreased gradually. When the gas flow rates drop to a certain value, the flame goes out and the system moves to the “Purge” step to push out the remaining gases in the supply pipe, then returns to “Stand by” for the next cycle. “Rapid stop” and “Emergency stop” buttons are provided to

correspond with different urgent situations.

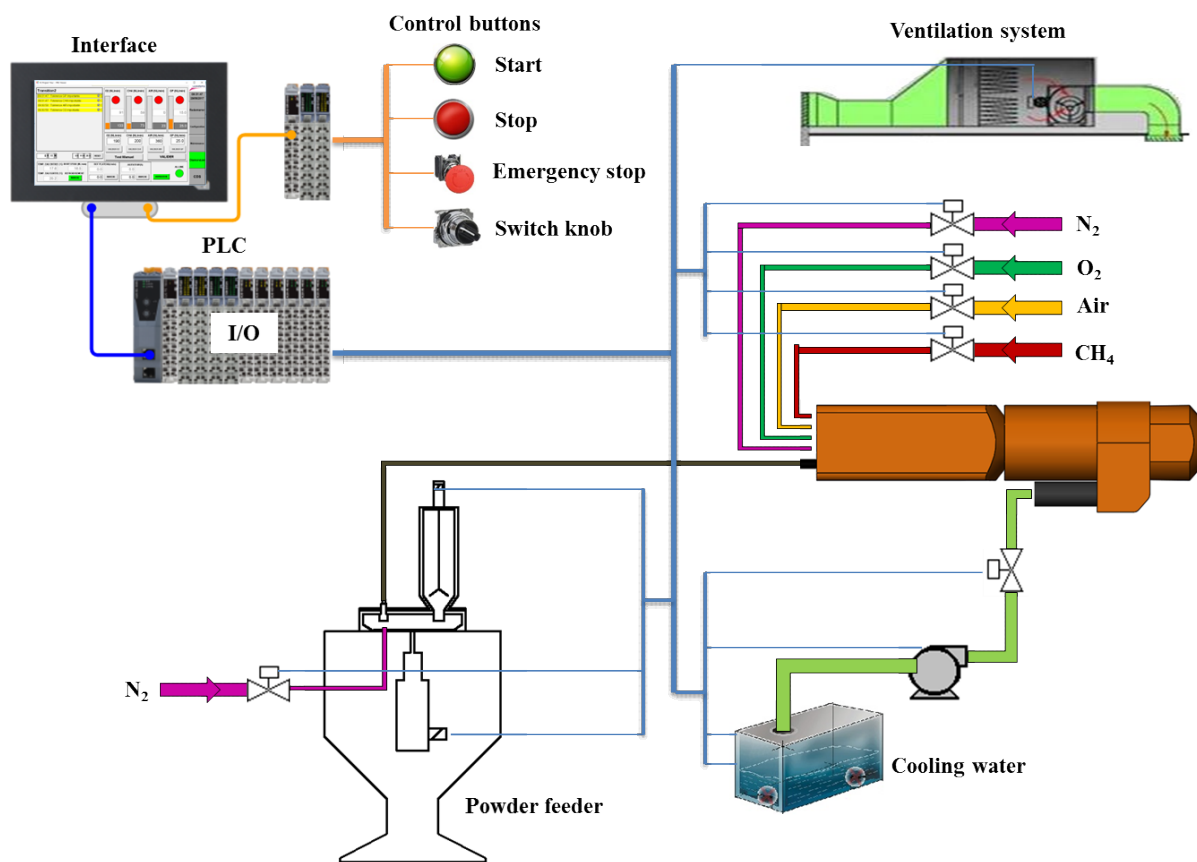


Figure 5.1 System architecture diagram of the HVOF spray control system

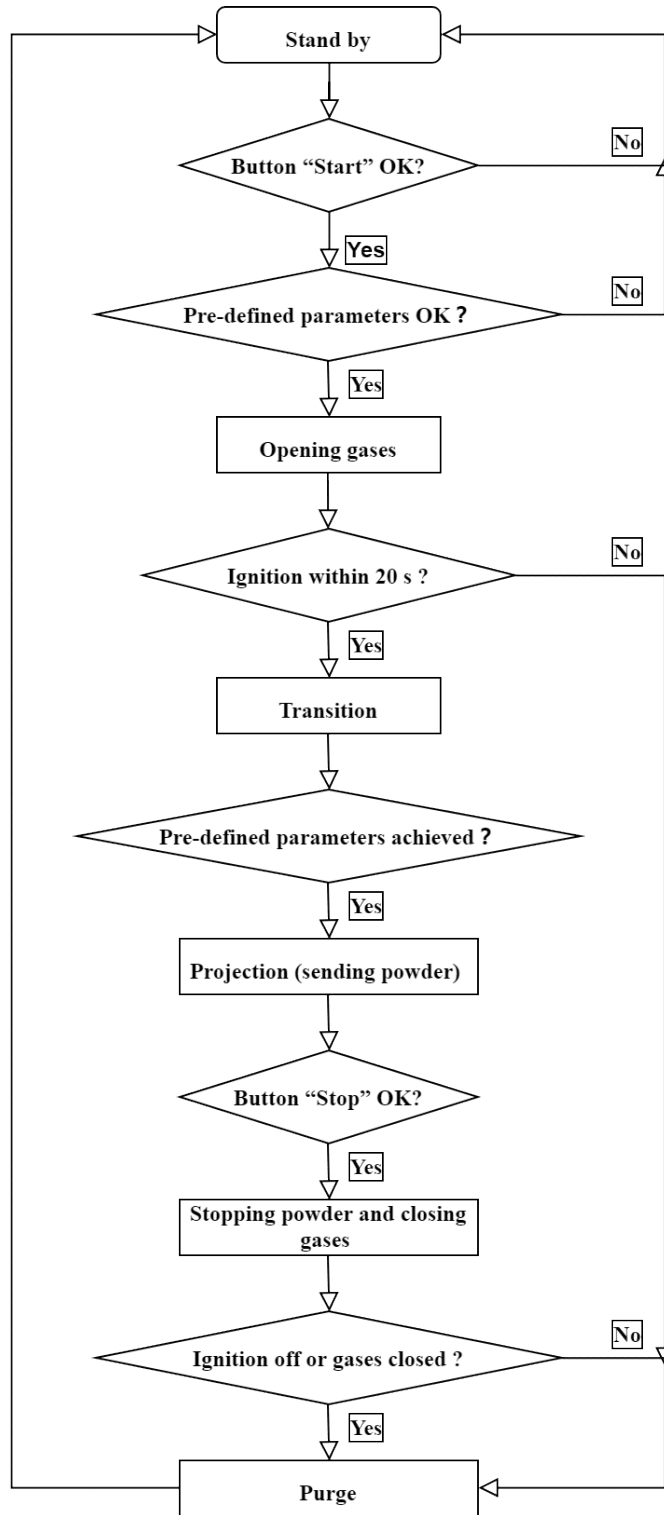


Figure 5.2 Workflow of the HVOF spray control system

5.1.2. The hardware of the HVOF spray control system

The hardware architecture of the HVOF control system is illustrated in Figure 5.3. Power panel (1) provides a display and touch screen, which integrates with a central processing unit (CPU) and

memory. The extended input/output (I/O) module includes a bus receiver (2), which is equipped with a multiplexer for the X2X Link as well as the internal I/O supply and is used to connect the X20 System to the X2X Link. Digital input/output modules (3, 8/4, 7) are used to input/output digital data. The remote I/O module uses a field bus controller (5) to connect X2X Link I/O nodes to the local field bus POWERLINK; it also makes it possible to operate the X2X Link cycle synchronously or asynchronously to POWERLINK using a prescaler. The supply module (6) is used together with an X20 bus controller, which is equipped with a feed for the bus controller, the X2X Link, and the internal I/O supply. Analog input/output modules (9/10) are employed to input/output analog signals. The control system is executed based on the hardware.

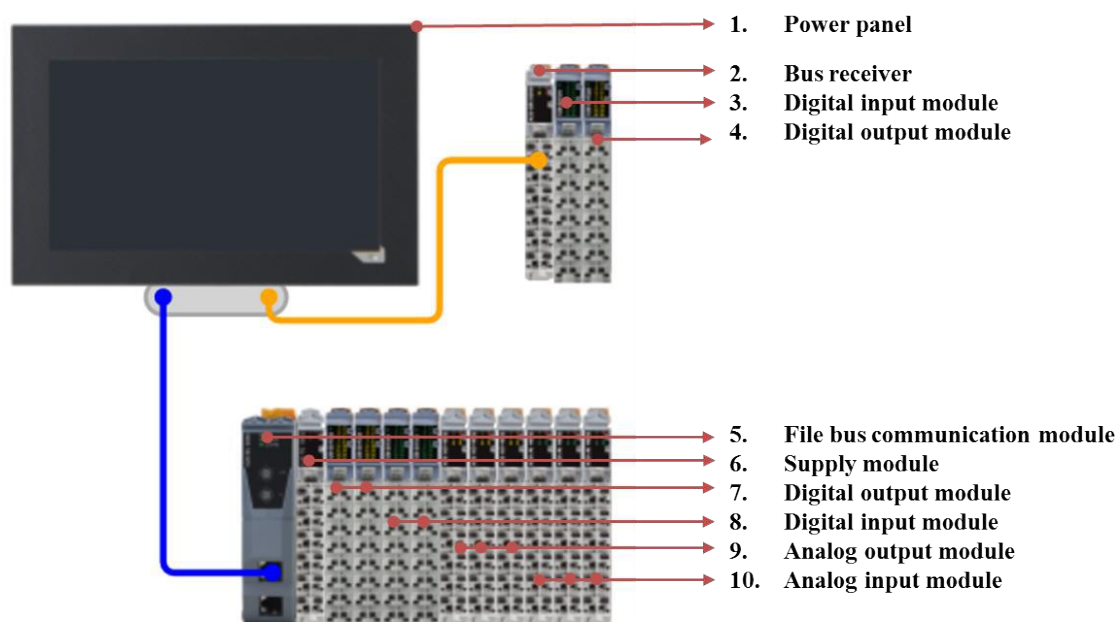


Figure 5.3 Hardware of the HVOF spray control system

5.1.3. The programming language of the HVOF spray control system

The PLC has been used to control the HVOF spray system. A PLC or programmable controller is an industrial digital device that monitors computer processes by viewing inputs to a system and turning the outputs on or off, based on a set of instructions programmed using PLC languages [1, 2]. It has been widely employed for controlling manufacturing processes or activities that require high reliability control and ease of programming and process fault diagnosis [1].

PLC programs are typically written in a special application on a personal computer and then downloaded to the PLC using a direct-connection cable or over a network. Various PLC programming

languages are provided in Automation Studio™. Our system has been programmed under the IEC 61131-3 standard, in which PLCs can be programmed using standards-based programming languages [1]. IEC 61131-3 is the third part (of 10) of the open international standard IEC 61131 for PLC, which deals with basic software architecture and programming languages of the control program within PLC [3]. It provides two textual and three graphical programming language standards:

- 1) Ladder diagram (LD), which is also known as ladder logic, is a graphical language that normally represents a program using a graphical diagram based on the circuit diagrams of relay logic hardware [4]. It is one of the most popular types of PLC programming languages attributing to its advantages of being intuitive, having good debugging tools, and its good representation for discrete logic [2].
- 2) Function block diagram (FBD), which drives data from inputs to outputs by sending them through blocks of nested data [2], is a graphical language that can describe the function between input and output variables. It allows programmers to view the system being programmed in terms of the flow of signals between the elements being processed [2].
- 3) Sequential function chart (SFC), which is defined as preparation of function charts for control systems, can be used to program processes that can be broken down into steps [5]. It is a graphical language that allows the programmer to enter code in chronological order. Its visualization of what and when it is happening in the procedure of the code makes it easy to understand [2].
- 4) Structured text (ST/STX), which is entirely text-based PLC language, is a high-level language that is block structured and syntactically resembles programming languages such as Basic and Pascal [2]. It supports complex statements and nested instructions, such as iteration loops (REPEAT-UNTIL; WHILE-DO), conditional execution (IF-THEN-ELSE; CASE), and functions (SQRT(), SIN()) [6].
- 5) Instruction list (IL) is one of the five languages supported by the initial versions of the IEC 61131-3 standard, and is subsequently deprecated in the third edition [7]. Because of this, it will not be introduced any more in this work.

As introduced in [Section 5.1.1](#), the control system works through the whole procedure by

changing from one state to another in response to external inputs and/or if a condition is satisfied. This is a typical finite-state machine (FSM), which is a mathematical model of computation. The change from one state to another in FSM is defined as a transition. An FSM is defined by a list of its states, its initial state, and the conditions for each transition [8]. The instruction “CASE... OF...” in ST language can easily realize state change in FSM. In addition, ST language is friendlier to programmers who are familiar with textual programming languages. Based on these points, the ST language has been chosen to program the HVOF spray control system. A simplified example of code is displayed in Figure 5.4. State (black frame) will change (orange frame) from one to another when the condition and/or input (blue frame) is satisfied. Corresponding actions (red frame) will be carried out when the system moves into a specific state.

```

CASE DJ_Select_Sys_State OF
(*initial state*)
  MANUALTEST
    (*Manually OPEN EV *) (*OPEN gas *)
    mySysOutput.O2IN := TRUE;
    ...
    IF DJ_ManualMode=FALSE THEN
      DJ_Select_Sys_State:=STOP_READY;
    ...
    END_IF
  STOP_READY:
    ...
    IF EDGEPOS(DJ_Bt_Run) = TRUE THEN
      //Aspiration ON Refroidissement ON
      ...
      DJ_Select_Sys_State := VERIFICATION;
    END_IF
  VERIFICATION
    (*verify if the user defined gas parameters and the water parameters are suitable*)
    IF ((DJ_Water.Water Flow>= 8) AND (DJ_Water.Water Temp Outlet <= 45)) THEN
      IF (DJ_User_Gas.O2>=74) AND (DJ_User_Gas.CH4 >=50) AND (DJ_User_Gas.GP>=12) THEN
        DJ_Select_Sys_State := START_GAS;
      ELSE
        DJ_Select_Sys_State := STOP_READY;
      END_IF
    ELSE
      DJ_Select_Sys_State := STOP_READY;
    END_IF
    ...
    IF DJ_Gas_Flow.O2>= myDJRecipe[0].START_O2_ARC THEN
      DJ_Arc := 1;
      DJ_Select_Sys_State := START_IGNITION
    END_IF
  START_IGNITION:
    ...
END_CASE

```

Figure 5.4 A simplified example of code for the control system

With the basic principle, hardware, and programming language, the HVOF spray control system has been developed. Details about the different interfaces of the control system will be rapidly introduced in the following.

5.1.4. The interfaces of the HVOF spray control system

Figure 5.5 displays the operation panel of the HVOF spray control system. The electronic control screen offers interfaces for the main operations. However, the “CDS” (see Figure 5.6 for details) and “Diamond-Jet” pages (see Figure 5.7 for details) are used to control the CDS torch and the Diamond-Jet 2701/2702 torch, separately. What is more, the system also provides a “Maintenance” page (see Figure 5.8 in details), on which users can conveniently test the electromagnetic valves and manually adjust the system. A “Configuration” page (see Figure 5.9 for details) was also designed for setting and recording the gases’ flow rates during the HVOF process. What is more, the history of the gases’ flow rate during the spraying process can be recorded using the background program. A variety of safety logic has been considered in this control system. Some mechanical buttons have been provided for key controls and a self-locking button for critical situations. For example, the “Start,” “Stop,” “Rapid stop,” and “Emergency stop” functions are controlled by mechanical buttons. The switches for the “CDS” and “Diamond-Jet” systems are controlled by both mechanical and virtual buttons.

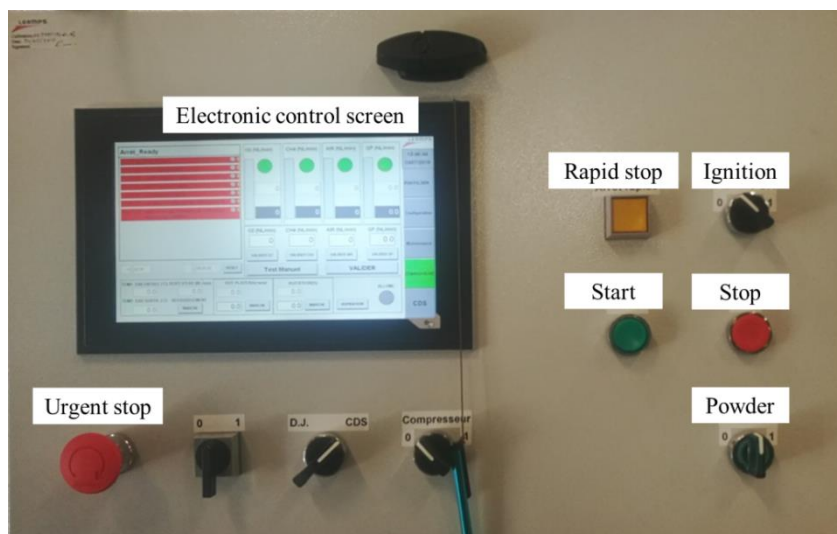


Figure 5.5 Operation panel of the HVOF spray control system

Interfaces of the CDS system and Diamond-Jet system

Figure 5.6 and Figure 5.7 exhibit the user interfaces of the CDS system and the Diamond-Jet system, respectively. Although the torch and gases used are different, the workflows and interfaces are similar. Part A is used to pre-define the gases’ flow-rate values and to show the status of the real gases’ flow rates during operation. However, A1 and A3 display the percentage and numerical value of the

real gas flow rate, respectively; A2 shows the difference between the pre-defined and real gas flow rate in color; A4 gives the pre-defined gas flow rate. Part B offers manual operating buttons for verification and testing under special security requirements. Part C displays the immediate warnings and alarms. Part D calculates the total and single spraying time. Part E shows the status of cooling water, including water flow rate and water temperature input and output. Part F presents the status of the powder feeder, containing the pre-defined and real rotation speed of the tray and stirrer, which will directly determine the powder feed rate. Part G is used to control the air compressor (G1) and shows the spraying status of the system (G2). Part H is designed to switch the interfaces.

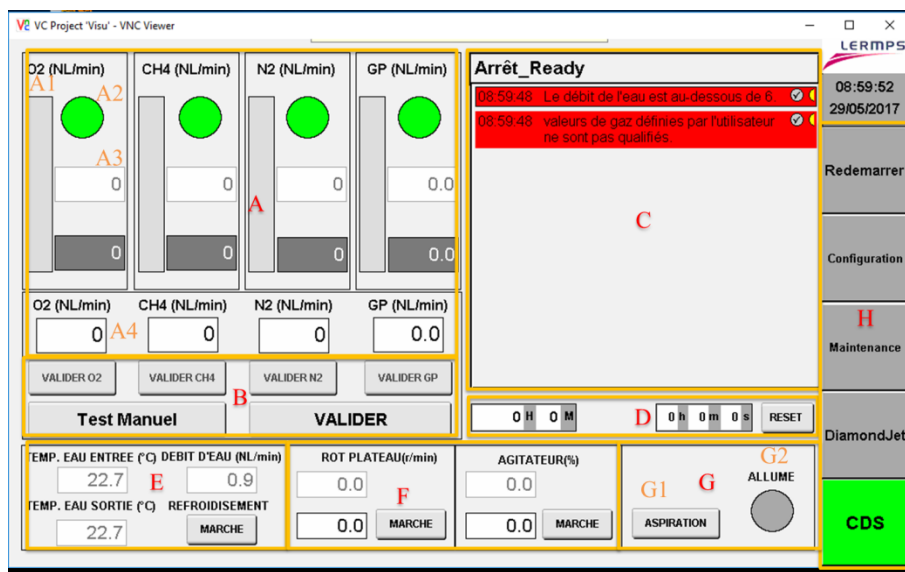


Figure 5.6 Interface of the CDS system

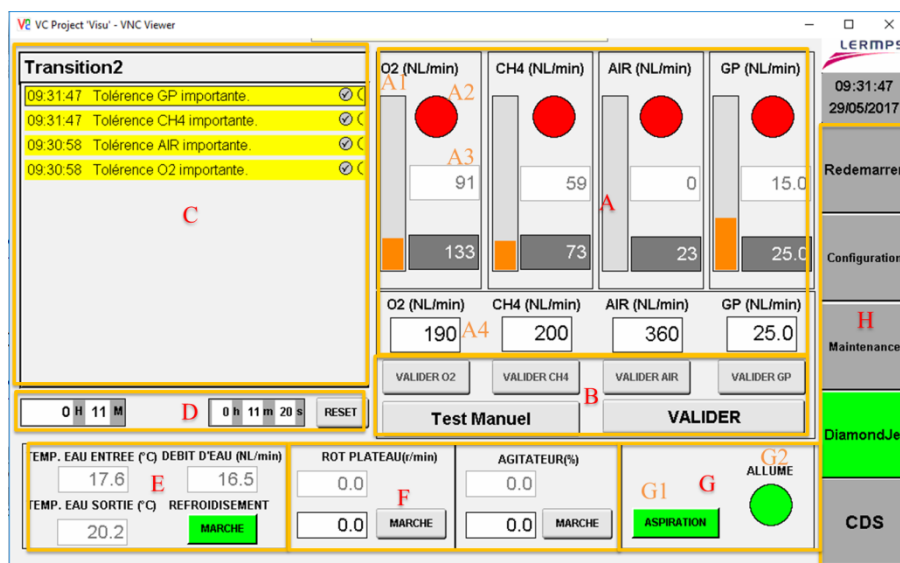


Figure 5.7 Interface of the Diamond-Jet system

Interface for maintenance

Figure 5.8 shows the interface for maintenance. The statuses of all the electromagnetic valves are displayed on this page, as well as the gas flow rates. Part A shows the real and set gas flow rates of all the gases used in this control system. Buttons are also offered for testing the gases. Part B lists all the electromagnetic valves used in this system, which conveniently help to detect and maintain the system. Part C displays the statuses of gases and accessories used, which are connected to the sensors. Thus, the maintenance of the HVOF control system, and the detection of the statuses of the electromagnetic valves, can be conveniently carried out using this “Maintenance” page.

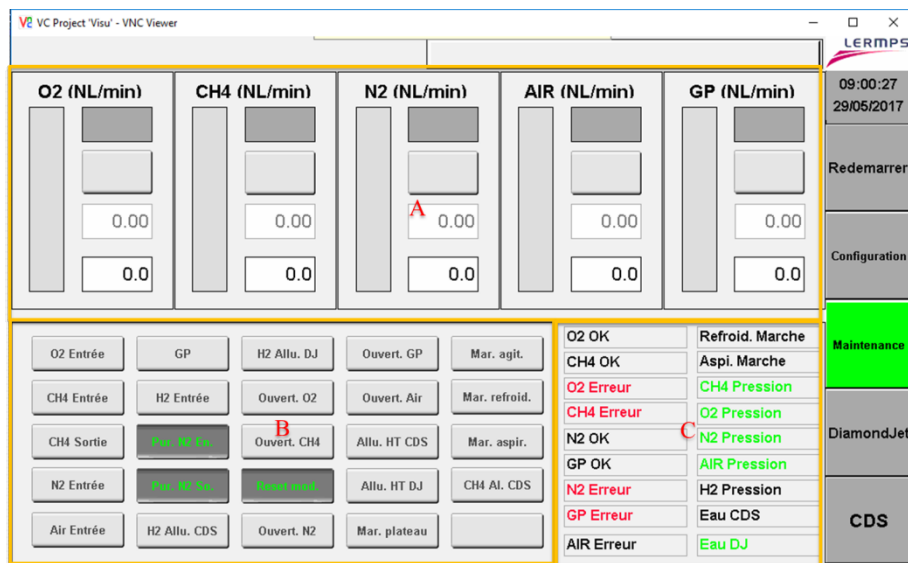


Figure 5.8 Interface of the maintenance system

Interface for configuration

Figure 5.9 shows the interface for configuration. This page is employed to switch languages (A) for the whole system and pre-define system parameters for stable ignition for the CDS (B) and Diamond-Jet systems (C). Generally, the gases’ flow rate values are fixed for stable ignition and flameout. However, the spray system may change gradually over time and use. It is necessary to set this page for further adjustment.

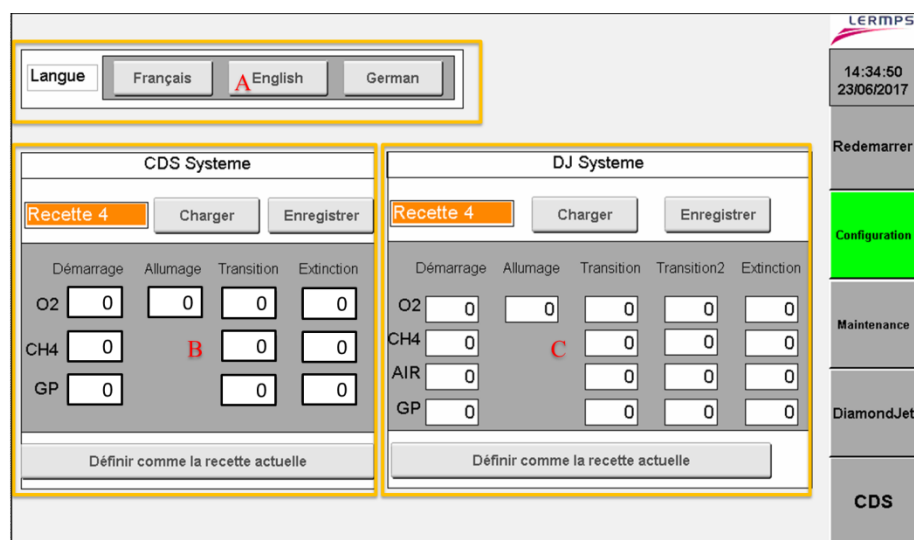


Figure 5.9 Interface of the configuration system

5.1.5. Data recording system

This control system also provides a background program for recording the process data during spraying. The data for the CDS and Diamond-Jet systems are recorded in the separated folders. Every single record is created in a single file from successful ignition to flameout. As shown in [Figure 5.10](#), the spraying period, system state, set and real gases flow rates, and spraying environment (cooling waters' flow rate and temperature) are recorded. The data is recorded every 100 ms. This recording system conveniently monitors the spray process and observes potential fluctuations during the spraying process. These data can be also used as big data to perform future data mining and system analysis.

CDS system

A	B	C	D	E	F	G	H	I	J	K	L	M
Num	IgnitionState	SetO2	SetCH4	SetN2	SetGP	RealO2	RealCH4	RealN2	RealGP	WaterTempIN	WaterTempOUT	WaterFLOW
Wed Sep 13 18:16:06 2017												
1	0	30	10	0	10	0	4.17493	0	0.503555	20.0232	20.3345	8.81863
2	0	30	10	0	10	0	4.13099	0	0	20.0262	20.3345	9.44853
3	0	30	10	0	10	0	0	0	0	20.0232	20.3375	9.44853
4	0	30	10	0	10	0	0	0	0	20.0232	20.3375	9.27641
...												
1444	0	30	10	0	10	88.992	30.5869	0	14.9785	20.307	22.1656	9.51323
1445	0	30	10	0	10	88.7173	30.5429	0	14.9632	20.307	22.1534	9.36552
1446	0	30	10	0	10	88.168	30.6308	0	14.9907	20.307	22.1412	9.2349
1447	0	30	10	0	10	87.5881	30.455	0	14.9663	20.307	22.1351	9.17997
1448	0	0	0	0	0	7.0998	30.3232	0	14.9602	20.3101	22.1229	9.46928
Wed Sep 13 18:20:56 2017												

Diamond-Jet system

A	B	C	D	E	F	G	H	I	J	K	L	M
Num	IgnitionState	SetO2	SetCH4	SetAir	SetGP	RealO2	RealCH4	RealAir	RealGP	WaterTempIN	WaterTempOUT	WaterFLOW
Tue Oct 10 12:08:46 2017												
1	0	40	20	10	12	0	4.90005	0	0.524918	17.6458	17.8259	16.4788
2	0	40	20	10	12	0	4.8561	0	0.512711	17.6458	17.8289	16.5862
3	0	40	20	10	12	0	4.79018	0	0	17.6458	17.8289	16.7254
4	0	40	20	10	12	0	4.87808	0	0	17.6458	17.8259	16.5423
...												
1790	3	163.333	146.667	120	15	176.946	254.847	117.618	14.9602	19.7485	28.5409	16.0344
1791	3	163.333	146.667	120	15	176.428	255.088	117.191	14.9449	19.7546	28.5409	15.9246
1792	3	163.333	146.667	120	15	176.122	255.308	117.008	14.9266	19.7516	28.5348	16.2114
1793	3	163.333	146.667	120	15	176.092	255.462	117.069	14.9754	19.7546	28.5348	16.1052
1794	0	0	0	0	0	176.061	255.462	115.238	14.9663	19.7546	28.5318	16.2835
Tue Oct 10 12:14:45 2017												

Figure 5.10 Data recording files for the CDS and Diamond-Jet systems

5.2. Integration of the ANN models into the HVOF spray control system

In Chapter 4, two ANN models have been constructed, optimized, and trained to study the HVOF spray process by relating the coating properties with the behaviors of in-flight particles with the ANN1 model and predicting particle behaviors based on the process parameters of the ANN2 model. This process was completed based on MATLAB software, in which two packaged ANN networks were obtained. In this section, two algorithms were introduced, which were permitted to convert these two packaged networks into the cyclic PLC program using the IEC 61131-3 language in Automation Studio™. The workflow is illustrated in Figure 5.11.

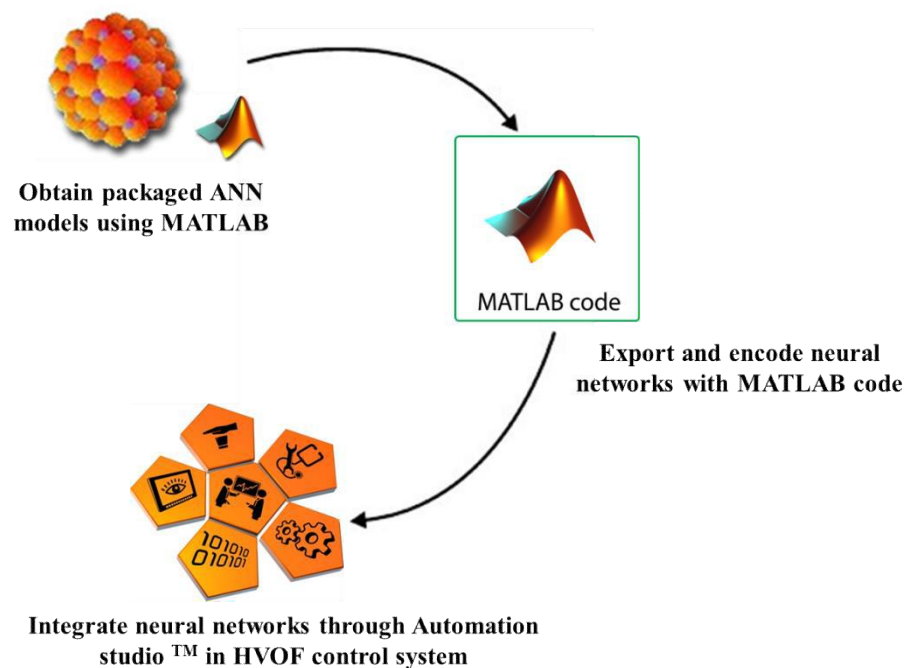


Figure 5.11 The workflow of integrating the ANN model

5.2.1. Extracting and programming with MATLAB code for ANN models

Extracting information from packaged ANN models

As introduced above, the first step is to extract information from packaged ANN models. With the command “genFunction,” a MATLAB function is generated for the simulation of a shallow neural network. Neural network constants, simulation process, and module functions are, therefore, acquired. Taking the ANN1 model as an example, some of the neural network constants are listed in [Figure 5.12](#). Variable x1_step1 contains the constants necessary to pre-process input data in the input layer. Variables b1 and IW1_1 consist of the bias or weights linking the input layer and the first hidden layer. Similarly, b2 and LW2_1 contain the bias or weights between hidden layers and b3, and LW3_2 provide bias or weights connecting the output layer from the second hidden layer. Variable y1_step1 gives the constants for post-processing the output data in the output layer. Therefore, the ANN models can be ported to other platforms using these neural network constants, according to MATLAB codes.

```

21 % Input 1
22 - x1_step1.xoffset = [-0.6;-0.333333333333333;-0.733333333333333];
23 - x1_step1.gain = [2.08333333333333;3.75;1.875];
24 - x1_step1.ymin = -1;
25
26 % Layer 1
27 - b1 = [0.59920030150300385152;-0.62843589200943650308;-1.229581324450538915;
28 - IW1_1 = [-0.95772371718778104288 0.1665085782326159447 -0.07509559721509447
29
30 % Layer 2
31 - b2 = [3.9962238132470506713;1.1697364838164683309;0.56083327205033761675;0.
32 - LW2_1 = [-0.56950053758409691085 2.8227463299331700952 1.119165469283033509
33
34 % Layer 3
35 - b3 = [-1.7645817671997705567;-0.62975280520270671136];
36 - LW3_2 = [-0.043558844221938723684 -0.30031689513774800782 0.461826490285277
37
38 % Output 1
39 - y1_step1.ymin = -1;
40 - y1_step1.gain = [1.44404332129964;3.78787878787879];
41 - y1_step1.xoffset = [-0.73;-0.248];

```

Figure 5.12 Neural network constant of the ANN1 model

Programming with MATLAB code for the ANN models

According to the structure of the ANN model, the ANN1 model can be programmed with MATLAB code using specific parameters and functions used in the ANN1 model, as displayed in [Figure 5.13](#). Matrix Xp1 stores pre-processed input data, which will be further transformed into the input layer. Matrix a1, a2, and a3 correspond to the value stored in neurons in the input layer, the first hidden layer, and the second hidden layer, respectively. The a3 matrix will be post-processed and stored in Y1 for exporting final predicted values. Wherein, the functions “tansig,” “logsig,” and “purelin” are the transfer functions used in the ANN1 model from the input layer to the first hidden layer, from the first hidden layer to the second hidden layer, and from the second hidden layer to the output layer, respectively. It should be noted that different ANN models may have various transfer functions. Therefore, the code needs to be adjusted accordingly. After understanding the structure and the procedure of the ANN model, work can continue to program the ANN model within Automation Studio™, using the IEC 61131-3 language and by integrating it into the HVOF spray control system.

```

1      % Input 1
2 -    Xp1 = times(X-x1_xoffset,x1_gain)+x1_ymin;
3
4      % Layer 1
5 -    a1 = tansig(b1 + IW1_1*Xp1);
6
7      % Layer 2
8 -    a2 = logsig(b2 + LW2_1*a1);
9
10     % Layer 3
11 -    a3 = purelin(b3 + LW3_2*a2);
12
13     % Output 1
14 -    Y1 = rdivide(a3-y1_ymin,y1_gain)+y1_xoffset;

```

Figure 5.13 Code for constructing the ANN1 model in MATLAB

5.2.2. The combination of ANN models with the HVOF control system

Structured text has also been chosen to program the ANN models. Attention should be paid to the calculation between the matrices. It is highly recommended to include the library “MTLinAlg” to call functions for matrix operations in the Automation Studio™. The ANN models have been integrated and the interface in the HVOF spray control system is shown in [Figure 5.14](#). After entering the process parameters, the velocity and temperature of in-flight particles will be predicted and will further flow into the ANN2 model to serve as input. The coating properties will then be calculated and shown on the interface. [Figure 5.14](#) also demonstrates a calculation example, in which the stand-off distance was set at 200 mm, the O₂ flow rate at 200 slpm, and the CH₄ flow rate at 180 slpm. The velocity and temperature of in-flight particles are predicted as 461 m/s and 2096 K by the ANN1 model. The coating properties are calculated by the ANN2 model, giving the microhardness as 712 HV_{0.3}, porosity as 0.196%, and wear rate as $2.184 * 10^{-5}$ mm³/N/m. These values are exactly the values predicted by the ANN models and are consistent with experimental values. Therefore, the ANN models have been successfully integrated into HVOF spray control.

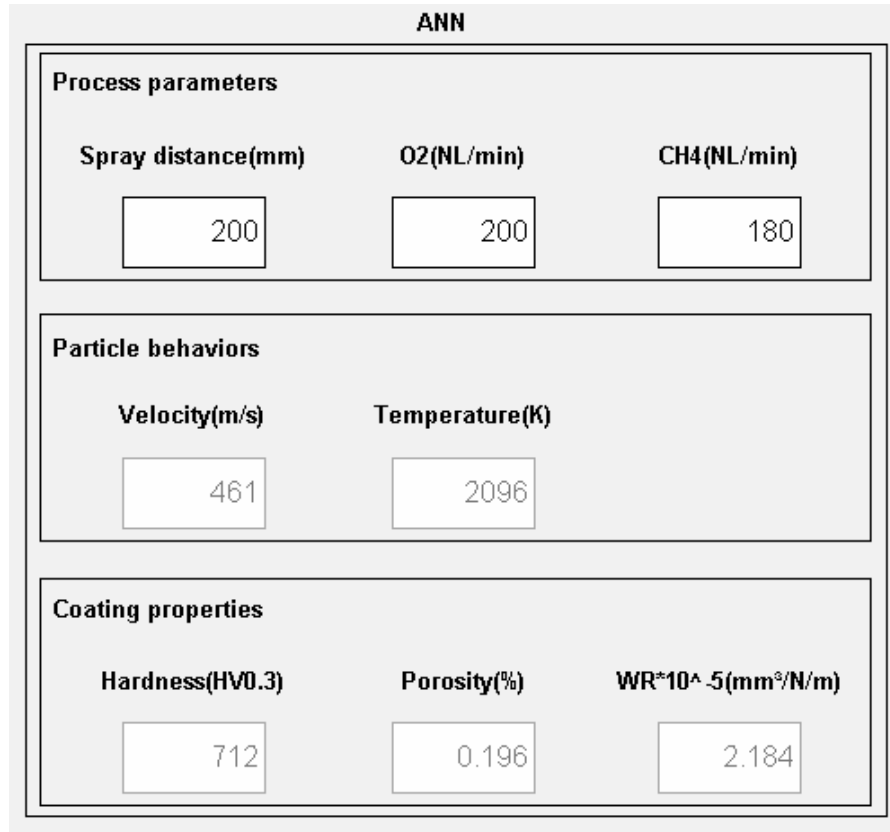


Figure 5.14 Interface of the ANN models in an HVOF control system

5.3. Development and integration of the reversed ANN model

A reversed ANN model (ANN3 model) has been developed to predict the process parameters based on the properties of the coating. By combining the ANN3 model with the integrated system introduced in [Section 5.2](#), feedback control was expected.

In the ANN3 model, microhardness has been chosen as the input. Compared to the coating's wear rate, microhardness is easily available. However, it is more reliable compared to the coating's porosity, which tends to be of a relative value. Process parameters (i.e., stand-off distance, O₂ flow rate, and CH₄ flow rate) have been set as outputs. The ANN3 model also went through the same optimization procedures as the ANN1 and ANN2 models, to obtain the most suitable functions and parameters. An R value of 0.97596 has been obtained based on the optimized ANN3 model, which is smaller than that of the ANN1 model (0.99991) and ANN2 model (0.99997). This demonstrates that the ANN3 model performs worse with its prediction requirements, which is mainly due to the lower amount of data in the input layer. Additionally, the duplicated data in the output layer also deprives the

prediction performance of the ANN3 model.

In order to integrate the ANN3 model, two options have been supplied with a button “Link” in Figure 5.15. For the first option (without pressing the button), the ANN3 model will operate independently and gives the results individually, providing a reference for the comparison of the process parameters. Due to the relatively low accuracy of the ANN3 model, the ANN3 model is used as a reference in this work. As shown in Figure 5.15, the process parameters predicted by the ANN3 model is not exactly equal to the set value. The stand-off distance is smaller than the expected value, while the O₂ and CH₄ flow rates are higher. Therefore, the set value can be adjusted to make them consistent. For the second option (pressing the button), the outputs of the ANN3 model will be transferred to the ANN1 model and works as the inputs of the ANN1 model to realize the feedback control. There is no doubt that the accuracy of the ANN3 model will increase with the growth of the data set. Therefore, although the second option has not been used here, it is useful to prepare the second option for further research.

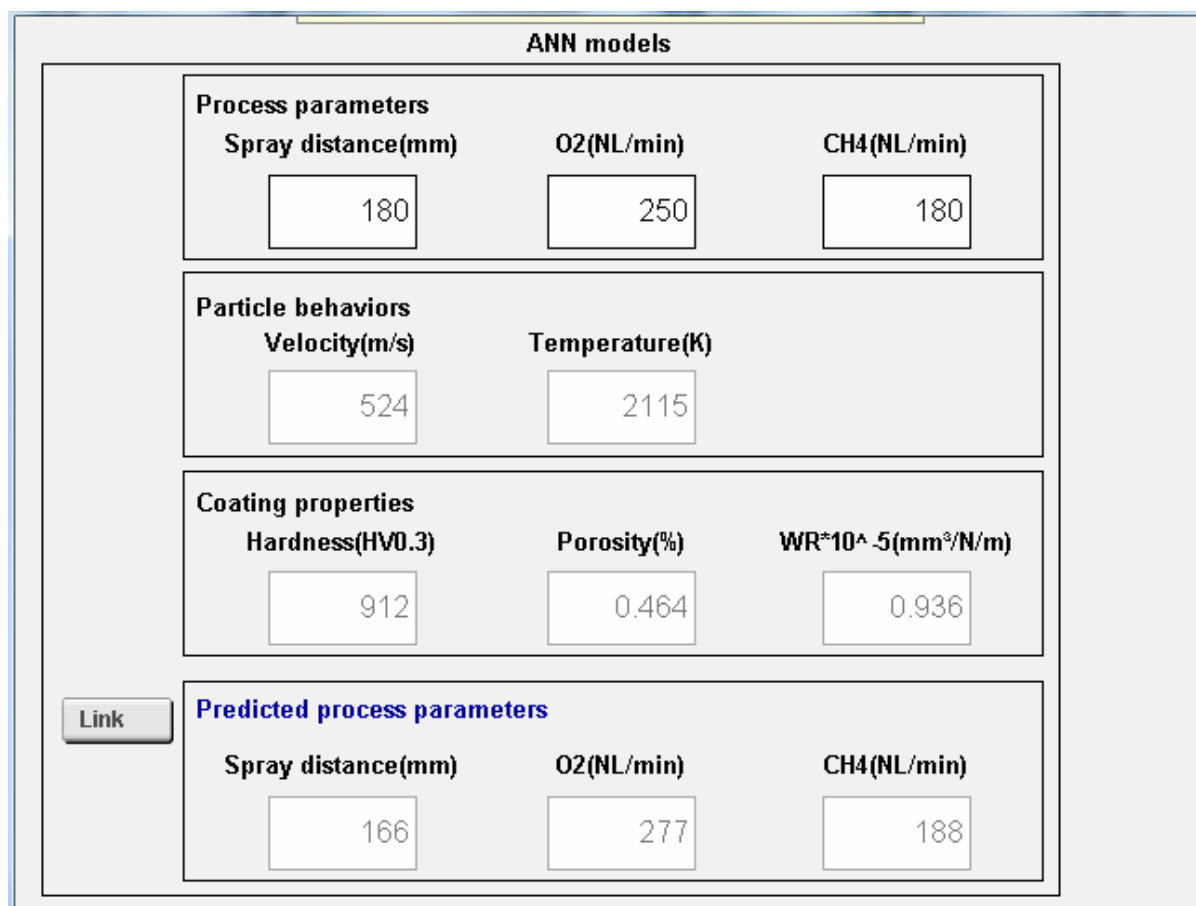


Figure 5.15 Integration of the ANN3 model into the HVOF control system

5.4. Conclusions

In this chapter, the HVOF spray control system has been developed and introduced in detail. Next, two packaged ANN models have been extracted and reprogrammed with the PLC programming language defined in IEC 61131-3; this is to realize the intelligent HVOF spray control system and real-time prediction the HVOF process and the HVOF sprayed NiCr-Cr₃C₂ coating.

In the first step, the hardware and software architectures have been decided according to the system requirement. The principle of the control system has been explained, offering the foundation for the developing control system. The operation has been clearly explained, ensuring the corrected operation of the system. In addition, a data recording system has been programmed and runs in the background during the spray process; this makes it convenient to monitor the spray process and observe potential fluctuations. Finally, the whole control system has been programmed using Structure Text (ST) language and transferred to the PLC platform.

For the integration of the ANN models, the information stored in the two packaged ANN models has been firstly extracted in MATLAB. This information, together with the specific functions used, helps to encode the ANN models using MATLAB code. Finally, the ANN models have been programmed with IEC 61131-3 language in Automation StudioTM and integrated in the HVOF spray control system.

A reversed ANN model (i.e., ANN3 model) has been developed to predict the process parameters based on coatings' microhardness. It has been integrated into the HVOF control system, in which two usage modes have been supplied. In this work, the outputs predicted by the ANN3 model have been used as a reference due to its relative low prediction accuracy. Another option has been supplied for further development of a feedback control system in the future.

This integration of ANN models into the HVOF control system provides a preliminary idea about constructing an intelligent control system for the HVOF spray process and can be promoted to other thermal spray technologies. More data and information are expected to build up ANN-assisted thermal spray control systems for different types of feedstock and thermal spray technologies.

Reference of chapter 5

- [1] Wikipedia, Programmable logic controller, in, https://en.wikipedia.org/wiki/Programmable_logic_controller.
- [2] M. Carvo, Five Types of PLC Language, in, <https://www.techwalla.com/articles/five-types-of-plc-language>, 2018.
- [3] Wikipedia, 61131-3, in, https://en.wikipedia.org/wiki/IEC_61131-3IEC
- [4] Wikipedia, Ladder logic, in, https://en.wikipedia.org/wiki/Ladder_logic.
- [5] Wikipedia, Sequential function chart, in, https://en.wikipedia.org/wiki/Sequential_function_chart.
- [6] Wikipedia, Structured text, in, https://en.wikipedia.org/wiki/Structured_text.
- [7] Status IEC 61131-3 standard, in, PLCopen, 1993.
- [8] Wikipedia, Finite-state machine, in, https://en.wikipedia.org/wiki/Finite-state_machine#cite_note-1.

Chapter 6. Conclusions and perspectives

6.1. Conclusions

After decades of development, thermal spray technologies have been widely applied in various industries to deal with a range of challenges. Along with this, diverse optimization and modeling methods have also been developed and employed to study the mechanism and coating formation, to deposit the desired coatings that meet specific requirements. In this context, the ANN model can be a satisfied candidate and more attention should be paid to it.

This dissertation aims to develop an intelligent HVOF spray control system via machine learning, specifically ANN models, to provide a comprehensive understanding of the relationship among HVOF process parameters, behaviors of in-flight particles, and coating performances. For the above purpose, 40 sets of thermal spray experiments have been carried out, as well as corresponding characterizations and tests. Hereafter, preliminary analyses of the behaviors of in-flight particles, as well as the phase components, microstructure, and properties of coating, have been given from the view of HVOF spray technology. The relationships among them are ambiguous and it is impossible to directly summarize. Therefore, ANN models were proposed, created, and trained to predict the properties of HVOF sprayed NiCr-Cr₃C₂ coating and analyze the influence of operating parameters considering the intermediate process. In addition, MIV-based analysis has been carried out to evaluate the factors' importance in ANN models. Finally, a HVOF spray control system was programmed to control and record the spraying process. Based on this control system, two packaged ANN models have been reprogrammed and integrated into the HVOF spray control system. The detailed conclusions from this research are summarized below.

Preliminary understanding of the HVOF process and HVOF sprayed coatings

From 40 sets of experiments and corresponding tests that have been carried out based on different process parameters, it can be roughly summarized that:

1. The temperature of in-flight particles shows a growing tendency with the increase of the O₂ flow rate. On the other hand, it shows an initially increasing, then decreasing, trend with an increasing stand-off distance. The temperature generally decreases with an increasing CH₄ flow rate, except for some fluctuations with longer stand-off distances. The increase of the O₂ flow rate would increase the velocity of in-flight particles. However, with the increase in the

stand-off distance, the effect of O₂ flow rates on the velocity of in-flight particles fades out. The velocity decreases progressively with the increasing stand-off distance. The CH₄ flow rate has a negligible impact on the velocity of in-flight particles.

2. The analysis of phase components indicates that the coatings are mainly composed of Cr_{1.12}Ni_{2.88}, Cr₇C₃, and Cr₂₃C₆. The microstructure of NiCr-Cr₃C₂ coatings proves that the spraying process is robust as uniform coatings, made of a distribution of hard carbide phase in the NiCr binder phase matrix, are obtained for all conditions. Subsequently, the porosity, microhardness, and wear rate of coatings has been discussed, considering the influence of behaviors of in-flight particles. It can be visually summarized that both the velocity and temperature of in-flight particles have an impact on the properties of coatings. However, it is impossible to directly relate the performances of in-flight particles to coating properties.

Therefore, machine learning methods, especially ANN models, were proposed to predict and study the HVOF spray process and the influence of the behaviors of in-flight particles on coating properties.

Constructing and analyzing ANN models

Two ANN models have been constructed and optimized to predict the properties of HVOF sprayed NiCr-Cr₃C₂ coating and to analyze the influence of operating parameters considering the intermediate process. It can be concluded that:

1. The ANN1 model has performed to forecast the relationship between the HVOF spray process parameters (i.e., stand-off distance, CH₄ flow rate, and O₂ flow rate) and the behaviors of in-flight particles (temperature and velocity) with a maximum relative error of 0.76% for velocity and 0.43% for temperature. The reliability and accuracy of the ANN1 model has been verified by the test sets with a relative error of 0.43% for velocity and 0.14% for temperature.
2. The ANN2 model has been trained to predict coating properties (i.e., microhardness, porosity, and wear rate) according to the characterizations of in-flight particles. A maximum relative error of 1.34%, 1.00%, and 3.15% for microhardness, porosity, and coating wear rate of coatings, respectively, have been obtained. Test sets have been used to certify the reliability and accuracy of the ANN2 models, for which the relative errors (0.06% for microhardness,

0.15% for porosity, and 0.31% for wear rate) are smaller than the maximum errors.

3. The MIV-based analysis has been executed to evaluate the importance of these factors. Analysis shows that the important sequence of the factors for the velocity of in-flight particles are stand-off distance > O₂ flow rate > CH₄ flow rate; for the temperature: stand-off distance > CH₄ flow rate > O₂ flow rate; for coating's microhardness: V > T; for coating's porosity and wear rate: T > V.

These two well-trained ANN models can be applied to the prediction of coating properties and in-flight particles behaviors, as well as the optimization of coatings. What is more, the MIV-based analysis makes up the study of the importance of the process parameters, which is lacking but is necessary for the ANN model. The development of ANN models in thermal spray technologies helps to better study thermal spray processes and controlled coating performances.

Developing an HVOF spray control system and the integration of ANN models

A HVOF spray control system has been developed for the HVOF thermal spray process from a global perspective. Most importantly, both the CDS torch and Diamond-Jet 2700 torch of the control systems were developed, taking different spraying requirements into account. Data recording has also been considered, as well as the maintenance and configuration requirement. In addition, it also provided an interface with which to subsequently integrate the ANN model into the HVOF control system.

As introduced in [Chapter 4](#), two packaged ANN models have been obtained. Hereafter, their information has been extracted and their structures have been reconstructed using MATLAB code. Based on this, the ANN models have been further reprogrammed using IEC 61131-3 language in Automation Studio™. An intelligent HVOF spray control system has been realized and the real-time prediction of the HVOF process and HVOF sprayed NiCr-Cr₃C₂ coating has been achieved.

6.2. Perspectives

With the development of society, there is no doubt that machine learning, especially artificial intelligence, will catch more and more attention in various fields, indicating its universality and high

accuracy. The combination of artificial intelligence and thermal spray technologies will further promote the research of the thermal spray process, as well as the development of high-quality thermal sprayed coatings. In the author's opinion, further work should focus on the following aspects.

Data size is one of the most important factors influencing the applicability and accuracy of artificial intelligence models. Nowadays, with the development of thermal spray control systems and monitoring equipment, it is convenient to collect data from thermal spray processes. However, it is still time-consuming work to obtain enough coating information from various tests. Based on this point, it is recommended to first study the thermal spray processes themselves with more alternative artificial intelligence methods. However, eventually, with the expansion of the coating information, attention should be paid to developing a comprehensive artificial model considering both the thermal spray processes and coating properties.

A gene database is highly recommended to construct for thermal spray technologies, considering all kinds of factors, such as types of thermal spray technology and torches, process parameters of the spray system, robot operating parameters, feedstock powders properties, hardware characteristics, and spraying environments. What is more, as time goes on, the performance of torch and spray systems may gradually change. Therefore, the duration should also be recorded and considered as a factor. With this all-in-one gene database, artificial intelligence methods will be more capable of studying thermal spray technologies

Abstract

In the high velocity oxygen fuel (HVOF) spray process, the coating properties are sensitive to the characteristics of in-flight particles, which are mainly determined by the process parameters. Due to the complex chemical and thermodynamic reactions during the deposition procedure, obtaining a comprehensive multi-physical model or analytical analysis of the HVOF process is still a challenging issue. This study proposes to develop a robust methodology via artificial neural networks (ANN) to solve this problem for the HVOF sprayed NiCr-Cr₃C₂ coatings under different operating parameters.

First, 40 sets of HVOF spray experiments and coating property tests were carried out for analysis and to build up the data set for ANN models. The relationship among the process parameters, behaviors of in-flight particles, and coating properties were investigated from an intuitive view, which provided a preliminary understanding of the HVOF process and sprayed coatings. Even though the effect of process parameters on the behaviors of in-flight particles and thus on the coating's properties can be roughly summarized, it is impossible to build up direct connections among them.

Second, two ANN models were developed and implemented to predict coating's performances (microhardness, porosity and wear rate) and to analyze the influence of operating parameters (stand-off distance, oxygen flow rate, and fuel flow rate) while considering the intermediate variables (temperature and velocity of in-flight particles). A detailed procedure for creating these two ANN models is presented in this work, which encodes the implicitly physical phenomena governing the HVOF process. A set of additional experiments were also conducted to validate the reliability and accuracy of the ANN models. The results show that the developed implicit models can satisfy the prediction requirements. Clarifying the interrelationships between the spraying conditions, behaviors of in-flight particles, and the final coating performances will provide better control of the HVOF sprayed coatings. Additionally, mean impact value (MIV) analysis was conducted to quantitatively explore the relative significance of each input on outputs for improving the effectiveness of the predictions.

Lastly, the well-trained ANN models were programmed and integrated into the homemade HVOF spray control system to realize an intelligent control system. With this system, the temperature

and velocity of in-flight particles can be calculated by entering process parameters, and thereafter obtaining specific coating properties. A reverse ANN model was also integrated, which calculates process parameters based on the microhardness of the coating to guide the selection of the best parameters. This integration provides a preliminary idea for the construction of an intelligent control system for HVOF spray process and can be promoted to other thermal spray technologies.

Overall, based on a large data set, this work not only intuitively analyzed the relationship among process parameters, behaviors of in-flight particles, and coating's properties, but also provided a prediction method for the HVOF spray process and HVOF sprayed coatings via the optimized and well-trained ANN models. In addition, a prototype to realize an intelligent control system for HVOF spray process has also been suggested.

Résumé

Dans le procédé de projection thermique de flamme d'oxygène à haute vitesse (HVOF), les propriétés du revêtement sont sensibles aux caractéristiques des particules en vol, qui sont principalement déterminées par les paramètres du procédé. En raison des réactions chimiques et thermodynamiques complexes au cours de la formation du dépôt, l'obtention d'un modèle multi-physique complet ou d'une analyse analytique du processus HVOF reste un challenge difficile. Cette étude propose de développer une méthodologie robuste via les réseaux de neurones artificiels (ANN) pour résoudre ce problème pour les revêtements NiCr-Cr₃C₂ élaborés par HVOF sous différents paramètres opératoires.

Premièrement, 40 ensembles d'expériences de projection HVOF et tests de propriétés du revêtement ont été effectués pour l'analyse et la constitution des données pour les modèles ANN. La relation entre les paramètres opératoires, le comportement des particules en vol et les propriétés du revêtement a été étudiée à partir d'une vue intuitive, qui fournit une compréhension préliminaire du processus HVOF et des revêtements. Même si l'effet des paramètres du processus sur ces derniers peut être résumé sommairement, il est impossible d'établir une relation directe entre eux.

Deux modèles ANN ont été développés et mis en œuvre pour prédire les performances du revêtement (micro-dureté, porosité et taux d'usure) et pour analyser l'influence des paramètres opératoires (distance de projection, débit d'oxygène et débit de carburant) en considérant les variables intermédiaires (température et vitesse de particules en vol). Une procédure détaillée de création de ces deux modèles ANN est présentée dans cette étude, qui encode implicitement les phénomènes physiques régissant le processus HVOF. Une série d'expériences supplémentaires ont également été menées pour valider la fiabilité et la précision des modèles ANN. Les résultats montrent que les modèles implicites développés peuvent satisfaire aux exigences de prédiction. La clarification des relations entre les conditions de projection, les comportements des particules en vol et les performances finales du revêtement offrira un meilleur contrôle des revêtements déposés par HVOF. De plus, l'analyse de la valeur d'impact moyenne (MIV) a été menée pour explorer quantitativement l'importance relative de chaque entrée sur les sorties pour améliorer la prédiction efficace.

Enfin, les modèles ANN bien formés ont été programmées et intégrés dans le système de contrôle de projection HVOF fait maison pour réaliser un système de contrôle intelligent. À l'aide de ce système, la température et la vitesse des particules en vol peuvent être calculées en saisissant les paramètres opératoires, puis des propriétés de revêtement spécifiques peuvent être obtenues. Un modèle ANN inversé a également été intégré, qui calcule les paramètres opératoires disponibles en fonction de la micro-dureté du revêtement pour guider la sélection des meilleurs paramètres. Cette intégration fournit une idée préliminaire de la construction d'un système de contrôle intelligent pour le processus de projection HVOF et peut être promue à d'autres technologies de projection thermique.

Dans l'ensemble, basé sur un grand nombre de données, ce travail a non seulement analysé intuitivement la relation entre les paramètres du processus, les comportements des particules en vol et les propriétés du revêtement, mais a également fourni une méthode de prédiction pour le processus de projection HVOF et les revêtements déposés par HVOF via le modèle ANN optimisé et bien formé. En outre, un prototype pour réaliser un système de contrôle intelligent pour le processus de projection HVOF a également été suggéré.



SPIM

■ École doctorale SPIM - Université de Technologie Belfort-Montbéliard
F - 90010 Belfort Cedex ■ tél. +33 (0)3 84 58 31 39
■ ed-spim@univ-fcomte.fr ■ www.ed-spim.univ-fcomte.fr

